Systems-biology Approaches for Studying Phosphatase Activity in Coxsackieviral Heart Disease

A Dissertation

Presented to the faculty of the School of Engineering and Applied Science in partial fulfillment of the requirements for the degree of

Doctor of Philosophy

By Millie Sunil Shah
January 2018

Department of Biomedical Engineering
University of Virginia

Table of Contents

Acknowledgements

This dissertation could not have been possible without the support of many people, this work is dedicated to them.

I would first like to thank the many mentors and advisors who encouraged me to pursue a research career in biomedical engineering. Thank you to Dr. Feilim MacGabhann for encouraging the curiosity of a young scientist and patiently teaching me how to conceive, design, and execute a research project (and also how to code in MatLab). Your mentorship prepared me for graduate school at UVa and continues to be invaluable as my career progresses. Thank you to Dr. Rosandra Kaplan who took a chance on a computational scientist and gave me the freedom to develop my wet-lab skills. My time in your lab at the NIH was pivotal in my growth as a scientist and as a person (and so much fun too!). Thank you to Dr. Andreas Raue who guided me through industry research and showed me that doing good science with integrity can happen outside the halls of academia and can have real impact. Thank you to my committee chair Dr. Jeffery Saucerman, your support and advice throughout these years has been invaluable. Lastly, I would like to thank my dissertation advisor Dr. Kevin Janes. Thank you for teaching me the ins and outs of experimental work and always being available to help troubleshoot difficult experiments or discuss confusing results (which happened a lot). You have always challenged me to aim high and given me the skills to achieve those aims. Also, you have boundless patience and for that I thank you.

I would also like to thank my colleagues (and friends) in the Biomedical Engineering department. UVa has a uniquely supportive graduate community that makes graduate school, dare I say it, *fun*. My time here has been enriched by so many people both scientifically and personally. I would specifically like to acknowledge my fellow lab mates who were supportive, critical, and down for a beer at all the right times. To Cheryl Borgman, our lab cannot function without you, thank you so much for your patience and help. To Sameer Bajikar, your advice throughout the years helped me make the most of grad school and your friendship outside of lab helped me make the most of Charlottesville. To Zeinab Chitforoushzadeh, thank you for always being a positive presence in lab. To Elizabeth (Liz/Beth) Pereira thank you for listening to all my complaints, not judging me for watching puppy videos between experiments, and keeping me fit; your work ethic will surely set you up for success as you finish your PhD. To Shambhavi Singh, thank you for always being supportive and keeping me balanced when I needed it most; your perspective and compassion have meant a lot these last couple years. I would also like to thank everyone who made life in Charlottesville nothing short of amazing. To my classmates Brian Mead, Katie Pelland, Brittany Earnest, and Sophia Cui, you guys made Charlottesville feel welcoming from the beginning and always made coming to class enjoyable. Scott and Steph Seaman thank you for being great friends who are always up for a hike or a beer. Also, thanks for always watching Sadie and letting Riley teach her how to be a dog. To Jane and Dustin Bauknight, thanks for being great friends and always hosting the best games nights.

This work would not have been possible without my family. Mom and Dad, you two are the most inspirational people I know. From you I learned what it means to be passionate about what you do, thank you for helping me discover my own passion for science (and not architecture). You encouraged me to pursue my dreams and made all of them possible because of your incredible strength and support. To my sisters Saloni and Kalee, you are my pillars. Your brilliance, compassion, and humor have kept me sane through grad school. Thank you for always telling me what I needed to hear and being the best friends anyone could ask for. To the Blais family, thank you for welcoming me into your family and making Virginia feel like home. And last but not least, to Dr. Edik Blais, you are my rock. You helped me navigate graduate school from the very beginning and your support never wavered. Thank you for always cheering me on, telling me how beautiful my data is, and taking Sadie for walks when it was cold outside. You are truly my partner in all things science and my best friend and I cannot wait to spend the rest of my life debating which one is better, R or MatLab, watching Cosmos, and traveling the world with you.

Abstract

Viruses are ancient pathogens that infect host cells and hijack their intracellular machinery. Most viruses, like the cardiotropic picornavirus coxsackievirus B3 (CVB3), engage several intracellular signaling pathways during infection through the expression of viral nucleic acid and proteins. During acute infection, these perturbations serve to condition the cell for optimal viral replication and release, while also avoiding immune surveillance. In chronic infections, where virion release is rare, these same perturbations cause long-term cellular dysfunction. For example, when cardiomyocytes become chronically infected with CVB3 they become elongated, resulting in dilation of the left ventricle. This dilation progresses to heart failure and death as the heart's pumping efficiency diminishes. Studies have shown that the tissue-level consequences of viral infection are not solely dependent on host-pathogen interactions but also on host responses to the environment; specifically, the inflammatory cytokine milieu. During acute infections, pro-inflammatory and antiviral cytokines promote infected cell death and viral clearance. However, prolonged expression of these cytokines is thought to contribute to chronic disease. The work presented in this dissertation asks whether virus-mediated intracellular signaling perturbations influences cellular responses to these inflammatory cues.

We address this question through methods engineering and systems-level experiments. We began by developing a set of quantitative, high-throughput phosphatase activity assays. Protein phosphatases are enzymes that post-translationally modify their substrates to regulate signaling pathway activity. These enzymes can not only affect the activity of multiple pathways but also are important for heart function. Using this assay platform, we show that phosphatase activity is disrupted during the acute phase of CVB3 infection and plays a role in the type I interferon response of infected cells. We then engineer a cellular model of chronic CVB3 infection in cardiac myocytes. Previous models of chronic CVB3 infection utilize non-scalable animal models. By contrast, this in vitro model of chronic infection facilitates subsequent systems-level studies of cellular responses to cytokine stimulation. Using clinically relevant cytokines, we uncover that host transcriptomic adaptions to chronic viral expression result in rewiring of phosphatase responses to inflammatory stimuli. In fact, we observe that stimulus-driven global upregulation of phosphatase activity diminishes host secretion of proinflammatory cytokines. This work has allowed us to not only understand the consequences of host-pathogen interactions during CVB3 infection, but has also unveiled principles underlying the importance of phosphatases in determining cellular behavior.

Chapter 1:

Introduction

1.1. Background

Viruses are ancient pathogens that infect host cells and hijack their intracellular machinery. In response, infected cells send out molecular signals to activate the immune system against infection. The resulting crosstalk between infected and immune cells should eventually lead to viral clearance and resolution of the infection. However, viruses have evolved to disrupt these anti-viral defense systems. For example, some viruses can alter the host-cell's ability to send, receive, and interpret signals from immune cells (1, 2). The ability of viral infection to affect both host and immune cell function from within the host-cell is an interesting systems-level problem. The goal of this work is to understand the effect viral infection has on the complex feedback between the immune system and infected cells.

This dissertation looks specifically at coxsackievirus B3 (CVB3), a common enterovirus known to infect the heart. In humans, as well as mice, genetic background and haplotype is a key determinant of CVB3 mediated disease (3). During acute infection, primary viremia occurs in the enterocytes of the gut. From there, viruses infect the heart tissue where secondary viremia occurs. Rapid replication and progeny release in the heart results in cardiac tissue damage and immune cell infiltration (3, 4). Eventually, the virus is cleared and diseased regions are replaced with fibrotic lesions. In a subset of patients, infections can become chronic: where viral RNA is present in cells but no detectable viral progeny is released (5, 6). In this phase of disease, tissue-level hypertrophy results in left ventricle dilation and lowered pumping efficiency. These clinical symptoms are known as dilated cardiomyopathy (DCM), which is the most common cause of heart transplantation (~50%) (7). Studies have shown that 10-66% of DCM patients have detectable viral RNA in endomyocardial biopsies (5, 6) and a six-fold higher risk of mortality (8). Understanding the divergence in mortality rate from non-viral DCM requires knowledge of CVB3-mediated perturbations at the cellular and tissue level.

CVB3 is a single stranded picornavirus, composed of a small, 3' polyadenylated RNA genome, only 7400 bp, that encodes eleven viral proteins (3). Despite its relative simplicity, CVB3 proteins perturb several host-cell functionalities. In response, host-cells initiate survival, stress, and proinflammatory

signaling pathways (9-11). This can result in the expression of antiviral proteins and chemotactic cytokines (12). Systemic dissemination of cytokines causes cardiac infiltration of activated immune cells, which once activated, induce a cytokine storm (13). The massive production of cytokines affects the function of host-cells as well as cells from both the innate and adaptive immune compartments. These processes occur concurrently in both acutely and chronically infected hearts making it difficult to dissect pathogenic from ameliorating signaling. This dissertation aims to understand how CVB3 infection globally disrupts proinflammatory signaling and the subsequent implications for immune cell crosstalk.

The following chapter will introduce both the intracellular and intercellular aspects of CVB3 infection and myocarditis. Previous studies have catalogued changes in intracellular signaling (9-11, 14, 15), inflammatory response (3, 4, 12, 13, 16), and cardiac structure (17-20) during CVB3 infection but have yet to link host-pathogen interactions to crosstalk between infected cells and the immune system. At the end of this chapter I will describe how we sought to address this knowledge gap through the development of systems-biology tools and models.

1.2. CVB3 Lifecycle

Coxsackievirus B3 is a small, non-enveloped virus consisting of an icosahedral protein capsid packed with the viral genome. In order to enter the cell, the viral capsid must bind its coreceptor, decay accelerating factor (DAF) and its cognate receptor, coxsackievirus and adenovirus receptor (CAR) (Fig 1A) (21). Once bound, the viral capsid destabilizes to deliver the positive strand RNA genome to the host cell cytoplasm (22).

Next, the viral genome is translated through a cap-independent mechanism. Host ribosomes bind CVB3 RNA at a virally encoded internal ribosome entry site (IRES) (23). Thus, translation can be initiated immediately without modification of the viral genome or host ribosomes. CVB3 is translated as a single polypeptide which is then autocatalytically cleaved into eleven mature viral proteins by viral proteases 2A and 3C (Fig 1B) (24). Viral proteins then go on to facilitate CVB3 genome replication.

Viral replication occurs at intracellular membranes that have been co-opted by viral non-structural proteins: 2A, 2B, and 3C (25, 26). Amphipathic alpha-helices anchor these proteins at the membrane. Replication complexes are formed through the association of anchored proteins with viral protein 3B and RNA-dependent RNA polymerase $3D^{pol}$ (Fig 1C). First, a template negative strand is copied from the positive strand genome that was delivered to the cell. Then, many copies of the positive strand genome are made from a single template (27, 28). Negative template strands are copied at a slower rate than positive strand genomes resulting in a ~30:1 ratio of positive to negative strands as the infection progresses (29). Once enough genome and viral proteins have been made, new viral progeny can be formed.

Viral capsid formation requires 60 tetramers of mature VP1, VP2, VP3, and VP4 viral proteins. Encapsidation occurs through a stochastic process in which unstable but fully formed capsids are stabilized upon insertion of a CVB3 genome (Fig 1D). The exact mechanism of insertion is still unknown (3). Once viral burden exceeds a certain threshold, CVB3 progeny is lytically released into the extracellular space (Fig 1E). Recent work also shows non-lytic release of virions in extracellular vesicles, though this has not been shown in the mature cardiomyocytes (30).

Viral processes of translation, replication, and encapsidation disrupt many important host-cell functions throughout the CVB3 life cycle (Fig. 2). Beginning early in infection, viral proteases 2A and 3C cleave not only CVB3 polypeptides but also antiviral signaling proteins and transcription factors (31-33). Further, to promote ribosomal availability for viral RNA, these proteases cleave eIF4G and PABP, proteins necessary for cap-dependent translation of host transcripts (34, 35). Without both of these capabilities, infected cells are unable to initiate interferon signaling – the host's most potent viral defense system.

Viral proteins also disrupt several structures vital to the proper function of cardiomyocytes. Cleavage of dystrophin at the plasma membrane disrupts cellular adhesion and structural integrity of cardiac tissue (36). Similarly, viral protease cleavage of nucleoporins results in loss of nuclear integrity and regulated nuclear-cytoplasmic protein shuttling (37, 38). Non-structural CVB3 proteins also inhibit

ER-Golgi transport of newly synthesized proteins like receptors and cytokines by co-opting their membranes for replication (39, 40). Insertion of the 2B protein into the ER and plasma membrane results in an increase of intracellular calcium (41). Consequently, contractile function of cardiac myocytes is disrupted and cellular membrane integrity breaks down, facilitating the release of new viral particles. Taken together, CVB3 components generated during infection alter the landscape of the host-cell suggesting widespread subversion of intracellular signal processing.

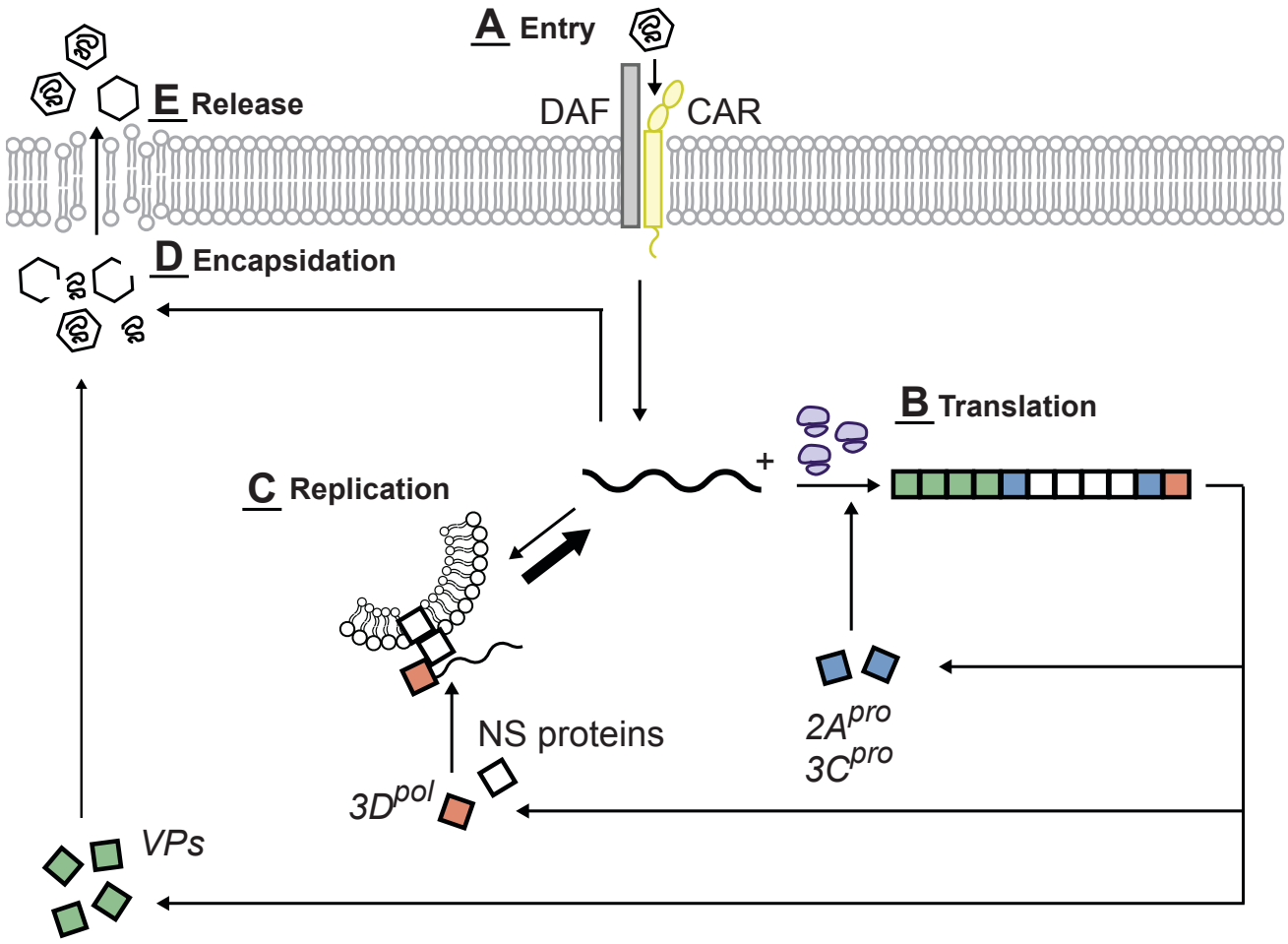

Figure 1. Schematic of CVB3 viral lifecycle
A. Viral entry is mediated by coxsackievirus and adenovirus receptor (CAR) and co-receptor decay accelerating factor (DAF). B. Eleven viral proteins (4 capsid and 7 non-structural (NS)) are translated by host ribosomes. C. Viral non-structural proteins and RNA-dependent RNA polymerase ($3D^{pol}$) create membrane-associated replication complexes where the viral genome is copied. New positive strand genomes can be used for more viral protein translation. D. Positive strand genomes are encapsidated by viral capsid proteins (VPs) into new virions. E. New viral progeny are released as unenveloped viruses.

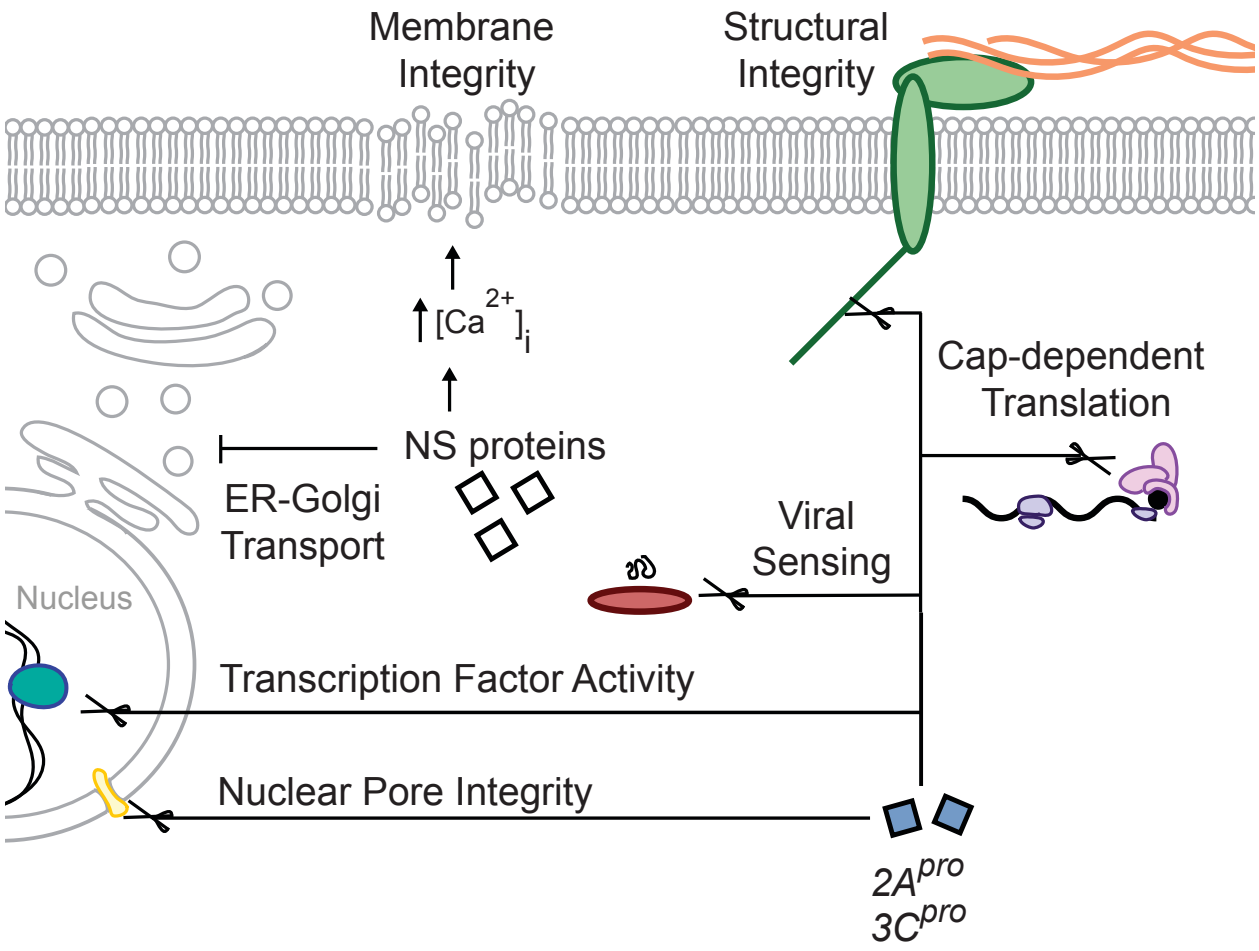

Figure 2. Host-pathogen interactions in CVB3 infection
Viral proteases (blue squares) have the most widely documented host-pathogen interactions. They cleave cap-dependent translation proteins (purple) to make ribosomes available for cap-independent viral translation. They also cleave viral sensors like RIG-I family member MDA5 (red) and transcription factors like NFAT5 (teal). Viral proteases also affect cellular structure through cleavage of ECM binding protein dystrophin (green) and nuclear porins (yellow). Similarly, viral non-structural proteins alter intracellular calcium concentration, disrupting membrane integrity as well as inhibit ER and Golgi function through co-option of organelle membranes for replication centers.

1.3. Intracellular Signaling Pathways in Infection

Previous studies have documented changes in anti-viral, survival, apoptosis, and stress pathways during CVB3 infection. Two of most commonly studied signaling networks include JAK-STAT (42-45) and MAPK (9, 15, 46-48). These pathways are not only important for inflammation but also for viral processes.

Indeed, CVB3 inhibits activation of anti-viral signaling by preventing signal transduction downstream of viral RNA receptors retinoic acid-inducible gene 1 like receptors (RLRs). In an intact system, these viral sensors would signal through NFκB and IRF3 to initiate autocrine factor secretion of proinflammatory cytokines and interferons. CVB3 proteases cleave several members of these signaling pathways including receptors RIG-I and MDA5 as well as signal transducer MAVS (31). In addition, CVB3 non-structural protein 2C and protease 3C prevent activation of NFκB by inhibiting upstream kinase IKKβ activation (49, 50) and cleaving IκBα into a stable inhibitor of NFκB (51), respectively. While viral RNA-sensing autocrine feedback loops are broken by intracellular virus, soluble factor stimulation can still occur through paracrine mechanisms. For example, binding of interferons at the cell surface activates signal transducers and activators of transcription (STATs), resulting in production of interferon stimulated genes (ISGs) that hinder viral, as well as host, processes like activation of ribonucleases that hydrolyze single stranded RNA (52).

In contrast to anti-viral signaling, CVB3 promotes the pro-survival and pro-growth activity of MAPK pathways. In fact, extracellular regulated kinase (ERK) is hyper-activated during infection due to cleavage of upstream RasGAP (53). Concurrently, p38 and jun N-terminal kinase (JNK) stress pathways are independently activated through unknown mechanisms (9, 54). While these pathways have documented importance for viral replication and progeny release, they also control the host inflammation response. MAPK pathways are key integrators of extracellular stimuli like pro-inflammatory cytokines present during viral infection. Downstream activation of transcription factors in Jun, Fos, ATF, and CREB families along with NFκB crosstalk controls the expression and stabilization of many stress-response genes including

cytokines themselves (55-59). With CVB3 disruption of these pathways, it is difficult to predict how host-cells would respond to the extracellular cytokine context during infection.

The net output of these pathways is dependent not only on their activation but also their negative regulation. Protein phosphatases (PPase) are a class of enzymes that remove phosphate groups from their substrates to post-translationally modify their activity (60, 61, 83). Theoretical models have shown that inhibition of phosphatase activity affects the amplitude, duration, and baseline levels of protein activation (62). Further, a single phosphatase can have many targets. As such, PPases are key coordinators of signaling networks and their disruption can have wide-spread effects. This is indeed the case in cardiac tissue where perturbation of protein phosphatase activity leads to pathological changes in contractility and morphology including DCM (63-66). PPases are also disrupted during CVB3 infection: hyperactivation of ERK leads to increased expression of dual specificity phosphatases, DUSP6 and DUSP1, and viral protein 2C regulates substrate recruitment of protein phosphatase 1 (PP1) (50, 67-69). Still, the role of phosphatases in determining cellular behavior during CVB3 infection has not been fully appreciated. The main focus of this dissertation is to understand how PPases targeting JAK-STAT and MAPK pathways influences the release of immuno-modulatory factors in response to pro-inflammatory stimuli.

1.4. Inflammation and Immune cell recruitment during Infection

The cytokine milieu during CVB3 infection is created by both cardiac cells and activated immune cells. This context is a key determinant of tissue damage and progression to chronic infection (3). Thus, studies have focused on understanding the recruitment and activation of immune cells during each phase of CVB3 infection. Many of the studies described below were conducted in mouse models because they faithfully recapitulate human CVB3 infection and susceptibility to chronic disease.

CVB3 infection engages both the innate and adaptive arms of the immune system. Innate immunity consists of fast, non-specific responses to infection. These responses are initiated by pathogen

associated molecular patterns (PAMPs) and damage associated molecular patterns (DAMPs). During CVB3 infection, intracellular presence of viral RNA is recognized as PAMP by RLRs while cellular apoptosis creates DAMPs. These first activate tissue resident cells such as myocytes, fibroblasts, and dendritic cells to release proinflammatory cytokines IL1β, TNFα, IFNγ, and IL6 (70-72). In response, innate immune cells infiltrate the myocardium, namely macrophages (MΦ), neutrophils, and natural killer (NK) cells. Once at the site of infection, MΦ and neutrophils begin phagocytosing apoptotic cells while NK cells kill infected myocytes (71). At the same time, activation of these cells by PAMPs and DAMPs results in amplified cytokine and chemokine production that recruits adaptive immune cells to the heart (3, 71). Adaptive immunity consists of pathogen-specific responses and is responsible for immunological memory wherein a second infection with the same pathogen is rendered less severe. Adaptive immunity is mediated mainly through B cells, which produce antibodies against viral antigens, and CD8+ T cells which specifically kill infected cells. Both of these processes are dependent on cardiac and innate immune cell presentation of CVB3 peptide fragments called antigens. A subset of T cells, called T helper cells, produce arrays of cytokines to further activate both innate and adaptive cells.

Mouse models of CVB3 infection present with a spectrum of immune responses but can be classified as dominated by either type 1 or type 2 immune cell polarization as determined by the cytokine microenvironment. Type 1 responses are characterized by IL2 and IFNγ, while type 2 responses are characterized mainly by IL4 (73). Type 1 immunity stimulates increased phagocytic activity and cytotoxic T cell engagement and activation, while type 2 immunity initiates B cell processes leading to high antibody titers. In mice, type 1 polarization results in severe acute myocarditis and lowered viral titers (54, 74). By contrast, type 2 polarization results in higher viral titers during acute infection but less inflammatory cell induced damage (75-78). The secreted factors typical of each response signal both to immune cells, furthering polarization and activation, and to cardiac cells, stimulating anti-viral and stress signaling. This cyclic crosstalk continues until resolution of infection and contraction of the immune response.

However, in the chronic phase of infection, prolonged expression of cytokines results in cardiomyocyte dysfunction and sustained cardiac infiltration of immune cells (44). We hypothesize that viral rewiring of the cytokine response results in paracrine factor secretion that supports persistent infiltration of activated immune cells. Factors known to be upregulated in the myocardium of chronically infected mice include IFNγ, IL1β, TNFα, MIP1α, and TGFβ (79, 80). Human clinical data has shown elevated TNFα in chronic disease, consistent with observations made in mice (81). The removal of viral genomes through IFNβ treatment results in improved heart function in DCM patients (82). These data suggest that intracellular host-viral mechanisms are initiators of chronic inflammation in the heart. Our understanding of this complex crosstalk can be improved by dissecting viral dysregulation of host-cell signaling and linking this to distal effects on the cytokine milieu.

1.5. Overview of Dissertation

The goal of this dissertation is to quantify phosphatase coordination of cytokine induced signaling pathways in acute and chronic CVB3 infection. The vast intracellular changes to the host during infection combined with the complex microenvironment formed during inflammation necessitates a multifactorial study design to decode the overall effects of viral infection. Thus, we seek to quantify phosphatase activity towards multiple protein substrates in response to multiple perturbations including acute and chronic CVB3 infection and cytokine stimulation. This requires the use of model systems and assay methods compatible with high-throughput and parallelizable experiments.

In chapter 2 of this dissertation we develop a subcellular phosphatase activity assay aimed at quantifying substrate-specific phosphatase activity in cellular lysates. Readouts of this assay tell us the net inactivation of a certain protein substrate by all phosphatases that target it. We optimize twelve phosphatase assays and show that all assays can be conducted from a single lysate extraction of less than 200,000 cells. This allows us to simultaneously assess negative regulation of six intracellular JAK-

STAT and MAPK signaling proteins in two cellular compartments. We apply this to understand CVB3 perturbation of interferon induced phosphatase activity early in acute infection.

In chapter 3 of this dissertation we develop an in vitro model of chronic CVB3 infection using human immortalized cardiomyocytes. Classic mouse models of chronic infection display incomplete penetrance of disease, making high-throughput studies difficult. Further, within the myocardium, chronically infected cells are diffuse; thus, healthy cardiomyocytes would mask viral perturbations in tissue extracts used for the phosphatase activity assay developed in chapter 2. Lastly, a cell-based model allows us to control the extracellular environment such that we can dissect the independent and synergistic effects of stimuli applied. Using this model system, we quantify phosphatase activity in response to two cytokines and two interferons. In parallel, we profile secretion of four paracrine factors in response to these stimuli. We find that clonal adaptations to chronic CVB3 infection alter phosphatase regulation and can affect proinflammatory cytokine secretion.

In chapter 4 of this dissertation we review statistical modeling techniques to infer relationships between large data sets. Large data sets with more variables than observations are distinctly amenable to statistical modeling. While simple correlation analysis can predict spurious relationships between data points, statistical modeling is able to draw out covariates of most importance for further investigation. In chapter 3, we apply these methods to interpret our phosphatase activity and cytokine release data. As a result, we can identify network features that are important for cytokine release and generate hypotheses about which features coordinate cytokine signatures.

In chapter 5, we profile the suitability of iPSC derived cardiomyocytes as a model of acute and chronic coxsackievirus infection. iPSC cardiomyocytes are emerging as the gold-standard for in vitro models of cardiac biology, however, their potential to model viral infections has yet to be determined. We find that iPSC cardiomyocytes initiate ERK and hypertrophic responses to acute CVB3 infection and discuss their potential for modeling chronic CVB3 infection.

Finally, in chapter 6 we discuss the broader implications of this work. The tools developed here are flexible platforms that can facilitate future studies. Further, the conceptual advances in intracellular

determinants of inflammation in cardiac myocytes can be generalized to many inflammatory heart conditions. Lastly, this work stresses the importance of dynamically regulated phosphatases in the coordination of signal transduction and cellular behavior.

1.6. References

1. Kemball, C. C., Harkins, S., Whitmire, J. K., Flynn, C. T., Feuer, R., and Whitton, J. L. (2009) Coxsackievirus B3 inhibits antigen presentation in vivo, exerting a profound and selective effect on the MHC class I pathway. *PLoS Pathog.* 5, e1000618
2. Ploegh, H. L. (1998) Viral strategies of immune evasion. *Science* 280, 248-253
3. Esfandiarei, M., and McManus, B. M. (2008) Molecular biology and pathogenesis of viral myocarditis. *Annu Rev Pathol* 3, 127-155
4. Garmaroudi, F. S., Marchant, D., Hendry, R., Luo, H., Yang, D., Ye, X., Shi, J., and McManus, B. M. (2015) Coxsackievirus B3 replication and pathogenesis. *Future Microbiol* 10, 629-653
5. Bowles, N. E., Richardson, P. J., Olsen, E. G., and Archard, L. C. (1986) Detection of Coxsackie-B-virus-specific RNA sequences in myocardial biopsy samples from patients with myocarditis and dilated cardiomyopathy. *Lancet* 1, 1120-1123
6. Baboonian, C., and Treasure, T. (1997) Meta-analysis of the association of enteroviruses with human heart disease. *Heart* 78, 539-543
7. Chambers, D. C., Yusen, R. D., Cherikh, W. S., Goldfarb, S. B., Kucheryavaya, A. Y., Khusch, K., Levvey, B. J., Lund, L. H., Meiser, B., Rossano, J. W., Stehlik, J., International Society for, H., and Lung, T. (2017) The Registry of the International Society for Heart and Lung Transplantation: Thirty-fourth Adult Lung And Heart-Lung Transplantation Report-2017; Focus Theme: Allograft ischemic time. *J Heart Lung Transplant* 36, 1047-1059
8. Why, H. J., Meany, B. T., Richardson, P. J., Olsen, E. G., Bowles, N. E., Cunningham, L., Freeke, C. A., and Archard, L. C. (1994) Clinical and prognostic significance of detection of enteroviral RNA in the myocardium of patients with myocarditis or dilated cardiomyopathy. *Circulation* 89, 2582-2589
9. Si, X., Luo, H., Morgan, A., Zhang, J., Wong, J., Yuan, J., Esfandiarei, M., Gao, G., Cheung, C., and McManus, B. M. (2005) Stress-activated protein kinases are involved in coxsackievirus B3 viral progeny release. *J. Virol.* 79, 13875-13881
10. Esfandiarei, M., Boroomand, S., Suarez, A., Si, X., Rahmani, M., and McManus, B. (2007) Coxsackievirus B3 activates nuclear factor kappa B transcription factor via a phosphatidylinositol-3 kinase/protein kinase B-dependent pathway to improve host cell viability. *Cell. Microbiol.* 9, 2358-2371
11. Esfandiarei, M., Luo, H., Yanagawa, B., Suarez, A., Dabiri, D., Zhang, J., and McManus, B. M. (2004) Protein kinase B/Akt regulates coxsackievirus B3 replication through a mechanism which is not caspase dependent. *J. Virol.* 78, 4289-4298
12. Seko, Y., Takahashi, N., Yagita, H., Okumura, K., and Yazaki, Y. (1997) Expression of cytokine mRNAs in murine hearts with acute myocarditis caused by coxsackievirus b3. *J. Pathol.* 183, 105-108
13. Matsumori, A., Yamada, T., Suzuki, H., Matoba, Y., and Sasayama, S. (1994) Increased circulating cytokines in patients with myocarditis and cardiomyopathy. *Br Heart J* 72, 561-566
14. Garmaroudi, F. S., Marchant, D., Si, X., Khalili, A., Bashashati, A., Wong, B. W., Tabet, A., Ng, R. T., Murphy, K., Luo, H., Janes, K. A., and McManus, B. M. (2010) Pairwise network mechanisms in the host signaling response to coxsackievirus B3 infection. *Proc Natl Acad Sci U S A* 107, 17053-17058
15. Jensen, K. J., Garmaroudi, F. S., Zhang, J., Lin, J., Boroomand, S., Zhang, M., Luo, Z., Yang, D., Luo, H., McManus, B. M., and Janes, K. A. (2013) An ERK-p38 subnetwork coordinates host cell apoptosis and necrosis during coxsackievirus B3 infection. *Cell Host Microbe* 13, 67-76
16. Huber, S. A., and Lodge, P. A. (1984) Coxsackievirus B-3 myocarditis in Balb/c mice. Evidence for autoimmunity to myocyte antigens. *Am. J. Pathol.* 116, 21-29
17. Cao, Y., Xu, W., and Xiong, S. (2013) Adoptive transfer of regulatory T cells protects against Coxsackievirus B3-induced cardiac fibrosis. *PLoS ONE* 8, e74955
18. Reetoo, K. N., Osman, S. A., Illavia, S. J., Cameron-Wilson, C. L., Banatvala, J. E., and Muir, P. (2000) Quantitative analysis of viral RNA kinetics in coxsackievirus B3-induced murine myocarditis: biphasic pattern of clearance following acute infection, with persistence of residual viral RNA throughout and beyond the inflammatory phase of disease. *J. Gen. Virol.* 81, 2755-2762

19. Wessely, R., Klingel, K., Santana, L. F., Dalton, N., Hongo, M., Jonathan Lederer, W., Kandolf, R., and Knowlton, K. U. (1998) Transgenic expression of replication-restricted enteroviral genomes in heart muscle induces defective excitation-contraction coupling and dilated cardiomyopathy. *J. Clin. Invest.* 102, 1444-1453
20. Liu, P., Aitken, K., Kong, Y. Y., Opavsky, M. A., Martino, T., Dawood, F., Wen, W. H., Kozieradzki, I., Bachmaier, K., Straus, D., Mak, T. W., and Penninger, J. M. (2000) The tyrosine kinase p56lck is essential in coxsackievirus B3-mediated heart disease. *Nat. Med.* 6, 429-434
21. Selinka, H.-C., Wolde, A., Sauter, M., Kandolf, R., and Klingel, K. (2004) Virus-receptor interactions of coxsackie B viruses and their putative influence on cardiotropism. *Med. Microbiol. Immunol.* 193, 127-131
22. Lee, H., Shingler, K. L., Organtini, L. J., Ashley, R. E., Makhov, A. M., Conway, J. F., and Hafenstein, S. (2016) The novel asymmetric entry intermediate of a picornavirus captured with nanodiscs. *Sci Adv* 2, e1501929
23. Pelletier, J., Kaplan, G., Racaniello, V. R., and Sonenberg, N. (1988) Cap-independent translation of poliovirus mRNA is conferred by sequence elements within the 5' noncoding region. *Mol. Cell. Biol.* 8, 1103-1112
24. Jacobson, M. F., and Baltimore, D. (1968) Polypeptide cleavages in the formation of poliovirus proteins. *Proc Natl Acad Sci U S A* 61, 77-84
25. Limpens, R. W. A. L., van der Schaar, H. M., Kumar, D., Koster, A. J., Snijder, E. J., van Kuppeveld, F. J. M., and Bárcena, M. (2011) The transformation of enterovirus replication structures: a three-dimensional study of single- and double-membrane compartments. *MBio* 2
26. Netherton, C., Moffat, K., Brooks, E., and Wileman, T. (2007) A guide to viral inclusions, membrane rearrangements, factories, and viroplasm produced during virus replication. *Adv. Virus Res.* 70, 101-182
27. Paul, A. V., van Boom, J. H., Filippov, D., and Wimmer, E. (1998) Protein-primed RNA synthesis by purified poliovirus RNA polymerase. *Nature* 393, 280-284
28. Steil, B. P., and Barton, D. J. (2009) Cis-active RNA elements (CREs) and picornavirus RNA replication. *Virus Res.* 139, 240-252
29. Novak, J. E., and Kirkegaard, K. (1991) Improved method for detecting poliovirus negative strands used to demonstrate specificity of positive-strand encapsidation and the ratio of positive to negative strands in infected cells. *J. Virol.* 65, 3384-3387
30. Robinson, S. M., Tsueng, G., Sin, J., Mangale, V., Rahawi, S., McIntyre, L. L., Williams, W., Kha, N., Cruz, C., Hancock, B. M., Nguyen, D. P., Sayen, M. R., Hilton, B. J., Doran, K. S., Segall, A. M., Wolkowicz, R., Cornell, C. T., Whitton, J. L., Gottlieb, R. A., and Feuer, R. (2014) Coxsackievirus B exits the host cell in shed microvesicles displaying autophagosomal markers. *PLoS Pathog.* 10, e1004045
31. Feng, Q., Langereis, M. A., Lork, M., Nguyen, M., Hato, S. V., Lanke, K., Emdad, L., Bhoopathi, P., Fisher, P. B., Lloyd, R. E., and van Kuppeveld, F. J. M. (2014) Enterovirus 2Apro targets MDA5 and MAVS in infected cells. *J. Virol.* 88, 3369-3378
32. Mukherjee, A., Morosky, S. A., Delorme-Axford, E., Dybdahl-Sissoko, N., Oberste, M. S., Wang, T., and Coyne, C. B. (2011) The coxsackievirus B 3C protease cleaves MAVS and TRIF to attenuate host type I interferon and apoptotic signaling. *PLoS Pathog.* 7, e1001311
33. Qiu, Y., Ye, X., Zhang, H. M., Hanson, P., Zhao, G., Tong, L., Xie, R., and Yang, D. (2017) Cleavage of osmosensitive transcriptional factor NFAT5 by Coxsackieviral protease 2A promotes viral replication. *PLoS Pathog.* 13, e1006744
34. Kerekatte, V., Keiper, B. D., Badorff, C., Cai, A., Knowlton, K. U., and Rhoads, R. E. (1999) Cleavage of Poly(A)-binding protein by coxsackievirus 2A protease in vitro and in vivo: another mechanism for host protein synthesis shutoff? *J. Virol.* 73, 709-717
35. Hanson, P. J., Ye, X., Qiu, Y., Zhang, H. M., Hemida, M. G., Wang, F., Lim, T., Gu, A., Cho, B., Kim, H., Fung, G., Granville, D. J., and Yang, D. (2016) Cleavage of DAP5 by coxsackievirus B3 2A protease facilitates viral replication and enhances apoptosis by altering translation of IRES-containing genes. *Cell Death Differ.* 23, 828-840

36. Badorff, C., Berkely, N., Mehrotra, S., Talhouk, J. W., Rhoads, R. E., and Knowlton, K. U. (2000) Enteroviral protease 2A directly cleaves dystrophin and is inhibited by a dystrophin-based substrate analogue. *J. Biol. Chem.* 275, 11191-11197
37. Belov, G. A., Evstafieva, A. G., Rubtsov, Y. P., Mikitas, O. V., Vartapetian, A. B., and Agol, V. I. (2000) Early alteration of nucleocytoplasmic traffic induced by some RNA viruses. *Virology* 275, 244-248
38. Belov, G. A., Lidsky, P. V., Mikitas, O. V., Egger, D., Lukyanov, K. A., Bienz, K., and Agol, V. I. (2004) Bidirectional increase in permeability of nuclear envelope upon poliovirus infection and accompanying alterations of nuclear pores. *J Virol* 78, 10166-10177
39. Cornell, C. T., Kiosses, W. B., Harkins, S., and Whitton, J. L. (2006) Inhibition of protein trafficking by coxsackievirus b3: multiple viral proteins target a single organelle. *J. Virol.* 80, 6637-6647
40. Doedens, J. R., and Kirkegaard, K. (1995) Inhibition of cellular protein secretion by poliovirus proteins 2B and 3A. *EMBO J.* 14, 894-907
41. van Kuppeveld, F. J., Hoenderop, J. G., Smeets, R. L., Willems, P. H., Dijkman, H. B., Galama, J. M., and Melchers, W. J. (1997) Coxsackievirus protein 2B modifies endoplasmic reticulum membrane and plasma membrane permeability and facilitates virus release. *EMBO J.* 16, 3519-3532
42. Ruppert, V., Meyer, T., Pankuweit, S., Jonsdottir, T., and Maisch, B. (2008) Activation of STAT1 transcription factor precedes up-regulation of coxsackievirus-adenovirus receptor during viral myocarditis. *Cardiovasc. Pathol.* 17, 81-92
43. Wessely, R., Klingel, K., Knowlton, K. U., and Kandolf, R. (2001) Cardioselective infection with coxsackievirus B3 requires intact type I interferon signaling: implications for mortality and early viral replication. *Circulation* 103, 756-761
44. Abston, E. D., Coronado, M. J., Bucek, A., Bedja, D., Shin, J., Kim, J. B., Kim, E., Gabrielson, K. L., Georgakopoulos, D., Mitzner, W., and Fairweather, D. (2012) Th2 regulation of viral myocarditis in mice: different roles for TLR3 versus TRIF in progression to chronic disease. *Clin Dev Immunol* 2012, 129486
45. Deonarain, R., Cerullo, D., Fuse, K., Liu, P. P., and Fish, E. N. (2004) Protective role for interferon-beta in coxsackievirus B3 infection. *Circulation* 110, 3540-3543
46. Cunningham, K. A., Chapman, N. M., and Carson, S. D. (2003) Caspase-3 activation and ERK phosphorylation during CVB3 infection of cells: influence of the coxsackievirus and adenovirus receptor and engineered variants. *Virus Res.* 92, 179-186
47. Luo, H., Yanagawa, B., Zhang, J., Luo, Z., Zhang, M., Esfandiarei, M., Carthy, C., Wilson, J. E., Yang, D., and McManus, B. M. (2002) Coxsackievirus B3 replication is reduced by inhibition of the extracellular signal-regulated kinase (ERK) signaling pathway. *J. Virol.* 76, 3365-3373
48. Dai, Q., Zhang, D., Yu, H., Xie, W., Xin, R., Wang, L., Xu, X., He, X., Xiong, J., Sheng, H., Zhang, L., Zhang, K., and Hu, X. (2017) Berberine Restricts Coxsackievirus B Type 3 Replication via Inhibition of c-Jun N-Terminal Kinase (JNK) and p38 MAPK Activation In Vitro. *Med. Sci. Monit.* 23, 1448-1455
49. Li, Q., Zheng, Z., Liu, Y., Zhang, Z., Liu, Q., Meng, J., Ke, X., Hu, Q., and Wang, H. (2016) 2C Proteins of Enteroviruses Suppress IKKβ Phosphorylation by Recruiting Protein Phosphatase 1. *J. Virol.* 90, 5141-5151
50. Zheng, Z., Li, H., Zhang, Z., Meng, J., Mao, D., Bai, B., Lu, B., Mao, P., Hu, Q., and Wang, H. (2011) Enterovirus 71 2C protein inhibits TNF-α-mediated activation of NF-κB by suppressing IκB kinase β phosphorylation. *J. Immunol.* 187, 2202-2212
51. Zaragoza, C., Saura, M., Padalko, E. Y., Lopez-Rivera, E., Lizarbe, T. R., Lamas, S., and Lowenstein, C. J. (2006) Viral protease cleavage of inhibitor of kappaBalpha triggers host cell apoptosis. *Proc Natl Acad Sci U S A* 103, 19051-19056
52. García-Sastre, A., and Biron, C. A. (2006) Type 1 interferons and the virus-host relationship: a lesson in détente. *Science* 312, 879-882
53. Huber, M., Watson, K. A., Selinka, H. C., Carthy, C. M., Klingel, K., McManus, B. M., and Kandolf, R. (1999) Cleavage of RasGAP and phosphorylation of mitogen-activated protein kinase in the course of coxsackievirus B3 replication. *J. Virol.* 73, 3587-3594

54. Marchant, D., Si, X., Luo, H., McManus, B., and Yang, D. (2008) The impact of CVB3 infection on host cell biology. *Curr. Top. Microbiol. Immunol.* 323, 177-198
55. Johnson, G. L., and Lapadat, R. (2002) Mitogen-activated protein kinase pathways mediated by ERK, JNK, and p38 protein kinases. *Science* 298, 1911-1912
56. Martin, T., Cardarelli, P. M., Parry, G. C., Felts, K. A., and Cobb, R. R. (1997) Cytokine induction of monocyte chemoattractant protein-1 gene expression in human endothelial cells depends on the cooperative action of NF-kappa B and AP-1. *Eur. J. Immunol.* 27, 1091-1097
57. Gupta, S., Campbell, D., Dérijard, B., and Davis, R. J. (1995) Transcription factor ATF2 regulation by the JNK signal transduction pathway. *Science* 267, 389-393
58. Raingeaud, J., Gupta, S., Rogers, J. S., Dickens, M., Han, J., Ulevitch, R. J., and Davis, R. J. (1995) Pro-inflammatory cytokines and environmental stress cause p38 mitogen-activated protein kinase activation by dual phosphorylation on tyrosine and threonine. *J. Biol. Chem.* 270, 7420-7426
59. Hess, J., Angel, P., and Schorpp-Kistner, M. (2004) AP-1 subunits: quarrel and harmony among siblings. *J. Cell. Sci.* 117, 5965-5973
60. Tonks, N. K. (2006) Protein tyrosine phosphatases: from genes, to function, to disease. *Nat. Rev. Mol. Cell Biol.* 7, 833-846
61. Owens, D. M., and Keyse, S. M. (2007) Differential regulation of MAP kinase signalling by dual-specificity protein phosphatases. *Oncogene* 26, 3203-3213
62. Heinrich, R., Neel, B. G., and Rapoport, T. A. (2002) Mathematical models of protein kinase signal transduction. *Mol. Cell* 9, 957-970
63. Pathak, A., del Monte, F., Zhao, W., Schultz, J.-E., Lorenz, J. N., Bodi, I., Weiser, D., Hahn, H., Carr, A. N., Syed, F., Mavila, N., Jha, L., Qian, J., Marreez, Y., Chen, G., McGraw, D. W., Heist, E. K., Guerrero, J. L., DePaoli-Roach, A. A., Hajjar, R. J., and Kranias, E. G. (2005) Enhancement of cardiac function and suppression of heart failure progression by inhibition of protein phosphatase 1. *Circ. Res.* 96, 756-766
64. Gergs, U., Boknik, P., Buchwalow, I., Fabritz, L., Matus, M., Justus, I., Hanske, G., Schmitz, W., and Neumann, J. (2004) Overexpression of the catalytic subunit of protein phosphatase 2A impairs cardiac function. *J. Biol. Chem.* 279, 40827-40834
65. Auger-Messier, M., Accornero, F., Goonasekera, S. A., Bueno, O. F., Lorenz, J. N., van Berlo, J. H., Willette, R. N., and Molkentin, J. D. (2013) Unrestrained p38 MAPK activation in Dusp1/4 double-null mice induces cardiomyopathy. *Circ. Res.* 112, 48-56
66. Purcell, N. H., Wilkins, B. J., York, A., Saba-El-Leil, M. K., Meloche, S., Robbins, J., and Molkentin, J. D. (2007) Genetic inhibition of cardiac ERK1/2 promotes stress-induced apoptosis and heart failure but has no effect on hypertrophy in vivo. *Proc Natl Acad Sci U S A* 104, 14074-14079
67. Ekerot, M., Stavridis, M. P., Delavaine, L., Mitchell, M. P., Staples, C., Owens, D. M., Keenan, I. D., Dickinson, R. J., Storey, K. G., and Keyse, S. M. (2008) Negative-feedback regulation of FGF signalling by DUSP6/MKP-3 is driven by ERK1/2 and mediated by Ets factor binding to a conserved site within the DUSP6/MKP-3 gene promoter. *Biochem J* 412, 287-298
68. Kondoh, K., and Nishida, E. (2007) Regulation of MAP kinases by MAP kinase phosphatases. *Biochim. Biophys. Acta* 1773, 1227-1237
69. Sarközi, R., Miller, B., Pollack, V., Feifel, E., Mayer, G., Sorokin, A., and Schramek, H. (2007) ERK1/2-driven and MKP-mediated inhibition of EGF-induced ERK5 signaling in human proximal tubular cells. *J. Cell. Physiol.* 211, 88-100
70. Shioi, T., Matsumori, A., and Sasayama, S. (1996) Persistent expression of cytokine in the chronic stage of viral myocarditis in mice. *Circulation* 94, 2930-2937
71. Huber, S. (2008) Host immune responses to coxsackievirus B3. *Curr. Top. Microbiol. Immunol.* 323, 199-221
72. Leipner, C., Grün, K., Schneider, I., Glück, B., Sigusch, H. H., and Stelzner, A. (2004) Coxsackievirus B3-induced myocarditis: differences in the immune response of C57BL/6 and Balb/c mice. *Med. Microbiol. Immunol.* 193, 141-147

73. Spellberg, B., and Edwards, J. E. (2001) Type 1/Type 2 immunity in infectious diseases. *Clin. Infect. Dis.* 32, 76-102
74. Fairweather, D., Frisancho-Kiss, S., Yusung, S. A., Barrett, M. A., Davis, S. E., Steele, R. A., Gatewood, S. J. L., and Rose, N. R. (2005) IL-12 protects against coxsackievirus B3-induced myocarditis by increasing IFN-gamma and macrophage and neutrophil populations in the heart. *J. Immunol.* 174, 261-269
75. Fairweather, D., Stafford, K. A., and Sung, Y. K. (2012) Update on coxsackievirus B3 myocarditis. *Curr Opin Rheumatol* 24, 401-407
76. Yue, Y., Gui, J., Ai, W., Xu, W., and Xiong, S. (2011) Direct gene transfer with IP-10 mutant ameliorates mouse CVB3-induced myocarditis by blunting Th1 immune responses. *PLoS ONE* 6, e18186
77. Huber, S. A., Polgar, J., Schultheiss, P., and Schwimmbeck, P. (1994) Augmentation of pathogenesis of coxsackievirus B3 infections in mice by exogenous administration of interleukin-1 and interleukin-2. *J. Virol.* 68, 195-206
78. Huber, S. A., and Pfaeffle, B. (1994) Differential Th1 and Th2 cell responses in male and female BALB/c mice infected with coxsackievirus group B type 3. *J. Virol.* 68, 5126-5132
79. Glück, B., Schmidtke, M., Merkle, I., Stelzner, A., and Gemsa, D. (2001) Persistent expression of cytokines in the chronic stage of CVB3-induced myocarditis in NMRI mice. *J. Mol. Cell. Cardiol.* 33, 1615-1626
80. Neumann, D. A., Lane, J. R., Allen, G. S., Herskowitz, A., and Rose, N. R. (1993) Viral myocarditis leading to cardiomyopathy: do cytokines contribute to pathogenesis? *Clin Immunol Immunopathol* 68, 181-190
81. Satoh, M., Tamura, G., Segawa, I., Tashiro, A., Hiramori, K., and Satodate, R. (1996) Expression of cytokine genes and presence of enteroviral genomic RNA in endomyocardial biopsy tissues of myocarditis and dilated cardiomyopathy. *Virchows Arch.* 427, 503-509
82. Kühl, U., Pauschinger, M., Schwimmbeck, P. L., Seeberg, B., Lober, C., Noutsias, M., Poller, W., and Schultheiss, H.-P. (2003) Interferon-beta treatment eliminates cardiotropic viruses and improves left ventricular function in patients with myocardial persistence of viral genomes and left ventricular dysfunction. *Circulation* 107, 2793-2798
83. Brautigan, D. L. (2013) Protein Ser/Thr phosphatases--the ugly ducklings of cell signalling. *FEBS J* 280, 324-345

Chapter 2:

Profiling subcellular protein phosphatase responses to coxsackievirus B3 infection of cardiomyocytes

Millie Shah‡, Christian M. Smolko‡, Sarah Kinicki‡, Zachary D. Chapman§,
David L. Brautigan¶, and Kevin A. Janes‡ll

From the ‡Department of Biomedical Engineering, the §Department of Chemistry, and the ¶Center for Cell Signaling and Department of Microbiology, Immunology, and Cancer Biology, University of Virginia School of Medicine Charlottesville, VA 22908

*This work was published in Molecular Cellular Proteomics Apr 2017

Abbreviations page:

Abbreviation	Definition
ANOVA	analysis of variance
ARE	AU-rich element
CAR	coxsackievirus and adenovirus receptor
Clv. Casp3	cleaved caspase 3
CREB	CAMP responsive element binding protein
CV	coefficient of variation
CVB3	coxsackievirus B3
DAF	decay accelerating factor
DUSP	dual specificity phosphatase
EGF	epidermal growth factor
eIF4G	eukaryotic translation initiation factor 4 gamma
ERK2	extracellular signal-regulated kinase 2
G6P	glucose-6-phosphate
Gluc	glucose
HK or Hexo	hexokinase
HSP90	heat shock protein 90 kDa
HRP	horseradish peroxidase
IFN	interferon
JAK	Janus kinase
JNK1	JUN N-Terminal kinase
MAPK	mitogen-activated protein kinase
MAVS	mitochondrial antiviral signaling protein
MCLR	microcystin-LR
MK2	mitogen-activated protein kinase-activated protein kinase 2
MOI	multiplicity of infection
NaPP	sodium pyrophosphate
Na_3VO_4	sodium orthovanadate
NP40	Nonidet P-40
PFA	paraformaldehyde
PFU	plaque forming unit
PP1	protein phosphatase 1
PP2A	protein phosphatase 2A
PTP	protein tyrosine phosphatase
RIPA	radioimmunoprecipitation assay buffer
SDS	sodium dodecyl sulfate
STAT1	signal transducer and activator of transcription 1
SV40	Simian virus 40
VP1	viral protein 1
WB	western blot

Summary

Cellular responses to stimuli involve dynamic and localized changes in protein kinases and phosphatases. Here, we report a generalized functional assay for high-throughput profiling of multiple protein phosphatases with subcellular resolution and apply it to analyze coxsackievirus B3 (CVB3) infection counteracted by interferon signaling. Using on-plate cell fractionation optimized for adherent cells, we isolate protein extracts containing active endogenous phosphatases from cell membranes, the cytoplasm, and the nucleus. The extracts contain all major classes of protein phosphatases and catalyze dephosphorylation of plate-bound phosphosubstrates in a microtiter format, with cellular activity quantified at the endpoint by phosphospecific ELISA. The platform is optimized for six phosphosubstrates (ERK2, JNK1, p38α, MK2, CREB, and STAT1) and measures specific activities from extracts of fewer than 50,000 cells. The assay was exploited to examine viral and antiviral signaling in AC16 cardiomyocytes, which we show can be engineered to serve as susceptible and permissive hosts for CVB3. Phosphatase responses were profiled in these cells by completing a full-factorial experiment for CVB3 infection and type I/II interferon signaling. Over 850 functional measurements revealed several independent, subcellular changes in specific phosphatase activities. During CVB3 infection, we found that type I interferon signaling increases subcellular JNK1 phosphatase activity, inhibiting nuclear JNK1 activity that otherwise promotes viral protein synthesis in the infected host cell. Our assay provides a high-throughput way to capture perturbations in important negative regulators of intracellular signal-transduction networks.

2.1. Introduction

Protein phosphorylation is a critical component of cellular signal transduction (1, 2). In response to extracellular stimulation by cytokines, hormones, and environmental stresses, protein kinases catalyze phosphorylation events that alter substrate activity, protein localization, gene expression, and cell phenotype (Fig. 1). To reverse these events and return the cell to a resting state, protein phosphatases dephosphorylate many phosphoprotein substrates (3-5). Phosphatase abundance and activity determine the extent of constitutive signaling (6) as well as the magnitude and duration of pathway stimulation (7). Accordingly, misregulated protein phosphatases have been implicated in many diseases, including cardiomyopathy, cancer, and inflammatory conditions (8-11).

There are ~500 protein kinases and ~180 protein phosphatases in the human genome, indicating that phosphatases must target a larger breadth of substrates (12). The catalytic subunits of the protein phosphatases PP1 and PP2A dephosphorylate most phospho-Ser/Thr-containing proteins, with selectivity conferred by regulatory subunits and subcellular localization (13). In contrast, dual-specificity phosphatases (DUSPs) hydrolyze phospho-Tyr residues paired with phospho-Ser/Thr sites, narrowly targeting bisphosphorylated MAP kinases (MAPKs) ERK, JNK, and p38 through kinase-interaction motifs (14) (Figure 1). DUSP targeting is further refined by subcellular localization and the nucleocytoplasmic shuttling characteristics of each MAPK (5, 15-19). DUSPs comprise part of a larger family of protein tyrosine phosphatases (PTPs) that dephosphorylate phospho-Tyr exclusively (3). Receptor-like PTPs have access to substrates near cell membranes, whereas nontransmembrane PTPs act elsewhere within the cell (Figure 1). Phosphatases can dephosphorylate a variety of substrates, but multiple phosphatases may also converge upon the same substrate. For example, the bisphosphorylated site in MAPKs is deactivated by DUSPs but also by the coordinate action of Ser/Thr phosphatases and PTPs (20). The extent of targeting is dictated by the abundance of protein phosphatase and phosphosubstrate along with their respective proximity in the cell (4, 5, 21, 22). The

redundancy, promiscuity, and multi-layered regulation of protein phosphatases make it challenging to define their specific roles in intracellular signaling (23).

Monitoring cellular protein dephosphorylation events would be greatly aided by high-throughput methods that capture multiple mechanisms of phosphatase regulation. In typical activity assays, phosphatases are purified from extracts and measured using a synthetic phosphopeptide substrate (24-27). This strategy captures changes in protein phosphatase abundance, but the enzyme may lose endogenous regulators during the purification, and subcellular localization is usually homogenized. It is also doubtful that short, unstructured phosphopeptides accurately reflect phosphatase activity in the same way as full-length phosphoproteins. Endogenous phosphatase activity measurements are possible by incubating total cell extracts with ^{32}P-radiolabeled phosphoproteins (28). However, robust protein phosphatase activities or heavily labeled substrates are required; thus, the approach does not scale well to dozens or hundreds of samples. We previously developed a substrate-focused protein phosphatase activity assay using phosphorylated MAPKs and homogenized cellular extracts in a phospho-ELISA format (29). Phosphatase activity in the extract was measured as the decrease in phosphorylated full-length recombinant MAPK substrates adsorbed to a 96-well plate. Although this approach captured substrate-phosphatase interactions, it could not characterize subcellular regulation of protein phosphatase activity and only included MAPKs. A true multi-pathway protein phosphatase assay with subcellular resolution would provide a better systems-level view of how signal transduction is negatively regulated.

Here, we introduce a high-throughput assay that now measures substrate dephosphorylation by all major classes of protein phosphatases in different biochemically defined subcellular compartments. We begin with a high-throughput, scalable lysis procedure that collects paired saponin- and detergent-soluble extracts containing active protein phosphatases from adherent cells. The activity of subcellular phosphatases is then quantified by phospho-ELISA using a panel of recognized full-length phosphoproteins. Building upon our past success with phosphorylated MAPKs (29), we add three new phosphosubstrates—phospho-MK2 (Thr^{334}), phospho-CREB (Ser^{133}), and phospho-STAT1 (Tyr^{701})—

each with distinct patterns of localization and targeting by protein phosphatase enzymes (Figure 1). Together, these substrates provide a subcellular phosphatase activity signature for the cellular response to growth factors, cytokines, and environmental stress.

As a prototypical cellular stress that engages several host-cell signaling pathways, we investigated changes in protein phosphatase activities during acute viral infection. Coxsackievirus B3 (CVB3) is a cardiotropic picornavirus that causes myocarditis in infants and young children (30, 31). The CVB3 genome encodes neither protein kinases nor phosphatases but widely alters the phosphorylation state of the infected host cell (32-36). For example, CVB3 infection cleaves a negative regulator of Ras, which gives rise to ERK phosphorylation that is important for viral replication (37-40). Various protein phosphatases are required for early CVB3 infection (41), and CVB3-encoded proteins can also modify host phosphatase activity directly. For example, viral protein 2C forms a complex with PP1 to inhibit IKKβ phosphorylation and NF-κB signaling (42). Furthermore, CVB3 infection induces expression of proinflammatory and antiviral cytokines, such as TNF, IL-1, and interferons, in both cardiomyocytes and infiltrating immune cells (43, 44) (Figure 1). Type I and Type II interferons activate STATs resulting in partially overlapping antiviral transcriptional responses that combat RNA viruses such as CVB3 (45, 46). Understanding the degree to which CVB3 infection intersects with interferons is important for more systematic profiling of protein phosphatase cross-regulation by combinations of cytokines and viral pathogens.

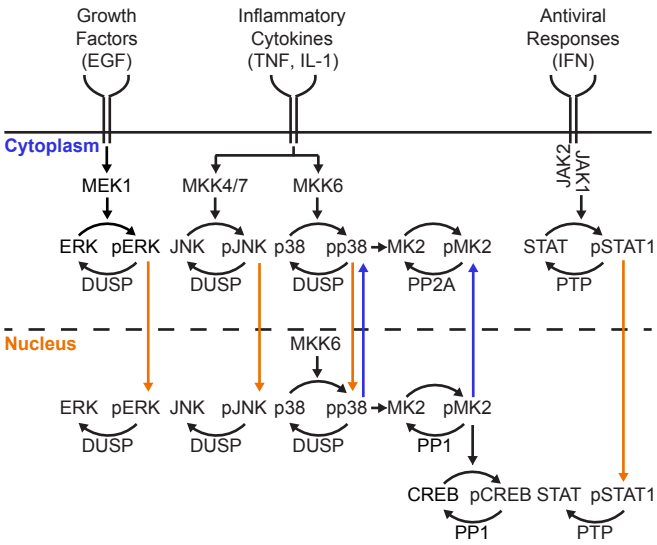

Figure 1. Subcellular phosphatase activities reset intracellular signaling triggered by growth factors, proinflammatory cytokines, and pathogenic stresses.
Hierarchical signaling cascades initiated by extracellular stimuli cause downstream protein phosphorylation. Upon phosphorylation, some signaling proteins are shuttled into (orange arrows) or out of (blue arrows) the nucleus. Compartment- and substrate-specific phosphatases dephosphorylate activated proteins thereby returning proteins to their resting compartment.

2.2. Results

Reliable Subcellular Extraction for Protein Phosphatase Activity Profiling

Preserving endogenous protein phosphatase activity from different subcellular fractions is technically challenging. Detergents rapidly extract proteins but lyse subcellular compartments indiscriminately (59). Cell lysis itself can inactivate protein phosphatases by oxidation, and phosphatase activity in lysates may be offset by constitutive kinase activities that co-extract (60, 61). We surmounted all of these hurdles by heavily modifying our whole-cell extraction procedure (29) originally developed to preserve the activity of protein phosphatases targeting MAPKs (Figure 2*A*, Experimental Procedures). Adherent cells are gently permeabilized without mechanical disruption by using a saponin extraction buffer to permeabilize cells by displacing cholesterol selectively in cell membranes (62). The nuclear envelope has negligible cholesterol and thus only small nuclear proteins (< 40 kDa) that freely diffuse through nuclear pore complexes will be released with saponin extraction (59, 63). Cells are washed with saponin-containing PBS and then incubated briefly with phosphate-free Nonidet P-40 (NP40) extraction buffer to solubilize lipid bilayers, including the nuclear envelope. The NP40 buffer also contains isotonic NaCl to partially disrupt electrostatic interactions between nuclear protein complexes and DNA. Both extraction buffers were supplemented with hexokinase and glucose to consume ATP and therefore prevent kinase-catalyzed phosphorylation in the extract (see below). Multiple reducing agents were included in both buffers to preserve the active site Cys of extracted protein phosphatases. Collectively, we reasoned that these modifications to the lysis procedure should yield two matched biochemical fractions—a saponin extract (SE) and an NP40 extract (NE)—which each retain the activity of endogenous protein phosphatases.

We first evaluated whether the on-plate extraction procedure accurately fractionated subcellular proteins in multiple biological settings. Using cell lines of breast (MCF10A-5E), cervical (HeLa), colonic (HT29) and cardiac (AC16-CAR) origin, we immunoblotted SE and NE fractions for multiple proteins that strongly localize to the cytoplasm or the nucleus (Figure 2*B*). We found that the dual-specificity

kinase MEK and the NF-κB inhibitor IκBα were restricted to the SE fraction, as expected (64, 65). The lack of MEK and IκBα immunoreactivity in the NE fractions confirmed that the intermediate washing steps completely removed residual SE proteins from the plate. To assess the overall fractionation efficiency, we extracted the remaining insoluble (I) material on the cell culture plate with Laemmli sample buffer (66) and noted that pure SE proteins were almost completely removed. Reciprocally, the DNA-repair enzyme PARP and the transcription factor JunD were only detectable in the NE and I fractions (Figure 2*B*). These results indicated that the preceding permeabilization and washing steps retained the proper localization of nuclear proteins within the size restriction of the nuclear pore complex (67), while recognizing that proteins bound tightly to DNA and chromatin-associated factors would not be completely removed by NE fractionation.

The extraction characteristics of SE and NE proteins extended to endogenous protein phosphatases (Figure 2*C*). The cytoplasmic DUSP MKP3 resided entirely in the SE fraction, whereas the Ser/Thr phosphatases PP1 and PP2A were distributed in both SE and NE fractions with overall efficiencies of ~53 ± 17% and ~81 ± 11% respectively. The extraction of marker proteins and protein phosphatases varied across cell lines but did not change when cells were stimulated with epidermal growth factor (EGF) (Figure 3). Replicated fractionation of resting and EGF-stimulated cells further showed that partitioning of endogenous protein phosphatases into SE and NE fractions was highly reproducible (Figure 4). We concluded that the biochemical fractionation strategy (Figure 2*A*) robustly isolates proteins from distinct subcellular compartments.

To assess protein separation more broadly, we ectopically expressed various V5-tagged constructs in AC16-CAR cells and repeated the fractionation. The DUSP MKP7 predominantly resided in the SE fraction (Figure 5*A*), consistent with the cytoplasmic localization reported in previous overexpression studies (68). The nuclear regulatory subunit of PP1, NIPP1 (69), was also mostly extracted in the SE fraction probably due to its small size and passive diffusion through nuclear pores (Figure 5*B*). However, ~17% was still detectable in the NE fraction, including a faster migrating form

that was exclusively NE resident. We observed a similarly interesting fractionation of the myristoylated JNK-stimulatory phosphatase, JSP1, whose localization has been reported to be perinuclear (70). A slower migrating form of JSP1 resided in the SE fraction, whereas a doublet was apparent in the NE fraction, which contained a faster migrating JSP1 that was also partially insoluble (Figure 5*C*). Curiously, the transmembrane phosphatase PTP-SL, which localizes to intracellular vesicles (71-74), was completely solubilized in the SE fraction (Figure 5*D*), suggesting that it may reside in a population of vesicles that is especially cholesterol rich. By contrast, the tight junction-associated transmembrane receptor CAR was negligibly extracted by saponin but solubilized efficiently in the NE fraction as expected (Figure 5*E*). The V5-tagging experiments together indicated that the SE and NE fractions access many compartments within cells.

The precision of subcellular extraction was determined in different culture formats by measuring total extracted protein content with o-pthalaldehyde, a fluorogenic reagent that is compatible with strong reducing conditions (75). We found that on-plate SE and NE extraction was consistent from day to day and compatible with 10-cm, 6-well, 12-well, and 24-well formats (Figure 6*A*-*B*). Total protein extraction decreased in the smaller formats, likely due to reduced shear forces and mixing during incubations on the platform rocker (see Experimental Procedures). However, the impact was equivalent for the SE and NE extraction steps, such that the ratio of the two fractions was roughly equal across all formats (Figure 6*C*). The overall generality of the on-plate extraction procedure ensured that the method could be rapidly adapted to different biological applications.

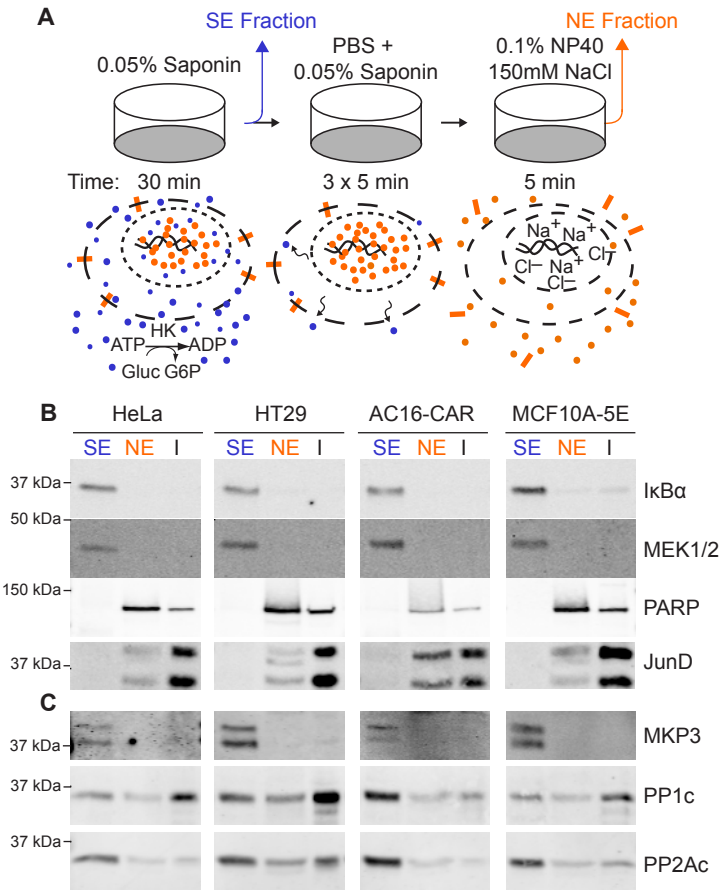

Figure 2. On-plate subcellular fractionation of adherent human cells.
A, Extraction procedure schematic for collection of cytoplasmic proteins (blue circles), nuclear proteins (orange and small blue circles), and transmembrane proteins (orange rectangles) from adherent cell cultures. HK, hexokinase. Gluc, glucose. G6P, glucose-6-phosphate. *B-C*, Immunoblot comparison of saponin extracts (SE), NP40 extracts (NE) and insoluble proteins (I) for cytoplasmic (MEK1/2 and IκBα) and nuclear (PARP and JunD) proteins (*B*) as well as endogenous MKP3 phosphatase, the catalytic subunit of PP1 (PP1c) phosphatase, and the catalytic subunit of PP2A (PP2Ac) phosphatase (*C*) in the indicated human cell lines.

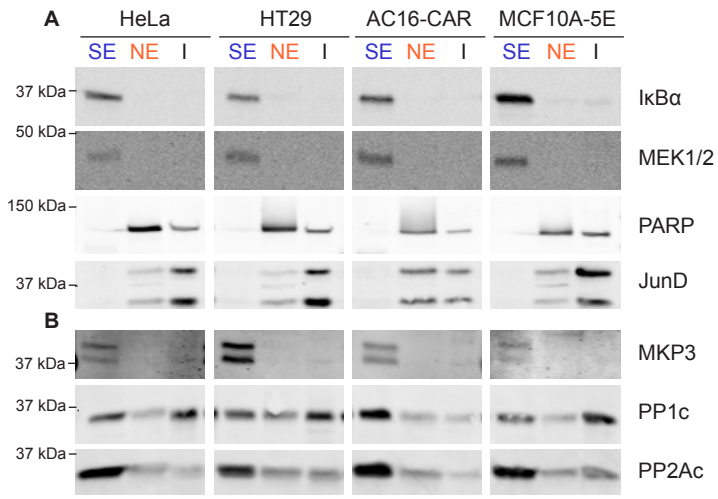

Figure 3. On-plate subcellular fractionation of adherent human cells is unchanged upon stimulation with EGF.
A-B, Immunoblot comparison of saponin extracts (SE), NP40 extracts (NE) and insoluble proteins (I) of cytoplasmic (MEK1/2 and IκBα) and nuclear (PARP and JunD) proteins (*A*) as well as endogenous MKP3, PP1 (catalytic subunit, PP1c), and PP2A (catalytic subunit, PP2Ac) phosphatases (*B*) in the indicated human cell lines. Cells were stimulated with 100 ng/mL EGF for 1 hour before subcellular fractionation. Equal volumes of the SE, NE, and I fractions were loaded for each sample and the immunoblots are representative of *n* = 3 independent fractionations.

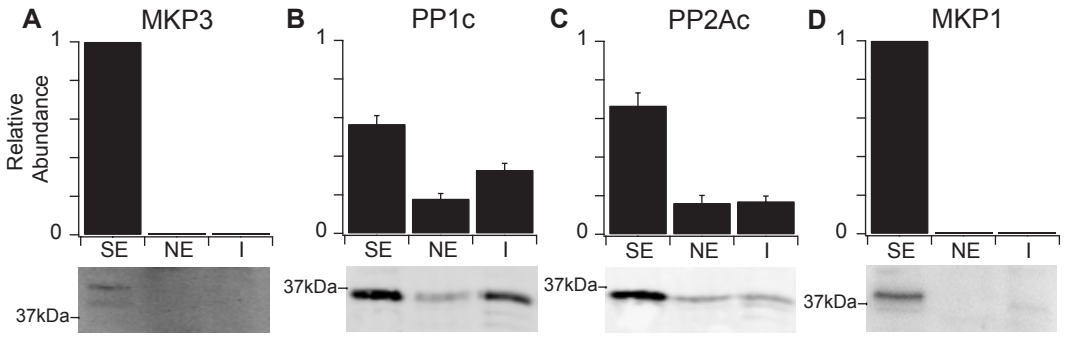

Figure 4. Replicated fractionation of endogenous phosphatases in AC16-CAR cells. Immunoblot comparison of saponin extracts (SE), NP40 extracts (NE) and insoluble protein extracts (I) of endogenous phosphatases MKP3 (*A*), PP1 (catalytic subunit, PP1c) (*B*), PP2A (catalytic subunit, PP2Ac) (*C*), and inducible phosphatase MKP1 (*D*). MKP1 extracts were collected from cells stimulated with 100 ng/mL of EGF for 1 hour. Equal volumes of the SE, NE, and I fractions were loaded for each sample. Densitometry of *n = 3* extraction replicates are shown above a representative immunoblot.

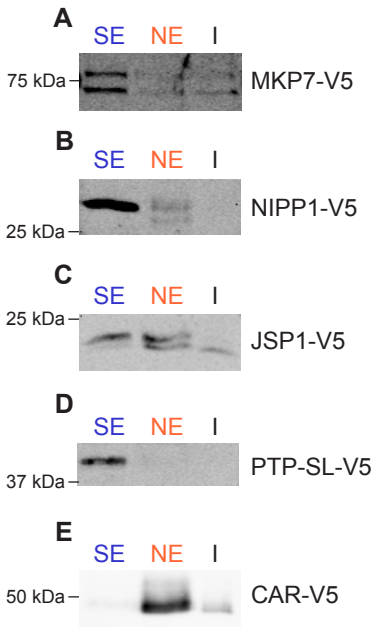

Figure 5. Fractionation of V5-tagged subcellular proteins in AC16-CAR cells.
A-E, Immunoblot comparison of saponin extracts (SE), NP40 extracts (NE) and insoluble protein extracts (I) of V5-tagged MKP7 (*A*), NIPP1 (*B*), JSP1 (*C*), PTP-SL (*D*) and CAR (*E*) from AC16-CAR cells. Equal volumes of the SE, NE, and I fractions were loaded for each sample.

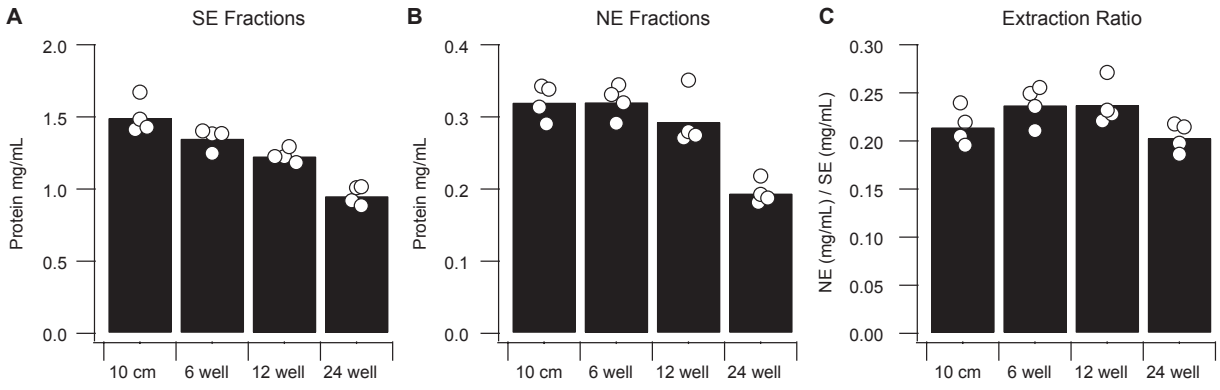

Figure 6. Subcellular protein extraction is reproducible and scalable across various culture formats.

A-C, o-phthalaldehyde-based protein quantification of SE (*A*) and NE (*B*) fractions from plates of different sizes. HeLa cells were seeded at ~50,000 cells/cm^2 for 24 hours before lysis. The extraction ratio (*C*) was calculated as the NE concentration divided by its paired SE concentration. Data are shown from n = 4 biological replicates and are representative of four independent extractions.

Multiplex Quantification of Subcellular Protein Phosphatase Activity

To capture a range of endogenous protein phosphatase activities, we generated six recombinant phosphosubstrates, which are compartmentalized in different subcellular locales and regulated by various stimuli (Figure 1). Phosphorylated MAPKs were previously produced using mutated, constitutively active dual-specificity kinases in vitro with their cognate MAPK substrate: MEK1-DD with ERK2, MKK4-EE and MKK7-EE with JNK1, and MKK6-EE with p38α (29). The efficiency of phosphorylated p38α (phospho-p38α) generation was increased considerably by coexpressing the constitutively active MKK6-EE in bacteria together with GST-tagged p38α. We built upon the success of in vivo p38α phosphorylation and produced phosphorylated MK2 (phospho-MK2) by triple coexpression of MKK6-EE, p38α, and GST-tagged MK2 in bacteria. To expand beyond phosphosubstrates that were themselves kinases, we purified two transcription factors, CREB and STAT1. Like ERK2 and JNK1, CREB and STAT1 were sufficiently phosphorylated in vitro: CREB with phospho-MK2 (described above) and STAT1 with a recombinant JAK1 fragment purified commercially (see Experimental Procedures). Using quantitative immunoblotting (56), we found that the phospho-stoichiometry of all substrates was well below that observed in stimulated cells (Table I), excluding the possibility of off-target dephosphorylation arising from excess phosphosubstrate. For each target, we identified adsorption conditions and phosphospecific antibody titers that yielded an extended linear dynamic range of the ELISA endpoint (Figure 7, arrows). These conditions provided a starting point for each protein phosphatase assay, where loss of phosphoryl groups on the microtiter well caused a proportional loss of ELISA signal.

The expanded panel of phosphosubstrates presented new challenges in measuring protein phosphatase activity. In SE fractions prepared with earlier versions of extraction buffers (29), we found that the phospho-ELISA endpoint increased rather than decreased for substrates such as CREB, suggesting that uninhibited kinase activity was overwhelming phosphatase activity (Figure 8*A*, columns 1 and 2). This phenomenon was not observed in NE fractions, which as a second-step extraction would

contain much lower concentrations of residual ATP (Figure 8*A*, columns 5 and 6, Figure 9*A*-*B*). We depleted ATP from the SE fractions by adding recombinant hexokinase together with its substrate glucose in the extraction buffer. To irreversibly deactivate serine proteases that copurify with hexokinase (76) and destroy phosphosubstrates (Figure 9*C*), we further supplemented the concentrated hexokinase stock solution with PMSF. The modified extraction buffer completely depleted residual ATP and resulted in substantially enhanced protein phosphatase activity measurements (Fig 8A, columns 3 and 4, Figure 9A). Therefore, depletion of endogenous ATP from extracts is critical for widespread measurements of protein phosphatase activity.

We encountered a separate challenge with activity measurements in NE fractions. Efficient extraction of nuclear and transmembrane proteins requires NP40 and NaCl; however, these reagents inhibit protein-protein interactions important for substrate recognition by protein phosphatases. Indeed, extracts in pure NE buffer yielded small and variable decreases in phospho-ELISA signal (Figure 8*B,* columns 1 and 3). After converting absorbance to phosphatase activity (see Experimental Procedures), non-diluted extracts yielded an unacceptable technical CV of 20%. We found that tenfold dilution of NP40 to 0.1% (w/v) and NaCl to 15 mM increased the measured protein phosphatase activity by more than twofold and reduced the technical CV to 3% (Figure 8*B*, columns 3 and 4). For assays requiring more concentrated NE fractions in a given culture format (Figure 6), protein phosphatase activity could be reliably measured with up to 0.3% (w/v) NP40 and 45 mM NaCl, allowing flexibility to adapt measurements to specific experimental settings.

Before quantifying protein phosphatase activity, we altered the temperature and duration of phosphatase reactions to maximize signal (decrease in phospho-ELISA endpoint) while minimizing technical noise relative to extract-free phosphatase blank wells. We sought conditions where the CV was consistently less than 20% when the extracted phosphatases reduced the phospho-ELISA signal by at least 30%. In vitro dephosphorylation kinetics were linear during the assays (Figure 10), ensuring that the extracted phosphatases preserved their activity and did not deplete the available phosphosubstrate on the plate. We calibrated the dynamic range of each assay by measuring protein

phosphatase activity in serially diluted SE or NE fractions that maintain the concentration of critical buffer constituents (hexokinase, reducing agents, etc.). SE and NE protein phosphatase activities increased hyperbolically with extract concentration, as expected, and the optimal dynamic range across the panel was well below 50,000 cells (corresponding to ~20 μg SE fraction and ~9 μg NE fraction) (Figure 11*A*–*L*). This sensitivity and overall performance is comparable to quantitative immunoblotting of protein abundance from total cellular extracts (56). NE phosphatase activity assays for MK2 and CREB phosphatases required more extract, which was achieved by diluting to 0.3% (w/v) NP40 and 45 mM NaCl (see above). The reduced sensitivity toward phosphorylated Ser/Thr substrates is consistent with the low relative abundances of PP1 and PP2A holoenzymes observed in the NE fraction (Figure 2*C*, Figure 4*B*&*C*). The aggregate sensitivity of the measurement platform readily enables six-plex subcellular activity profiling of extracts from one well of a 12-well plate.

We evaluated protein phosphatase specificity of the activity assays by using small-molecule inhibitors. With the pan-phosphatase inhibitor sodium pyrophosphate (NaPP) (77, 78), all activity measurements were potently inhibited as expected (Figure 12*A*–*F*). The tyrosine dephosphorylation of STAT1 was also strongly reduced by sodium orthovanadate (Na_3VO_4) inhibition of PTPs (79, 80) (Figure 12*A*). Reciprocally, the MK2 and CREB phosphatase assays were blocked by microcystin-LR (MCLR), implicating the substrates as targets of PP1, PP2A, or PP4,5,6 phosphatases (81) (Figure 12*B*–*C*). Moreover, because MCLR does not inhibit acid or alkaline phosphatases (82), these results also exclude contaminating activity from other phosphatases in various cellular subcompartments.

The response of the MAPK phosphatase assays was more complex due to the multiple dephosphorylation reactions involved and the mixed specificity of the antibody detection reagents (20, 83, 84). ERK2 phosphatase measurements in SE and NE fractions were almost entirely MCLR sensitive (Figure 12*D*), probably reflecting the phospho-Thr preference of the ELISA antibody (83) or the low abundance of inducible DUSPs for ERK, relative to PP2A, in resting cells (85, 86). Conversely, JNK1 phosphatases were highly vanadate sensitive (Figure 12*E*); a phospho-Tyr preference for the phospho-JNK antibody has not been reported, but multiple JNK-selective DUSPs reside in both the

cytoplasm and nucleus (5). The observed lack of MCLR sensitivity may stem from the prolyl isomerization of JNK within its pThr-Pro-pTyr activation loop (87), which prevents dephosphorylation by PP2A (88).

Most interesting was the behavior of p38α phosphatases, which were much more vanadate sensitive in the NE fraction (Figure 12*F*, gray) but showed similar susceptibility to MCLR as to vanadate in the SE fraction (Figure 12*F*, black). These data are consistent with negative p38α regulation by PP2A in the cytoplasm (89) and DUSPs in the nucleus (5). Together, our inhibitor results confirm that the assay platform measures all major classes of protein phosphatases in the SE and NE subcellular fractions.

We benchmarked the assay platform by performing a brief time-course experiment in cells stimulated with EGF to induce phosphorylation of ERK and the upregulation of DUSPs (90). In parallel with extracts for phosphatase activity, subcellular samples were prepared for phospho-ERK quantification by supplementing SE and NE buffers with phosphatase inhibitors (see Experimental Procedures). In the SE fraction, we observed a rapid increase in ERK phosphorylation within five minutes that remained elevated for up to two hours (Figure 13*A*–*B*). ERK2 phosphatase activity also increased in the SE fraction, likely blunting the peak phosphorylation observed, but the increase was transient and could not revert phospho-ERK abundance to pre-stimulus levels (Figure 13*C*). Similar transients were observed for p38α and JNK1 phosphatases in the SE fraction (Figure 14*A*–*B*), suggesting activity by a shared set of DUSPs. In contrast, MK2 and CREB phosphatase activities in the SE fraction were slowly reduced after EGF stimulation (Figure 14*C*–*D*), and STAT1 phosphatase activity was rapidly elevated and sustained, perhaps in response to STAT1 phosphorylation induced by EGF (91, 92) (Figure 14*E*). The qualitatively different phosphatase dynamics in the SE fraction provide a further validation of substrate specificity afforded by the assay.

A very different time course of phospho-ERK abundance was observed in the NE fraction. ERK phosphorylation was slower, peaking at 30 minutes concomitant with maximum total ERK shuttled into

the nucleus (Figure 13*D*–*E*). Importantly, phospho-ERK in the NE fraction reverted to pre-stimulus levels within two hours, suggesting that negative regulation in this subcompartment was more persistent than in the SE fraction. Corroborating the phospho-ERK dynamics, we found that ERK2 phosphatase activity in the NE fraction was increased and sustained from 30–120 minutes after EGF stimulation. Moreover, this trajectory was unique among MAPKs, as p38α phosphatase activity in the NE fraction was transiently increased and JNK1 phosphatase activity was slightly decreased (Figure 14*F*–*G*). Among other phosphosubstrates, MK2 and CREB phosphatases were largely unaltered in the NE fraction, while STAT1 phosphatases were slowly and transiently activated (Figure 14*H*–*J*). Overall, the measured subcellular ERK2 phosphatase activities reconcile the observed phospho-ERK dynamics, while the broader panel of phosphosubstrates in the assay reinforces the more-widespread alterations caused by EGF stimulation.

Table I. Phospho-stoichiometry of recombinant phosphosubstrates

Substrate	Phosphosite	Recombinant[a]	In vivo[a] (stimulation[b])
ERK2	Thr^{202}/Tyr^{204}	0.10	1.9 (EGF)
p38α	Thr^{180}/Tyr^{182}	0.040	3.5 (TNF)
JNK1	Thr^{183}/Tyr^{185}	0.046	3.1 (TNF)
MK2	Thr^{334}	0.69	4.8 (TNF)
CREB	Ser^{133}	0.033	2.2 (TNF)
STAT1	Tyr^{709}	6.4	36 (IFNβ)

[a] Values are reported relative to unstimulated AC16-CAR cells.
[b] EGF, 100 ng/ml EGF for 5 min; TNF, 20 ng/ml TNF for 15 min; IFNβ, 50 ng/ml IFNβ for 30 min.

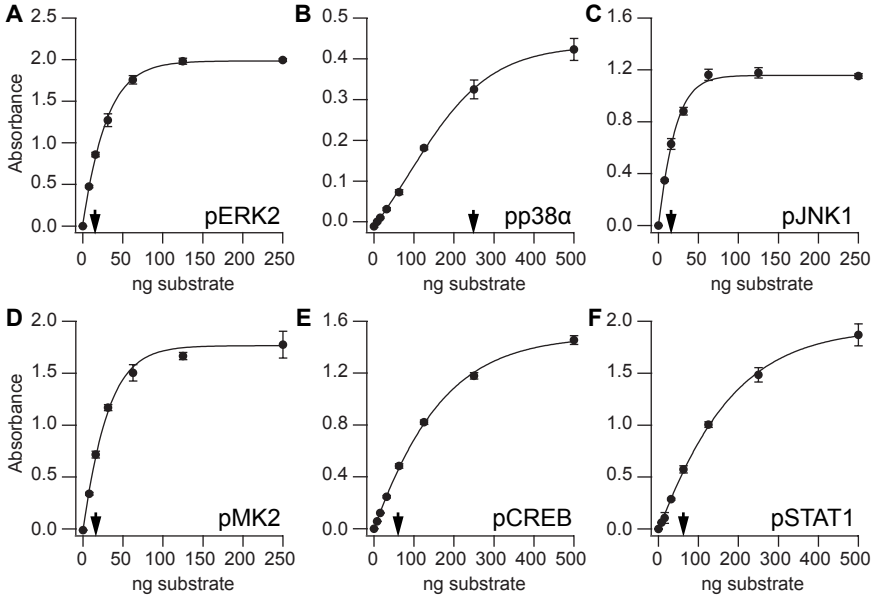

Figure 7. Phospho-ELISA quantification of adsorbed recombinant substrates.
A-*F*, Phosphoproteins were serially diluted (two-fold) and adsorbed overnight onto 96-well plates. Phosphospecific antibody binding for pERK2 (*A*), pp38α (*B*), pJNK1 (*C*), pMK2 (*D*), pCREB (*E*), and pSTAT1 (*F*) was detected by ELISA. The amount of substrate added for each phosphatase assay is indicated by a black arrow (see Experimental Procedures). Data are shown as the mean ± standard deviation of $n = 4$ assay replicates.

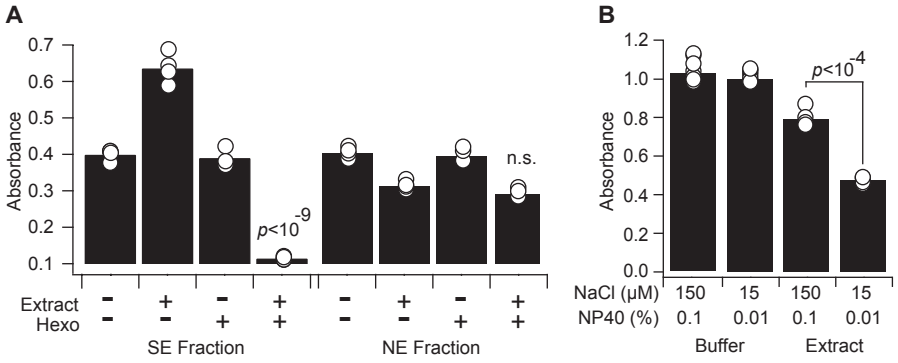

Figure 8. ATP depletion and salt-detergent dilution are required for reliable subcellular phosphatase activity measurements.
A, Adsorbed recombinant phospho-CREB was incubated with (+) or without (–) SE or NE fractions (50,000 cell equivalents) and with (+) or without (–) exogenous hexokinase (Hexo) to deplete intracellular ATP. CREB phosphorylation was measured by phospho-ELISA after incubation for one hour at 30ºC. Interaction between hexokinase and lysate was assessed statistically by two-way ANOVA. Data are shown as the mean of $n = 4$ independent biological extracts. *B*, Adsorbed recombinant phospho-p38α was incubated with NE fraction (8,500 cell equivalents) in NE buffer containing the indicated final concentrations of NaCl and NP40. p38α phosphorylation was measured by phospho-ELISA after incubation for one hour at 30ºC. Data are shown as the mean of $n = 8$ (buffer) or 4 (extract) assay replicates. Difference in means was assessed by two-tailed Student's *t* test.

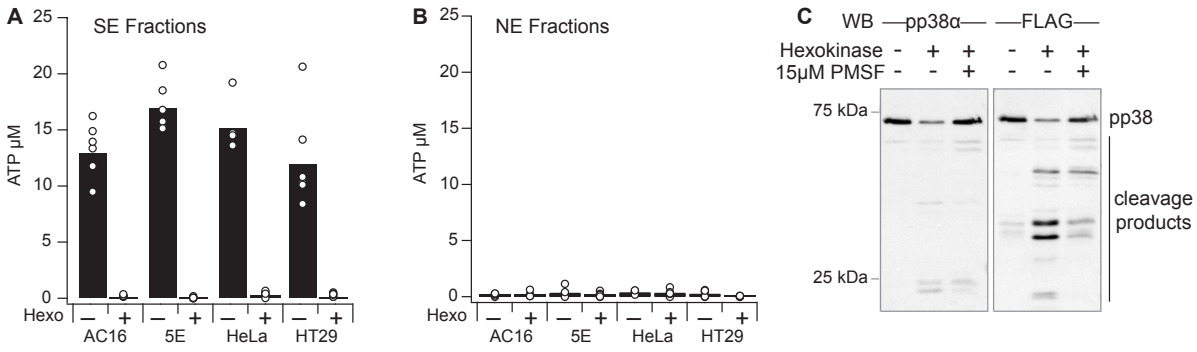

Figure 9. Hexokinase supplementation depletes intracellular ATP.
A-B, ATP quantification in SE (*A*) and NE (*B*) fractions from the indicated human cell lines with (+) or without (-) exogenous hexokinase (Hexo) in the extraction buffer. Data are shown as the mean of $n = 6$ independent extractions per cell line per condition. *C*, Recombinant pp38α was incubated in SE buffer with or without hexokinase and 15 μM PMSF to inhibit contaminating protease activity as indicated. Samples were immunoblotted for pp38 or total FLAG protein.

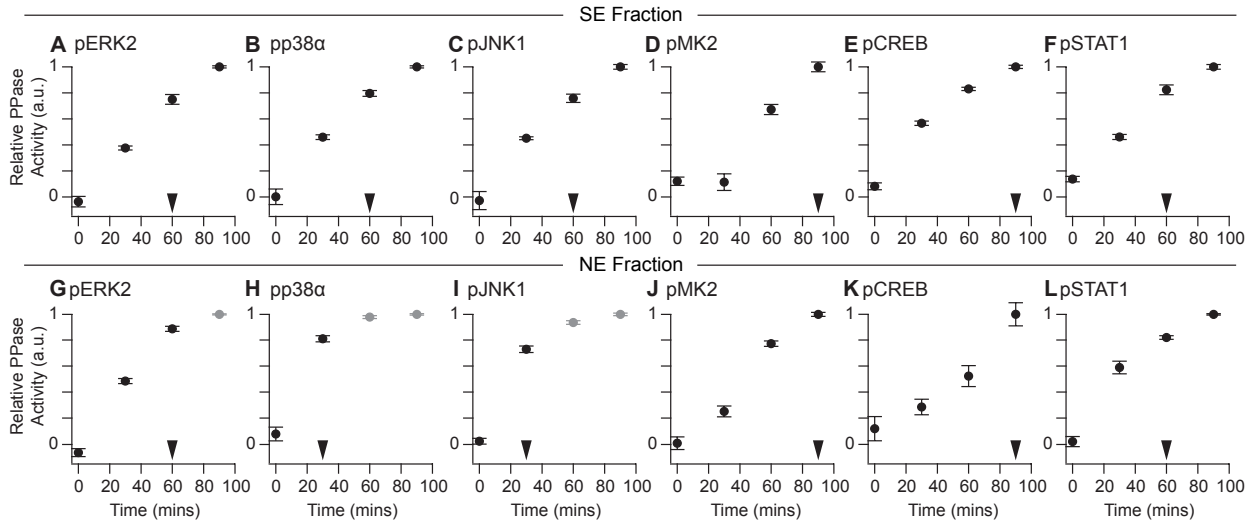

Figure 10. Reaction kinetics are linear during each phosphatase assay.
A-L, Phosphatase activity of AC16-CAR cells was measured in SE (*A-F*) and NE (*G-L*) fractions at the indicated reaction times. NE fractions used for pMK2 (*J*) and pCREB (*K*) were collected from cells stimulated with TNF for 30 minutes. Black arrowheads indicate the optimal phosphatase reaction time after which the kinetics saturate (gray markers). Data are shown as the mean ± standard error for $n = 4$ assay replicates.

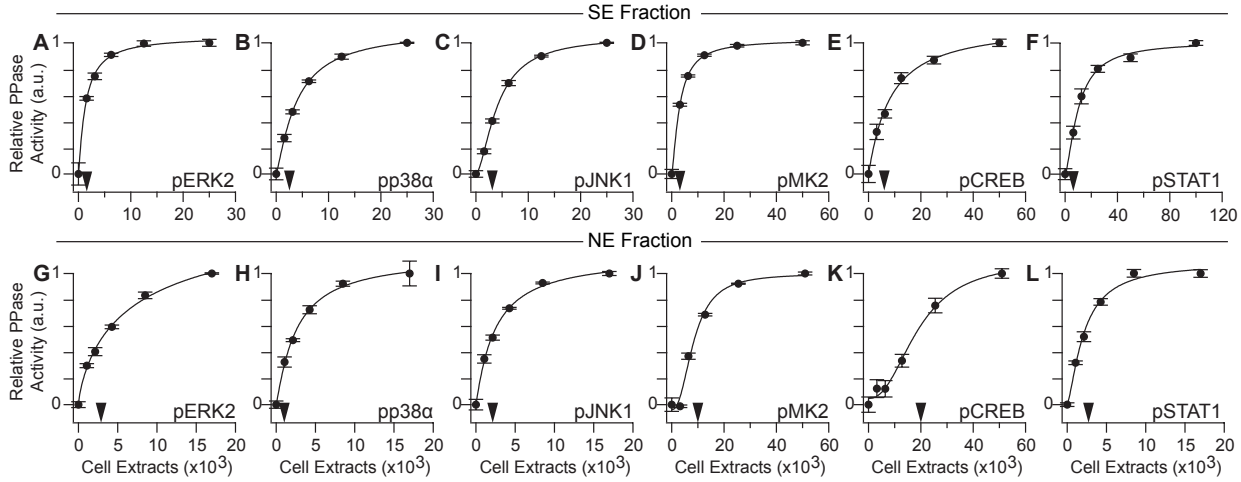

Figure 11. Sensitive detection and quantification of substrate-specific subcellular phosphatase activities.

A-*F*, SE phosphatase assays were performed with twofold serially diluted AC16-CAR extracts starting at 25,000 (*A*-*C*), 50,000 (*D*-*E*), or 100,000 (*F*) cell equivalents. *G*-*L*, NE phosphatase assays were performed with twofold serially diluted extracts starting at 17,000 (*G*-*I*, *K*) or 51,000 (*J*, *L*) cell equivalents. NE fractions for phospho-MK2 (*J*) and phospho-CREB (*K*) were collected from cells stimulated with TNF for 30 minutes. Black arrows denote the optimized extract concentration for each assay. Phosphatase activity data were regressed against cell input with a four-parameter logistic regression curve. Data are shown as the mean ± standard error of $n = 4$ assay replicates.

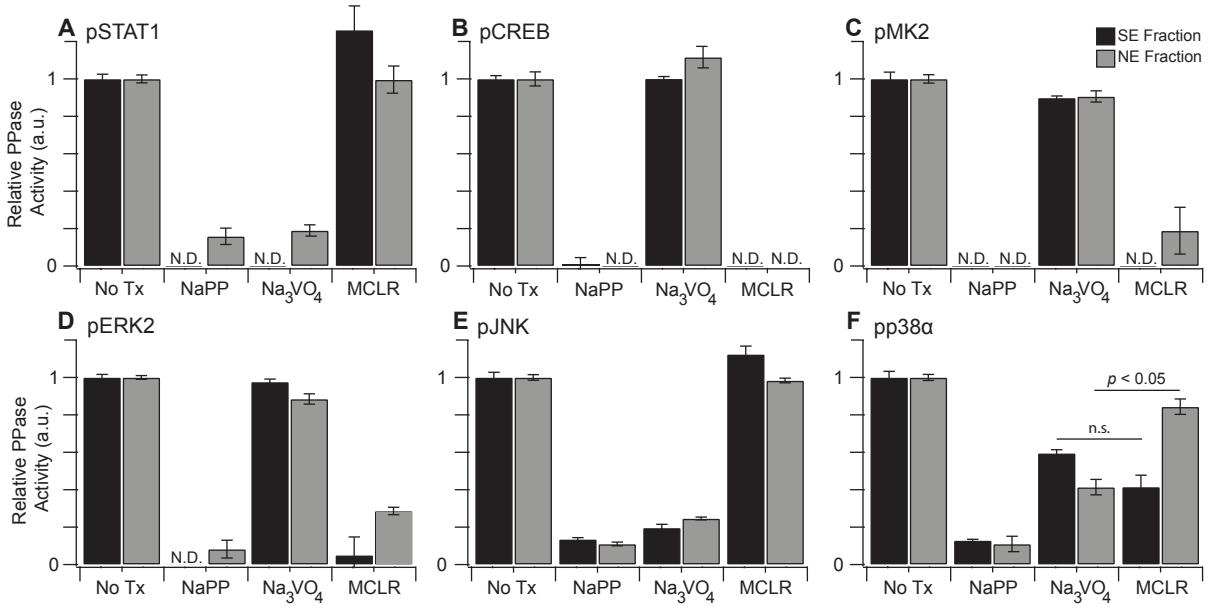

Figure 12. Subcellular phosphatase assays are sensitive to specific classes of phosphatase inhibition.

A-F, Phosphosubstrates were incubated with AC16-CAR SE (black bars) or NE (gray bars) fractions and the pan phosphatase inhibitor NaPP (10 mM), the Tyr phosphatase inhibitor Na_3VO_4 (200 μM), the Ser/Thr phosphatase inhibitor microcystin-LR (MCLR, 1 μg/mL), or control (NoTx). NE fractions used for phospho-CREB (*B*, gray bars) and phospho-MK2 (*C*, gray bars) were collected from cells stimulated with TNF for 30 minutes. Cellular equivalents for each assay are listed in supplemental Table S2. Data are shown as the mean ± standard error of n = 8 (NoTx) or 4 (NaPP, Na_3VO_4, MCLR) assay replicates. N.D., not detectable above baseline. Fraction-specific sensitivity differences were assessed by two-tailed Student's t test with Bonferroni correction.

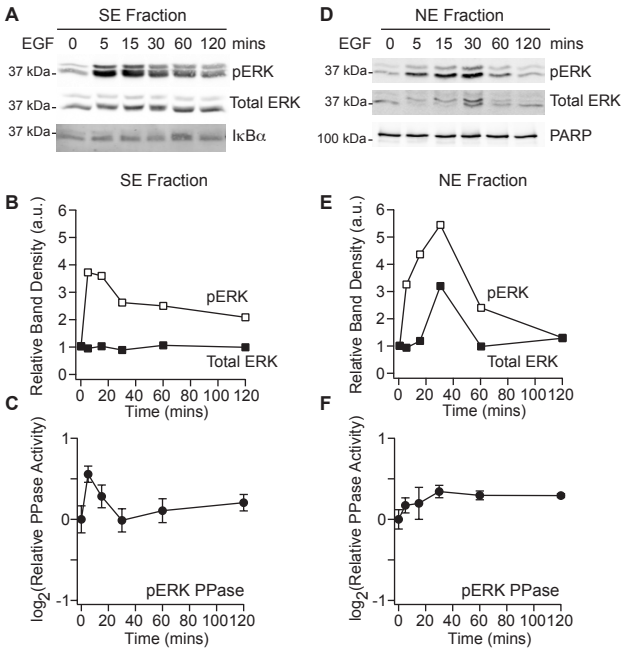

Figure 13. EGF stimulates subcellular ERK phosphorylation and ERK phosphatases.
A-B, Immunoblots for phospho-ERK and total ERK in the SE fraction (*A*) were quantified by densitometry (*B*) with IκBα used to confirm equal loading. *C*, ERK2 phosphatase activity quantified in the SE fraction. *D-E*, Immunoblots for phospho-ERK and total ERK in the NE fraction (*D*) were quantified by densitometry (*E*) with PARP used to confirm equal loading. *F*, ERK2 phosphatase activity quantified in the NE fraction. Phosphatase activities are shown as the mean ± standard error of $n = 4$ biological replicates. Cells were stimulated with 100 ng/mL of EGF for the indicated times.

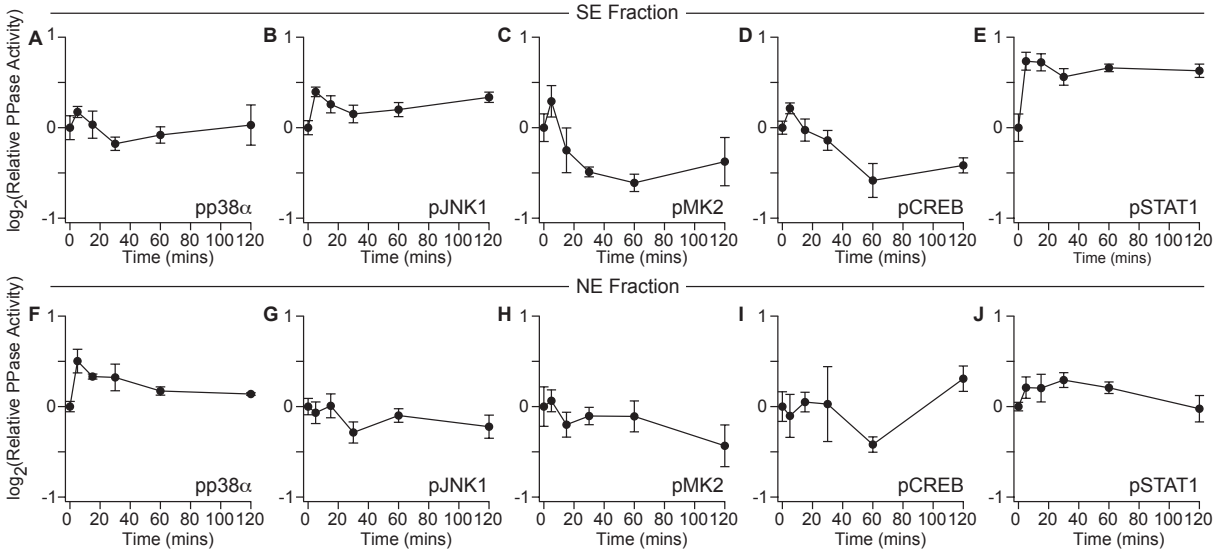

Figure 14. Subcellular phosphatase activity time courses in response to EGF stimulation. *A*-*J*, Phosphatase activities in SE (*A*-*E*) and NE (*F*-*J*) fractions are shown for all substrates except pERK. Data are shown as the mean ± standard error of $n = 4$ biological replicates, except for the pp38α NE fraction consisting of $n = 3$ biological replicates. AC16-CAR cells were stimulated with 100 ng/mL EGF for the indicated times.

Viral and Antiviral Regulation of Protein Phosphatases During Acute Infection of Cardiomyocytes with Coxsackievirus B3

To profile subcellular protein phosphatase dynamics in infectious disease, we investigated the interactions between host-cell antiviral signaling and acute infection by CVB3, which perturbs most of the signaling pathways in the assay panel (Figure 1). Despite its recognized tropism for juvenile cardiomyocytes (93, 94), CVB3 pathogenesis is largely studied in permissive HeLa cells because of the efficiency of viral propagation (40, 95, 96). As an alternative, neonatal mouse HL-1 cells have been used (35, 39), but these cells are atrially derived, and CVB3 infections disproportionately impact the ventricular myocardium (97, 98). A human ventricular cardiomyocyte cell line that is susceptible to CVB3 would be highly desirable for in vitro studies of host-pathogen interactions.

We tackled this challenge by starting with AC16 cells, a clonal human line derived by fusing adult ventricular cardiomyocytes with SV40-transformed fibroblasts (53). Although lacking the typical sarcomeric organization of the myocardium, AC16 cells express several markers of immature cardiomyocytes, including cardiac-specific transcription factors and contractile proteins. SV40 small t antigen alters PP2A function as an unavoidable facet of the line (99), but AC16 cells nonetheless have detectable MCLR-sensitive phosphatase activity at baseline (Figure 12*B*–*D*, 12*F*). Given that AC16 cells originate from adult tissue and expression of the CVB3-obligate receptor CAR declines with age (100), we reconstituted CAR by lentiviral transduction and stable selection to generate AC16-CAR cells (see Experimental Procedures). Compared to the parental AC16 line, AC16-CAR cells were much more supportive of intracellular viral protein synthesis upon CVB3 infection, as indicated by expression of the viral capsid protein VP1 (Figure 15*A*). We also detected cleavage of eIF4G, a recognized target of the active enteroviral protease 2A (101). Accordingly, CVB3 infection was substantially more toxic to the AC16-CAR line. By fluorescence microscopy, we observed cells with increased caspase-3 cleavage as well as others with compromised membrane integrity (Figure 15*B*), indicating concurrent apoptosis and necrosis within the culture (39). Cardiomyocyte apoptosis has been shown to be correlated with CVB3 viral titer (102), and we found that viral titers increased 1000-fold in conditioned media from infected

AC16-CAR cells (Figure 15*C*–*D*). Therefore, with the restoration of CAR, AC16 cells support all stages of the viral life cycle required to amplify an acute infection.

We sought to use AC16-CAR cells together with the subcellular phosphatase assay to profile activity changes during CVB3 infection and the associated interferon response. Type I interferons (IFNα, IFNβ) are potently induced by double-stranded RNA (dsRNA) that accompanies viral replication, but CVB3 counteracts the type I response by cleaving sensors and transducers of dsRNA (103). Type II interferon (IFNγ) signaling is initiated by the paracrine action of natural killer cells, which become activated upon CVB3 infection (44). Co-treatment of cells with IFNβ and IFNγ synergistically inhibits CVB3 replication (104), and IFNβ treatment alone has shown some success in clearing persistent CVB3 infections (98). Phosphatases are rare among interferon-stimulated genes (105), but some viruses directly perturb interferon action by upregulating phosphatase activity (106). Whether more-distant crosstalk occurs between phosphatases modulated by interferons and CVB3 has not been examined.

The throughput of the assay enabled a highly replicated (n = 9), fully crossed design of three factors: CVB3 (MOI = 10), IFNβ (30 ng/ml), and IFNγ (50 U/ml). Samples receiving CVB3 were infected for three hours before stimulation with IFNβ, IFNγ, or both, followed by on-plate fractionation and phosphatase-activity profiling of the resulting extracts. Some assays showed skewed or leptokurtic error distributions across biological replicates, requiring the use of nonparametric methods for statistical inference in these instances (see Experimental Procedures). Without antiviral cytokines, we did not detect significant differences in phosphatase activity caused by CVB3 infection alone after correcting for multiple-hypothesis testing (Figure 16*A*). Therefore, day-to-day and plate-to-plate variation was accounted for by normalizing data to the median activity of no-cytokine samples in each group (see Experimental Procedures). The full-factorial design of the experiment allowed us to test for main effects of CVB3, IFNβ, and IFNγ, as well as nonlinear interactions between factors that would indicate synergistic or antagonistic regulation.

Overall, we observed various single-factor perturbations consistent with the literature (Figure 16*B*). For example, IFNβ independently suppressed ERK2, p38α, and MK2 phosphatase activities in the SE fraction (Figure 16*C*–*E*, $p < 0.01$). ERK activity is critical for the type I interferon response (107). Also, the p38–MK2 pathway stabilizes mRNAs with AU-rich elements (108, 109), a characteristic of many interferon-response genes (105) (Table II). Reduced phosphatase activity toward these targets may collectively prolong the duration of the type I interferon response. Notably, we did not observe IFNβ-stimulated decreases in all DUSP or Ser/Thr phosphatase targets (Figure 16*B*, JNK1 and CREB), reinforcing the specificity of the assay panel.

IFNβ suppression of p38α phosphatase activity was also observed in NE fractions (Figure 16*C*, $p < 0.001$), but there were multiple instances of changes specific to one cellular subcompartment. In contrast to IFNβ, we found that IFNγ upregulated p38 phosphatase activity only in the NE fraction ($p < 0.01$). A similar trend was observed for JNK1 phosphatase in the SE fraction (Figure 16*F*), although the IFNγ effect did not retain statistical significance after correction for multiple-hypothesis testing at a false-discovery rate of 10%. Long-term (3+ hours) stimulation of macrophages with IFNγ upregulates MKP5 and MKP7 (110), which dephosphorylate JNK–p38 and endogenously localize to the cytoplasm and nucleus (5). Our findings raise the possibility that these induced DUSPs exhibit different substrate preferences depending on their localization.

Despite median normalization, specific subcellular perturbations were also detected in CVB3-infected cells: ERK2 phosphatase activity in the SE fraction was increased overall (Figure 16*D*, $p < 0.01$) along with the activity of JNK1 phosphatases in the NE fraction (Figure 16*F*, $p < 0.001$). ERK2 phosphatase activity likely reflected the compensatory upregulation of cytoplasmic DUSPs, such as MKP3, that could be induced by CVB3 activation of the ERK pathway (37). The NE-associated JNK1 phosphatase result was more intriguing given conflicting reports involving the role of JNK activation in CVB3 pathogenesis (38, 111). We therefore pursued follow-on experiments to dissect mechanistically the role of CVB3-associated JNK1 phosphatase activity in the NE fraction.

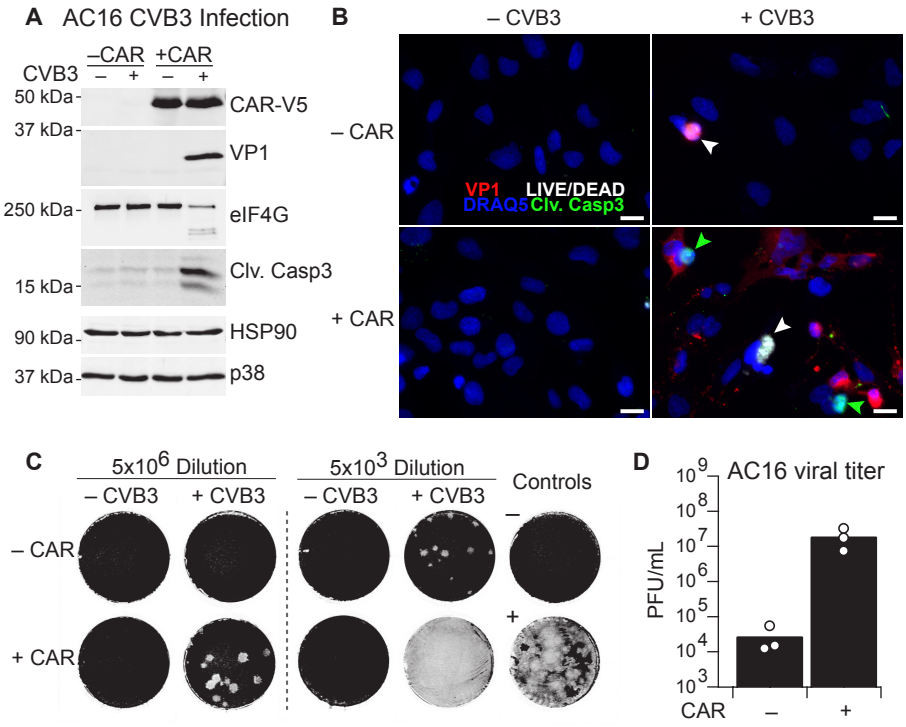

Figure 15. Modeling acute CVB3 Infection through engineered AC16-CAR cells.
A, Immunoblot of infected and non-infected AC16 cells for V5 epitope-tagged CAR (CAR-V5), viral capsid protein VP1, viral protease target eIF4G, and cleaved caspase-3 (Clv. Casp3), with HSP90 and p38 used as loading controls. *B*, Immunofluorescence of infected versus non-infected parental and CAR-expressing AC16 cells stained for VP1 (red), Clv. Casp3 (green), LIVE/DEAD stain (white) (39), and nuclei (blue). Green arrowheads indicate apoptotic cells, and white arrowheads indicate necrotic cells. Scale bar is 20 μm. *C*, Plaque assay of two dilutions of conditioned medium from AC16 cells with or without CAR expression and with or without CVB3 infection. The negative control (unconditioned medium) and positive control (2000 plaque forming units [PFU] of CVB3) are shown on the right. Viral plaques appear white and indicate the presence of single infectious virions, which propagate to surrounding cells. *D*, Quantification of viral PFUs from *n* = 3 independent CVB3 infections and plaque assays. Cells were infected with sham or CVB3 at MOI = 10 for 24 hours.

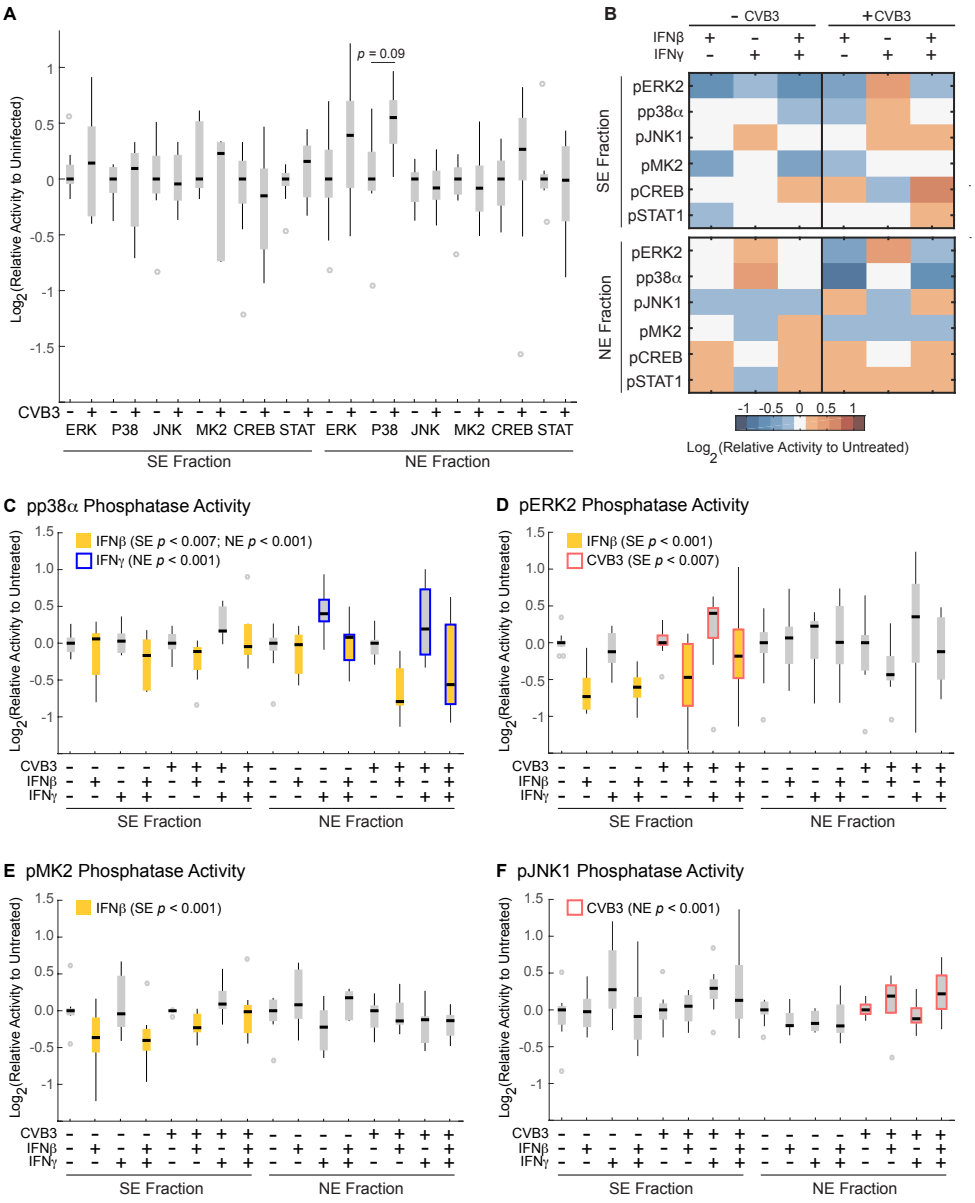

Figure 16. Subcellular phosphatase profiling of CVB3 infection and interferon signaling in AC16-CAR cells.

A, Subcellular phosphatase activities are comparable after infection with CVB3 (MOI = 10) for seven hours. No differences were statistically significant after correcting for multiple-hypothesis testing (see Experimental Procedures). *B*, Heat map of median phosphatase activity changes in AC16-CAR cells treated with or without CVB3 (MOI = 10) for three hours followed by treatment with IFNβ (30 ng/mL), IFNγ (50 U/mL), or both for four hours. Cellular equivalents for each assay are listed in supplemental Table S3. *C-F,* Box-and-whisker plots of replicated data summarized in (*B*). Significant main effects at a 10% false-discovery rate (see Experimental Procedures) are highlighted for IFNβ (solid yellow), IFNγ (blue box), and CVB3 (red box). For (*A*) and (*C-F*), black bars show $\log_2$-transformed median activity levels of $n = 9$ independent biological replicates. Gray boxes indicate interquartile range. Black whiskers denote values that fall within 1.5 times the interquartile range. Gray dots are outliers beyond 1.5 times the interquartile range.

Table II. Percentage of IFN target genes with AU-rich elements (AREs) in the human, mouse, and rat genomes.

Species	AREs	p =
Human	22%	2×10^{-9}
Mouse	17%	9×10^{-14}
Rat	7.6%	4×10^{-5}

The list of interferon-stimulated genes from (2) was assessed for AREs using ARED Organism (3). Enrichment *p* values were determined by binomial test

Nuclear JNK1 Phosphatases Impede CVB3 Pathogenesis

Given the considerable vanadate sensitivity of JNK1 phosphatases in the NE fraction (Figure 12*E*), we first sought to identify nuclear DUSPs that contributed to the activity measured by the assay. We cloned inducible shRNAs (Figure 17) for four JNK-targeting DUSPs and transduced AC16-CAR cells to assess their individual contributions toward JNK1 phosphatase activity in the NE fraction. Significant changes were not observed with shMKP7 or shDUSP19 perturbations, but knockdown of MKP1 and MKP5 reduced JNK1 phosphatase activity in the NE fraction by ~50% and ~30% respectively (Figure 18). These results implicate MKP1 and MKP5 as the predominant JNK1 phosphatases in the NE fraction of AC16-CAR cells.

Next, it was important to clarify the role of JNK pathway activity in CVB3 pathogenesis. Prior CVB3 studies involving the JNK pathway relied on a first-generation inhibitor that is now known to inhibit many other kinases (38, 111, 112). We therefore turned to JNK-IN-8 (IN8), a newer covalent JNK inhibitor that is much more selective (113). Rather than block the JNK pathway constitutively, we sought to exploit the covalent nature of IN8 and achieve a slow reactivation of JNK by washout during infection. Three-hour preincubation of cells with IN8 strongly reduced cJun phosphorylation—a surrogate of JNK activity—but phosphorylation was nearly restored to control levels after 20 hours of washout (Figure 19*A*). By shifting the initial baseline, IN8 washout achieves a fold-change activation of the JNK pathway that can be overlaid on viral and antiviral signaling (Figure 19*B*) (114-116).

As a single factor, CVB3 increased JNK1 phosphatase activity in the NE fraction (Figure 16*F*), but there was also a suggestive synergy with IFNβ (interaction $p < 0.05$), prompting us to perform the IN8 washout experiments in CVB3-infected cells ± IFNβ. The interferon response initiated by IFNβ strongly suppressed translation of VP1 during CVB3 expression, as expected, but we found that VP1 abundance doubled when the JNK pathway was activated by IN8 washout (Figure 19*C*–*D*). These results suggest that CVB3- and IFNβ-induced activation of JNK phosphatases may contribute to the host antiviral response.

The IN8 washout experiment generally implicates the JNK pathway in CVB3 pathogenesis but cannot assign a specific role for nuclear-localized activity. To do so, we engineered inducible MKK4-EE and MKK7-EE alleles harboring a potent nuclear localization sequence (NLS) that should restrict JNK activation to the nucleus. By immunofluorescence, we confirmed the localization of MKK4-EE-NLS and MKK7-EE-NLS and observed an increased frequency of cells with elevated cJun phosphorylation compared to EGFP-NLS controls (Figure 19E). Timed induction of JNK activators was reliable under resting conditions but became highly variable during CVB3 infection and IFNβ stimulation due to the shutdown of protein translation during the host-cell interferon response. We exploited this variability to ask whether the amount of induced MKK4/7-EE-NLS corresponded to a proportional increase in VP1 abundance for the same biological replicate. Indeed, VP1 expression was significantly correlated with MKK4/7-EE-NLS but not EGFP-NLS controls, indicating that nuclear JNK activation promotes viral propagation in infected host cells. These follow-on experiments together provide a rationale and molecular basis for the CVB3- and IFNβ-stimulated JNK1 phosphatase activity measured by the assay in the NE fraction.

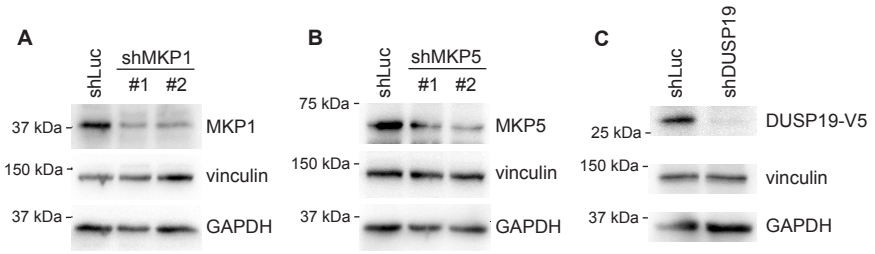

Figure 17. Knockdown of pJNK targeting DUSPs with shRNA.
A, AC16-CAR cells were transduced twice with lentivirus encoding the indicated hairpin and induced for 24 hours then stimulated with 100 ng/mL EGF for 1 hour before whole cell lysis. *B-C,* Transient co-lipofection of induced shMKP5 or shDUSP19 hairpins with V5-tagged MKP5 (*B*) and DUSP19 (*C*) in 293T cells. Knockdown was assessed in whole cell extracts after 48 hours. shMKP7 hairpins were previously described (1).

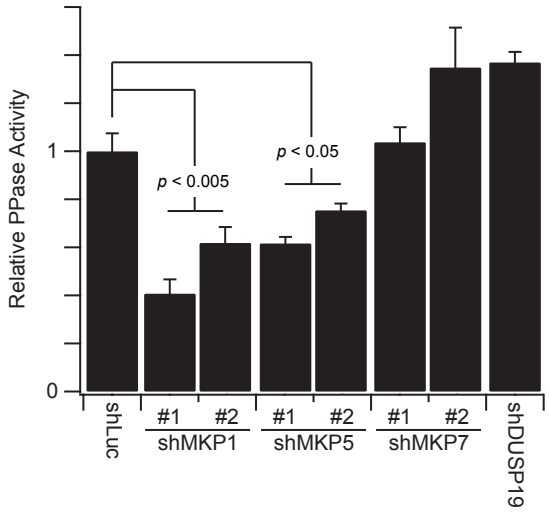

Figure 18. JNK phosphatase activity in the NE fraction is reduced upon knockdown of MKP1 and MKP5.
AC16-CAR cells stably expressing inducible shRNA constructs encoding the designated hairpin were induced for 72 hours with doxycycline before subcellular fractions were collected. JNK1 phosphatase activity in the NE fraction is shown as the mean ± standard error of $n = 3$ biological replicates. Significant differences from the control shLuc hairpin were assessed by Student's *t* test with Bonferroni correction and Fisher's method of combined probability where applicable.

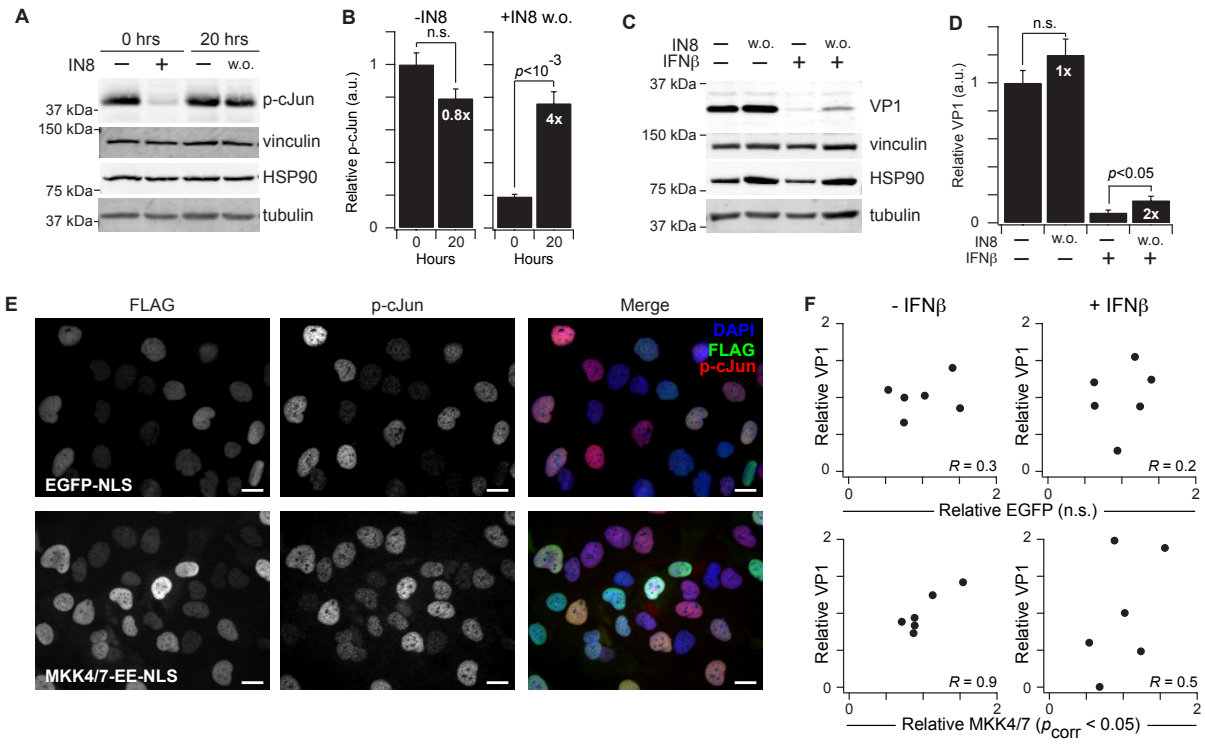

Figure 19. Nuclear JNK1 activity promotes CVB3 protein synthesis in infected AC16-CAR cells. *A-B,* Immunoblots for p-cJun before and after JNK-IN-8 (IN8) washout (w.o.) (*A*) were quantified by densitometry (*B*) with vinculin, HSP90, and tubulin used to confirm equal loading. Fold change in p-cJun relative to the corresponding pre-washout condition is shown in white. *C-D*, Immunoblots for VP1 with or without IN8 washout, IFNβ treatment, or both in CVB3-infected cells (*C*) were quantified by densitometry (*D*) with vinculin, HSP90, and tubulin used to confirm equal loading. Fold change in VP1 relative to the corresponding pre-washout condition is shown in white. *E,* Immunofluorescence of EGFP-NLS or MKK4/7-EE-NLS and p-cJun in AC16-CAR cells. Scale bar is 20 μm. *F,* Correlation plots between relative FLAG and VP1 abundance in infected AC16-CAR cells overexpressing EGFP-NLS (top panels) or MKK4/7-EE-NLS (bottom panels). IN8 data are shown as the mean ± standard error of *n* = 4 biological replicates. Differences in p-cJun (*B*) and VP1 (*D*) abundance were assessed by Student's *t* test. FLAG-VP1 Pearson correlations (*R*) were assessed after Fisher Z transformation and Fisher's method of combined probabilities for each cell line.

2.3. Discussion

This work considerably extends the premise of substrate-directed phosphatase activity profiling (29) by doubling the number of substrates and subcellular compartments accessible with the method. Phosphoprotein-focused mathematical models of cell signaling often separate rate processes that occur in the cytoplasm and nucleus (117-119). Subcellular measurements of protein phosphatase activity will help to parameterize time- and subcompartment-specific deactivation rates, which determine steady-state signaling (6). Furthermore, it should be easier to hone in on detailed mechanisms of phosphosubstrate regulation (29) by focusing on the specific phosphatases localized to where activity changes were measured (5, 22). In this way, systematic experiments performed with high-throughput methods set the stage for more in-depth mechanistic hypotheses (120, 121).

The expanded phosphatase format revealed cellular ATP as an important confounder in the assay. We had noted increased, rather than decreased, substrate phosphorylation in the assay before (29) but discounted it because it was observed only when JNK phosphatases were measured in the presence of vanadate. After ATP depletion, phospho-JNK dephosphorylation is considerably inhibited by vanadate in both NE and SE fractions (Figure 12*E*). Our results corroborate observations in clinical isolates, which illustrated that kinases are as problematic as phosphatases when seeking to accurately capture the cellular phosphoproteome accurately (61). For enzyme-catalyzed depletion of ATP, hexokinase is a useful alternative to apyrase (122) when extracts must be kept at low temperature (123).

Isolation of NE-fractionated protein phosphatases was a tradeoff between extraction efficiency and retention of catalytic activity. Proteins tightly associated with chromatin, including some protein phosphatases (22), likely remain in the nucleus after extraction. However, the conditions required to displace such proteins would undoubtedly interfere with activity in the entire extract. Nuclear MK2 and CREB phosphatase activity measurements were somewhat less sensitive than others in the panel, possibly due to unextracted PP1 isoforms (124). More important than total extraction is the ability to

capture stimulus-dependent changes in phosphatase activity, as observed in response to growth factors, interferons, and viruses.

We found that reconstitution of CAR expression was sufficient to render AC16 cells permissive to CVB3. CAR is not universally rate-limiting for CVB3 infection—A549 lung adenocarcinoma cells express as much CAR as permissive HeLa cells, but their ability to propagate the virus is restricted by deficient expression of the DAF coreceptor (125). CVB3 permissiveness is also dictated by more than cell-surface receptors, with many intracellular factors contributing positively or negatively to infectivity (41). For example, HeLa cells become non-permissive upon overexpression of the mitochondrial antiviral signaling protein MAVS (126). AC16 cells were originally isolated from human ventricular cardiomyocytes of an adult (53), and their initial CVB3 restriction likely stems from the natural decline in CAR expression that occurs with age (100). CAR-supplemented AC16 cells provide an improved CVB3 host, which reflects the natural tropism of the virus.

Our crossed experimental design with CVB3 and antiviral factors uncovered multiple changes in protein phosphatase activity that could contribute to systems analyses of virus-host interactions. By coupling protein phosphatase profiles with matched observations of kinase activity and substrate phosphorylation, related data types could be assessed for concordance (127-129). The substrate-focused phosphatase assays are ideal for such a comparison, with the tradeoff that it is more complicated to identify the specific phosphatase(s) involved. Nevertheless, it is possible to dissect mechanisms as we showed for the elevated JNK1 phosphatase activity observed in the NE fraction of AC16-CAR cells. For interferons and other extracellular ligands, transcriptomic profiles of protein phosphatase subunits could provide clues about induced changes in abundance. The challenge is greater for CVB3-induced perturbations, which are largely mediated by the proteases 2A and 3C or by innate antiviral mechanisms. Many protein phosphatases contain high scoring consensus sequences for enteroviral proteases (130), suggesting that perturbations could be highly multifaceted.

The demonstrated generality of the assay platform opens up additional opportunities to interrogate protein phosphatase activities related to CVB3 infection. In epithelia, viral docking rapidly

activates Abl and Fyn, and CVB3 crosslinking of DAF in lymphocytes triggers phosphorylation of Lck (32-34). These nonreceptor tyrosine kinases readily autophosphorylate in bacteria and in vitro (131, 132), suggesting that such substrates could be prepared in high yield for Abl-, Fyn-, and Lck-focused phosphatase assays. CVB3 infection also mobilizes Ca^{2+} stores (133), and the Ca^{2+}-activated phosphatase calcineurin disinhibits NFAT, a transcription factor whose activation in T cells promotes myocarditis (134). A calcineurin-focused NFAT phosphatase assay would enable a further elaboration of the host-cell signaling networks perturbed by CVB3.

The CVB3 genome engages many intracellular signaling pathways to disrupt host-cell functions (135). Decoding viral mechanisms of action on specific host phosphoproteins will be critical for devising strategies to block or offset these mechanisms during CVB3 infection. Reciprocally, one can envision future virus-inspired interventions for diseases of signaling misregulation such as lung cancer, where high CAR expression is important for tumorigenesis (136) and CVB3 has been shown to be oncolytic (137)

2.4. Experimental procedures

Plasmids — For phosphosubstrate preparation and purification, pGEX-4T-1 3×FLAG-ERK2, pGEX-4T-1 3×FLAG-JNK1, pGEX-4T-1 3×FLAG-p38α, pGEX-4T-1 3×HA-MEK-DD, pGEX-4T-1 3×HA-MKK4-EE, pGEX-4T-1 3×HA-MKK7a1-EE, and pGEX-4T-1 3×HA-MKK6-EE were described previously (29). Human MKK6-EE (Addgene plasmid #13518) (47) was cloned into the BamHI and SalI sites of pCDFDuet-1 (Novagen, Madison, WI) by PCR with the primers gcgcagatctatgtctcagtcgaaaggcaag (forward) and gcgcgtcgacttagtctccaagaatcagttttac (reverse) followed by digestion with BglII and SalI to yield pCDFDuet-1 MKK6-EE. Murine p38α (Addgene plasmid #20351) (48) was cloned into the BglII and XhoI sites of pCDFDuet-1 MKK6-EE by PCR with the primers gcgcggatccatgtcgcaggagaggccc (forward) and gcgcctcgagtcaggactccatttcttcttgg (reverse) followed by digestion with BamHI and XhoI to yield pCDFDuet-1 MKK6-EE p38α. Human MAPKAPK2 (MK2) (hORFeome V5.1 #10384) (49) was cloned into the BamHI and EcoRI sites of pGEX-4T-1 (3×FLAG) by PCR with the primers gcgcggatccatgctgtccaactcccaggg (forward) and gcgcctcgagtcagtgggccagagccg (reverse) followed by digestion with BamHI and EcoRI to yield pGEX-4T-1 3×FLAG-MK2. Human CREB (hORFeome V5.1 #3038) (49) was cloned into the BamHI and EcoRI sites of pGEX-4T-1 (3×FLAG) by PCR with the primers gcgcggatccatgaccatggaatctggagc (forward) and gcgcgaattcttaatctgatttgtggcagtaaag (reverse) followed by digestion with BamHI and EcoRI to yield pGEX-4T-1 3×FLAG-CREB. Human STAT1 (hORFeome V5.1 #4126) (49) was cloned into the BamHI and EcoRI sites of pGEX-4T-1 (3×FLAG) by PCR with the primers gcgcggatccatgtctcagtggtacgaact (forward) and gcgcgaattcttacacttcagacacagaaatca (reverse) followed by digestion with BamHI and EcoRI to yield pGEX-4T-1 3×FLAG-STAT1.

For constitutive lentiviral overexpression, human CXADR/CAR (hORFeome V5.1 #356) (49) was recombined with pLX304 (Addgene plasmid #25890) (49) using Gateway LR clonase (Invitrogen, Carlsbad, CA) to yield pLX304 CAR-V5. Human DUSP10/MKP5 (hORFeome V5.1 #8448),

DUSP16/MKP7 (hORFeome V5.1 #11351), DUSP19 (hORFeome V5.1 #2039), DUSP22/JSP1 (hORFeome V5.1 #8622), PTPRR/PTP-SL (hORFeome V5.1 #56450), and PPP1R8/NIPP1 (hORFeome V5.1 #6578) were recombined with pLX302 (Addgene plasmid #25896) using Gateway LR clonase (Invitrogen, Carlsbad, CA) to yield pLX302 MKP5-V5, pLX302 MKP7-V5, pLX302 DUSP19-V5, pLX302 JSP1-V5, pLX302 PTP-SL-V5, and pLX302 NIPP1-V5.

For inducible lentiviral expression, human MKK4-EE was cloned into the SpeI and MfeI sites of pEN_TTmiRc2 3×FLAG (50) by PCR with the primers gcgcactagtggatccatgcagggtaaacg (forward) and gcgccaattgctacactttacgttttttcttcggaccagaaccaccatcgacatacatgg (reverse, adding a short linker and the monopartite NLS of SV40 large T antigen) followed by digestion with SpeI and MfeI to yield pEN_TTmiRc2 3×FLAG-MKK4-EE-NLS. Human MKK7a1-EE was cloned into the SpeI and MfeI sites of pEN_TTmiRc2 3×FLAG by PCR with the primers gcgctctagaggatccatgctggggctc (forward) and gcgccaattgctacactttacgttttttcttcggaccagaaccacccctgaagaagggca (reverse, adding a short linker and the monopartite NLS of SV40 large T antigen) followed by digestion with XbaI and MfeI to yield pEN_TTmiRc2 3×FLAG-MKK7-EE-NLS. EGFP was cloned into the SpeI and MfeI sites of pEN_TTmiRc2 3×FLAG by PCR with the primers gcgcactagtgtgagcaagggcgaggagct (forward) and gcgccaattgctacactttacgttttttcttcggaccagaaccaccgtcggcgcgcccac (reverse, adding a short linker and the monopartite NLS of SV40 large T antigen) followed by digestion with SpeI and MfeI to yield pEN_TTmiRc2 3×FLAG-EGFP-NLS. The pEN_TTmiRc2 donor vectors were recombined with pSLIK hygro (50) using Gateway LR clonase (Invitrogen, Carlsbad, CA) to yield pSLIK 3×FLAG-MKK4-EE-NLS, pSLIK 3×FLAG-MKK7-EE-NLS, and pSLIK 3×FLAG-EGFP-NLS.

All PCR-cloned constructs and donor vectors were verified by restriction digest and sequencing, and all plasmids will be available through Addgene.

Protein Induction and Purification — ERK2 and MEK-DD purifications were performed as described previously (29). BL21-CodonPlus (DE3)-RIPL competent cells (#230280, Stratagene, San Diego, CA) were transformed with pGEX-4T-1 or pCDFDuet-1 and pGEX-4T-1 plasmids, and liquid

cultures were grown at 37°C until OD 0.6–1. Cultures were cooled to 12°C for 30–45 minutes and protein expression was induced at 12°C overnight with one of the following isopropyl-D-1-thiogalactopyranoside (IPTG) concentrations: 0.4 mM (CREB, MKK4), 1 mM (p38α, JNK1, STAT1, MKK7), 2 mM (MK2). Bacterial cultures were collected by centrifugation and resuspended in 7.5 mL RIPL TNE buffer (54 mM Tris [pH 7.4], 160 mM NaCl, 1 mM EDTA, 2 μg/mL leupeptin, 5 μg/mL aprotinin, 1 μg/mL pepstatin, 32 mM sodium fluoride, 100 μM Na_3VO_4, 10 mM sodium pyrophosphate, 2 mM ATP, 1.2 mg/mL $MgSO_4$, 13 mM $MgCl_2$, 7 μg/mL DNAse, and 1 mM DTT) per 250 mL culture. Bacteria were mechanically lysed using an EmulsiFlex B15 (Avestin) at 80 psi. Lysates were clarified by centrifugation and flowed over a 5-mL GSTrap column (#17-5131-02, GE Healthcare, Chicago, IL) using an ÄKTAprime Plus chromatography system at 0.1 mL/min (GE Healthcare, Chicago, IL). The column was washed at 0.1 mL/min with 20–25 mL of Buffer A (25 mM sodium phosphate [pH 7.2], 150 mM NaCl), and proteins were eluted in 2 mL fractions with glutathione elution buffer (6 mg/mL glutathione in Buffer A plus 2 mM DTT). For MKK4-EE and MKK7-EE purifications, clarified lysates were incubated with glutathione-agarose beads (Sigma, St. Louis, MO) for 4 hours at 4°C. Beads were then spun down and washed with PBS twice before use.

Phosphorylation of Protein Substrates — ERK2 phosphorylation was performed in vitro with purified MEK-DD as described previously (29). In vivo phosphorylation of p38 and MK2 was achieved by co-transformation of RIPL cells with pCDFDuet-1 MKK6-EE and pCDFDuet-1 MKK6-EE p38α respectively. Phosphorylation of JNK1 was performed in vitro with purified 3×HA-MKK4-EE and 3×HA-MKK7a1-EE bound to glutathione-agarose beads (Sigma, St. Louis, MO) by incubating for 1 hour at 37°C in kinase assay buffer (30 mM Tris [pH 7.5], 3 mM ATP, 45 mM $MgCl_2$, 7.5 mM β-glycerophosphate, 1.5 mM Na_3VO_4, 1.5 mM EGTA, 0.6 mM DTT). The supernatant containing phosphorylated JNK1 was collected after centrifugation of the kinase assay reactions. CREB and STAT1 were phosphorylated in vitro with phospho-MK2 or active JAK1 fragment (#14-918, Millipore, Dundee, UK) respectively by incubation at 37°C in kinase assay buffer for 24 hours.

Phospho-stoichiometry of substrates was assessed in the phosphoprotein preparations relative to unstimulated or stimulated RIPA lysates from AC16-CAR cells by immunoblotting with antibodies specific to the phosphoprotein and the total protein as described below. Phosphoprotein bands were normalized to the total protein immunoreactivity and phospho-to-total ratio was assessed relative to unstimulated cell lysate.

Cell Lines and Culture — MCF10A-5E cells were obtained and cultured as previously reported (51, 52). CVB3-permissive HeLa cells were provided by Dr. Bruce McManus (University of British Columbia, Vancouver BC, Canada) and were cultured in DMEM (#11965092, Gibco, Grand Island, NY) supplemented with 10% fetal bovine serum and 1% penicillin-streptomycin (#15140-122, Gibco, Grand Island, NY). HT-29 cells (ATCC, Manassas, VA) were cultured according to the distributor's recommendations. AC16 cells were purchased from Dr. Mercy Davidson (Columbia University, NY, New York) (53) and cultured in DMEM/F12 (#11330-032, Gibco, Grand Island, NY) supplemented with 12.5% fetal bovine serum and 1% penicillin-streptomycin. AC16-CAR cells were prepared by transducing parental AC16 cells with pLX304 CAR-V5 lentiviruses as described previously (54) and selecting for stable expression with 10 μg/mL blasticidin (#46-1120, Invitrogen, Carlsbad, CA) until control plates had cleared. AC16-CAR cells overexpressing pLX302 MKP7-V5, pLX302 JSP1-V5, pLX302 NIPP1-V5, or pLX302 PTP-SL-V5 were prepared by transducing AC16-CAR cells with lentiviruses as described previously (46). Two days after transduction, cells were either fractionated as described below or selected in 2 μg/mL puromycin (#100552, MP Biomedicals, Santa Ana, CA) plus 10 μg/mL blasticidin (#46-1120, Invitrogen, Carlsbad, CA) until control plates had cleared. AC16-CAR cells dually expressing 3×FLAG-MKK4-EE-NLS and 3×FLAG-MKK7-EE-NLS (3×FLAG-MKK4/7-EE-NLS) or 3×FLAG-EGFP-NLS were prepared by transducing AC16-CAR cells with single or pooled lentiviruses as described previously (54). Two days after transduction, cells were selected for stable integration with 100 μg/mL hygromycin (#ant-hg-5, Invivogen, Toulouse, France) and 10 μg/mL blasticidin (#46-1120, Invitrogen, Carlsbad, CA) until control plates had cleared.

On-plate Subcellular Fractionation — Cells were washed briefly with ice-cold PBS and then incubated with saponin extract (SE) buffer (50 mM HEPES [pH 7.5], 0.05% [w/v] saponin, 20 µg/mL aprotinin, 20 µg/mL leupeptin, 1 µg/mL pepstatin, 2 mM $MgCl_2$, 1 mM DTT, 50 mM 2-mercaptoethanol, 5 mM D-glucose, and 15 µg/mL hexokinase [#H5000, Sigma, St. Louis, MO]) on a platform rocker for 30 minutes at 4ºC. The hexokinase stock for the extraction buffer was prepared at 5 mg/ml with 15 µM phenylmethylsulfonyl fluoride (PMSF). After incubation, the SE fraction was collected and cells were washed three times with 0.05% (w/v) saponin in ice-cold PBS for 5 minutes on ice with rocking. After the third wash, permeabilized cells were incubated with NP40 extract (NE) buffer (50 mM HEPES [pH 7.5], 0.1% [w/v] Nonidet P-40 [NP40], 150 mM NaCl, 20 µg/mL aprotinin, 20 µg/mL leupeptin, 1 µg/mL pepstatin, 2 mM $MgCl_2$, 1 mM DTT, 50 mM 2-mercaptoethanol, 5 mM D-glucose, and 15 µg/mL hexokinase) for 5 minutes on ice with rocking. After incubation, the NE fraction was collected and cells were washed with 0.05% (w/v) saponin in ice-cold PBS for 5 minutes on ice with rocking. Then, the insoluble fraction was collected by addition of 1× sample buffer (62.5 mM Tris pH 6.8, 2% [w/v] sodium dodecyl sulfate [SDS], 10% [v/v] glycerol, 0.01% [w/v] bromophenol blue) and cell scraping. EGF-stimulated subcellular fractions for immunoblotting were lysed in SE and NE buffers supplemented with phosphatase inhibitors (200 µM Na_3VO_4, 10 mM sodium pyrophosphate, and 1 µg/mL microcystin-LR) to preserve phosphoproteins.

Subcellular Protein Phosphatase Assays — High protein-binding 96-well plates (#9018, Corning Costar, Lowell, MA) were coated overnight with recombinant phosphoprotein diluted in 100 µL PBS (see supplemental Table S1 for details). The next morning, plates were washed three times with Tris-buffered saline + 0.1% (v/v) Tween-80 (TBS-T) and blocked for 1 hour at room temperature on platform rocker with 5% (w/v) BSA in TBS-T (blocking buffer) and washed three times with TBS-T before use.

SE and NE fractions were diluted to cellular equivalents (an amount of cell extract estimated from the cellular density at the time of fractionation) that fall within the optimal dynamic range of each assay (see supplemental Tables S2 and S3 for equivalents used in each figure). SE fractions were

diluted to 85 µL in SE buffer, whereas NE fractions were diluted to 85 µL in 10% (v/v) NE buffer + 90% (v/v) NP40- and NaCl-free NE buffer (for phospho-ERK2, phospho-p38α, phospho-JNK, and phospho-STAT1 assays) or 30% (v/v) NE buffer + 70% (v/v) NP40- and NaCl-free NE buffer (for phospho-MK2 and phospho-CREB assays). Diluted extracts were added to the phosphosubstrate-coated plate and incubated in a Jitterbug Microplate Incubator-Shaker (Thomas Scientific, Swedesboro, NJ) at 575 RPM and 30ºC for 30–90 minutes depending on the kinetics of the assay (see supplemental Table S1 for details). Dephosphorylation reactions were terminated with 85 µL of 2× phosphatase inhibitor solution (20 mM sodium pyrophosphate, 60 mM sodium fluoride, and 400 µM Na_3VO_4 in TBS) followed by three washes with 1× phosphatase inhibitor solution diluted in TBS-T.

After washing once with TBS-T lacking phosphatase inhibitors, each well was incubated for one hour at room temperature on a platform rocker with 50 µL of one of the following primary antibodies diluted in blocking buffer: phospho-ERK2 (Thr^{202}/Tyr^{204}) (1:1000, #4370, Cell Signaling Technology, Beverly, MA), phospho-p38 (Thr^{180}/Tyr^{182}) (1:1000, #4511, Cell Signaling Technology, Beverly, MA), phospho-JNK (Thr^{183}/Tyr^{185}) (1:100, #9251, Cell Signaling Technology, Beverly, MA), phospho-MK2 (Thr^{334}) (1:1000, #3007, Cell Signaling Technology, Beverly, MA), phospho-CREB (Ser^{133}) (1:1000, #9198, Cell Signaling Technology, Beverly, MA), phospho-STAT1 (Tyr^{709}) (1:5000, #9167, Cell Signaling Technology, Beverly, MA). Primary antibody solutions were removed and plates washed three times with TBS-T. Each well was then incubated for 1 hour at room temperature on a platform rocker with 50 µL of biotinylated goat anti-rabbit secondary antibody (1:10,000, #111-065-045, Jackson Immunoresearch, West Grove, PA) diluted in blocking buffer. The secondary antibody solution was removed and wells were washed three times with TBS-T followed by incubation for 1 hour at room temperature on a platform rocker with 50 µL of streptavidin-HRP diluted in blocking buffer (1:200, #DY998, R&D Systems, Minneapolis, MN). After washing three times with TBS-T, wells were incubated at room temperature on a platform rocker with 100 µL of 1:1 mix of ELISA Reagent A (stabilized hydrogen peroxide) and Reagent B (stabilized tetramethylbenzidine) (#DY999, R&D Systems,

Minneapolis, MN). ELISA reactions were stopped with 50 µL of 1 M sulfuric acid after 10 minutes, with the exception of phospho-p38α assays that were allowed to proceed for 15 minutes. Well absorbance of the phospho-ELISA endpoint was measured at 450 nm with background correction at 540 nm on an Optima plate reader.

Phosphatase activity was calculated as the decrease in phospho-ELISA signal relative to buffer-only controls. For calibration of relative activities, a two-fold serial dilution of pooled SE or NE fraction was used to prepare a standard alongside the unknown samples. Standards were regressed against input material by using a four-parameter logistic curve, which was inverted to calculate relative phosphatase activity from unknown samples. Last, activity measurements were adjusted for relative total protein concentration as quantified by o-pthalaldehyde assay (see below). For inhibitor studies, concentrated inhibitors were spiked into diluted extracts to achieve a final concentration of 10 mM sodium pyrophosphate, 200 µM activated Na_3VO_4 (55), or 1 µg/mL microcystin-LR before the start of the assay.

Cell lysis — Total cell extracts were prepared in radioimmunoprecipitation assay (RIPA) buffer (25 mM Tris-HCl [pH 7.6], 150 mM NaCl, 1% Nonidet P-40, 1% sodium deoxycholate, 0.1% SDS, 10 µg/mL aprotinin, 10 µg/mL leupeptin, 1 µg/mL pepstatin, 200 µM Na_3VO_4, 1 µg/mL microcystin-LR and 30 µM phenylmethylsulfonyl fluoride [PMSF]) as described previously (56).

Cell Infection and Stimulation — For assessment of the stoichiometry of recombinant phosphosubstrates, AC16-CAR cells were seeded at 50,000 cells/cm^2 for 24 hours and stimulated with EGF (#AF-100-15, Peprotech, Rocky Hill, NJ), TNF (#300-01A, Peprotech, Rocky Hill, NJ), or IFNβ (#300-02BC, Peprotech, Rocky Hill, NJ) by spiking in a 20$\times$ concentrated stock for the indicated times before lysis in RIPA buffer.

For the EGF time course, AC16-CAR cells were seeded at 50,000 cells/cm^2 for 24 hours on a 12-well plate pre-coated for 2 hours with 0.02% [w/v] gelatin (#G9391, Sigma, St. Louis, MO) at 37°C. Cells were either unstimulated or stimulated for 120, 60, 30, 15, or 5 minutes with 100 ng/mL EGF

before simultaneous extraction using the on-plate subcellular fractionation technique described above.

For CVB3 infection of AC16 and AC16-CAR cells, culture plates were coated with 0.02% [w/v] gelatin as described above before plating at ~25,000 cells/cm^2 for 24 hours. Before infection, 75% of the culture medium volume was removed, and virus stock was spiked in at a multiplicity of infection (MOI) of 10 virions per cell. Cells were infected for one hour with gentle rocking every 10–15 minutes, and then cells were washed with PBS and refed with growth medium lacking selection antibiotics until lysis. In the full-factorial experiment with type I/II interferons, CVB3-infected cells were stimulated with 30 ng/mL IFNβ, 50 U/mL IFNγ (#11040596001, Roche, Mannheim, Germany), or both by spiking in cytokine stocks at 3 hours after the start of CVB3 infection (two hours after refeeding). After 4 hours of cytokine stimulation, SE and NE fractions were prepared as described above.

For experiments involving JNK inhibition, AC16-CAR cells were seeded ~25,000 cells/cm^2 for 21 hours and treated with 1 μM JNK-IN-8 (#sc-364745, Santa Cruz Biotechnology, Santa Cruz, CA) prepared as a 1 mM stock in DMSO. Three hours after JNK-IN-8 addition, cells were infected and stimulated with 30 ng/mL IFNβ as described above. Cells were lysed in RIPA buffer 20 hours after the start of CVB3 infection.

For the genetic perturbation of JNK activity, AC16-CAR cells stably expressing inducible 3×FLAG-MKK4/7-EE-NLS or 3×FLAG-EGFP-NLS control were seeded at ~25,000 cells/cm^2. To induce expression, 1 μg/mL doxycycline hyclate (#D9891, Sigma, St. Louis, MO) was added two hours before the start of CVB3 infection (MOI = 10), and 30 ng/mL IFNβ was added 3 hours after the start of CVB3 infection as before. Cells were lysed in RIPA buffer 20 hours after the start of CVB3 infection.

Protein Quantification — RIPA lysates were quantified for total protein as previously described (56). Subcellular extracts were quantified by o-pthalaldehyde assay with incomplete phthaldialdehyde reagent (#P7914, Sigma, St. Louis, MO) in 96-well black-walled, clear-bottom microtiter plates (#3720, Corning, Lowell, MA). Phthaldialdehyde reagent was activated with 1/500th volume of 2-mercaptoethanol and then 50 μL of activated reagent was incubated with 10 μL of sample for 2 minutes

on an orbital shaker at room temperature. Fluorescence (λ_{ex} = 355 nm, λ_{em} = 440 nm) was detected using an Optima plate reader. All subcellular extracts were regressed against a bovine serum albumin standard run on the same plate under the same conditions.

ATP Quantification — Subcellular SE and NE fractions were collected with or without hexokinase in the extraction buffer. ATP concentration in the extracts was quantified using the Kinase-Glo Assay (#V6701, Promega, Madison, WI). Extracts (25 µL) or ATP standards were incubated with 25 µL of Kinase-Glo Reagent for 10 minutes at room temperature in black-walled, solid-bottom microtiter plates (#655209, Greiner Bio-One, Kremsmünster, Austria). Luminescence was detected using an Optima Plate reader. ATP standards were diluted in either SE or NE buffer lacking glucose and saponin, which act as substrates for hexokinase and cause loss of luminescence in the ATP standards.

Plaque Assay — CVB3-permissive HeLa cells were plated at 1 million cells/well in a 6-well dish overnight, washed, and incubated with 200 µL of diluted conditioned medium from AC16 or AC16-CAR cells infected with CVB3 for 24 hours. HeLa cells were infected for 40 minutes, washed with serum-free DMEM, and overlaid with 2 mL of a 1:1 mix of 1.5% (w/v) agar and 2× DMEM (#12100-046, Gibco, Grand Island, NY) for 72 hours. Wells were fixed with 2 mL of Carnoy's fixative (75% [v/v] ethanol, 25% [v/v] acetic acid) for 30 minutes at room temperature. Fixative was decanted and agar plugs removed with a pliable weighing spatula. Viral plaques were counterstained with 0.5% (w/v) crystal violet. Plates were scanned on a LI-COR Odyssey scanner in the 700 channel.

Immunofluorescence — Glass coverslips were coated with 2 µg/cm^2 poly-D-lysine (#P6407, Sigma, St. Louis, MO) in a 6-well dish for 5 minutes, washed briefly with cell culture grade water, and allowed to dry for at least 2 hours. AC16 or AC16-CAR cells were plated at 20,000 cells/cm^2 for 24 hours and then infected as described above. Cells were LIVE/DEAD stained and processed for immunofluorescence as described (39, 54) with the following primary antibodies: mouse anti-VP1 (1:1000, #M7064, Dako, Carpinteria, CA) and rabbit anti-cleaved caspase 3 antibody (1:200, #9661,

Cell Signaling Technology, Beverly, MA). For MKK4/7-EE-NLS and EGFP-NLS lines, cells were plated in medium containing 1 µg/mL doxycycline to induce expression. Cells were processed for immunofluorescence as described (39, 54) with the following primary antibodies: rabbit anti-p-cJun (1:100, #9164, Cell Signaling Technology, Beverly, MA), mouse anti-FLAG (1:200, #F3165, Sigma, St. Louis, MO).

Immunoblotting — Quantitative immunoblotting of RIPA lysates and subcellular extracts was performed as described (56) with the following primary antibodies: caspase 3 (1:1000, #9662, Cell Signaling Technology, Beverly, MA), eIF4G (1:1000, #2498, Cell Signaling Technology, Beverly, MA), FLAG (1:5000, #F3165, Sigma, St. Louis, MO), HSP90 (1:2000, #sc-7947, Santa Cruz Biotechnology, Santa Cruz, CA), IκBα (1:1000, #4814, Cell Signaling Technology, Beverly, MA), JunD (1:1000, #sc-74, Santa Cruz Biotechnology, Santa Cruz, CA), MEK1/2 (1:1000, #4694, Cell Signaling Technology, Beverly, MA), MKP3 (1:1000, #2138, Epitomics, Burlingame, CA), PARP (1:1000, #9532, Cell Signaling Technology, Beverly, MA), PP1c (1:1000, custom polyclonal from D.L.B.), PP2Ac (1:1000, custom polyclonal from D.L.B.), tubulin (#ab89984, Abcam, Cambridge, MA), V5 (1:5000, #46-0705, Invitrogen, Carlsbad, CA), VP1 (1:1000, #M7064, Dako, Carpinteria, CA), phospho-ERK2 (Thr^{202}/Tyr^{204}) (1:1000, #4370, Cell Signaling Technology, Beverly, MA), total ERK (1:1000, #4695, Cell Signaling Technologies, Beverly, MA), phospho-p38 (Thr^{180}/Tyr^{182}) (1:1000, #4511, Cell Signaling Technology, Beverly, MA), total p38 (1:5000, #sc-535, Santa Cruz Biotechnology, Santa Cruz, CA), phospho-JNK (Thr^{183}/Tyr^{185}) (1:100, #9251, Cell Signaling Technology, Beverly, MA), total JNK (1:1000, #9252, Cell Signaling Technology, Beverly, MA), phospho-MK2 (Thr^{334}) (1:1000, #3007, Cell Signaling Technology, Beverly, MA), total MK2 (1:500, #ADI-KAP-MA015-F, Enzo Life Sciences, Farmingdale, NY), phospho-CREB (Ser^{133}) (1:1000, #9198, Cell Signaling Technology, Beverly, MA), total CREB (1:1000, #9197, Cell Signaling Technology, Beverly, MA), phospho-STAT1 (Tyr^{709}) (1:1000, #9167, Cell Signaling Technology, Beverly, MA), and total STAT1 (1:1000, #9172, Cell Signaling Technology, Beverly, MA).

MKP1, DUSP19-V5 and MKP5-V5 phosphatases were immunoblotted by chemiluminescence as described (56) using the following primary antibodies: MKP1 (1:200, #sc-1102, Santa Cruz

Biotechnology, Santa Cruz, CA), V5 (1:5000, #46-0705, Invitrogen, Carlsbad, CA), and MKP5 (1:1000, #3483, Cell Signaling Technology, Beverly, MA). Blots were then stripped for 30 minutes at 50°C in high stringency stripping buffer (2% [w/v] SDS, 62.5mM Tris pH 6.8, 100mM 2-mercaptoethanol in water) and reprobed for vinculin (1:10,000, #05-386, EMD Millipore, Dramstadt, Germany) and GAPDH (1:20,000, #AM4300, Thermo Fisher Scientific, Waltham, MA) as loading controls.

shRNA cloning and validation — The following shRNA sequences were obtained from the RNAi Consortium and cloned into tet-pLKO-puro (57) as previously described (58): shMKP1 (#1: TRCN0000356127 and #2: TRCN0000367631), shMKP5 (#1: TRCN0000220147 and #2: TRCN0000314618), shMKP7 (#1: TRCN0000052013 and #2: TRCN0000052017), and shDUSP19 (TRCN0000356162). Lentiviruses were packaged, transduced into AC16-CAR cells, and selected with 2 μg/mL puromycin and 100 μg/mL blasticidin as previously described (54). shRNAs in AC16-CAR stable lines were induced with 1 μg/mL doxycycline for 72 hours before the start of the experiment. shMKP5 and shDUSP19 sequences were validated by transient co-transfection with pLX302 MKP5-V5 and pLX302 DUSP19-V5, respectively, using Lipofectamine 2000 (#11668019, Invitrogen, Carlsbad, CA) in the presence of 1 μg/mL doxycycline for 48 hours. shMKP1 sequences were verified in AC16-CAR stable lines induced with 1 μg/mL doxycycline 24 hours prior to stimulation with 100 ng/mL EGF for 1 hour.

Experimental Design and Statistical Rationale — The number of samples analyzed per experiment is indicated by "*n* =" at the bottom of each figure legend, where the distinction is made between assay replicates (same extract, different microtiter wells) and biological replicates (different extracts). All quantitative data were collected with $n \geq 3$ replicates, providing ~82% minimum power to detect a 1.5-fold difference in unpaired means according to noncentral *t* statistics assuming a coefficient of variation (CV) of 20%, which conservatively models error in the assay. Among biological replicates, the error of some assays was much higher (CV = 30–50%), prompting a paired design with $n = 9$ samples to maintain ~75% minimum power to detect a 1.5-fold difference when CV = 50%.

Negative controls in the phosphatase assays (n = 4–14) were phosphosubstrate-coated wells incubated with the appropriate extraction buffer instead of cellular extract. Negative controls in the biological studies (n = 9) were cells treated with viral or cytokine diluent lacking CVB3 or cytokines. No randomization of plates or wells within plates was performed, but lack of spatial bias or artifacts was confirmed retrospectively.

Statistical analysis — Standard statistical analyses are described in the figure subpanel legend where used. For the full-factorial experiment involving CVB3, IFNβ, and IFNγ, the assumption of normally distributed biological replicates was assessed by Lilliefors test. Given their empirical cumulative distribution functions, the null hypothesis was rejected for the following phosphatase assays: phospho-JNK1 (SE fraction), phospho-MK2 (SE fraction), phospho-CREB (SE and NE fractions), and phospho-STAT1 (SE and NE fractions). For these six assays, differences in relative ranks were assessed by rank-sum test with Bonferroni correction for multiple-hypothesis testing, and main effects or two-factor interactions were assessed by the three-way extension of the Scheirer-Ray-Hare test at a 10% false-discovery rate. For the remaining six assays where the normality assumption could be retained, differences in means were assessed by two-tailed Student's t test with Bonferroni correction for multiple-hypothesis testing, and main effects or two-factor interactions were assessed by three-way ANOVA at a 10% false-discovery rate.

Assay	Substrate amount per well	Assay reaction time SE Fraction	NE Fraction
pERK2	16 ng	60 min	60 min
pp38α	250 ng	60 min	30 min
pJNK1	16 ng	60 min	30 min
pMK2	16 ng	90 min	90 min
pCREB	62 ng	90 min	90 min
pSTAT1	62 ng	60 min	60 min

Table S1. Substrate adsorption and phosphatase incubation conditions for the subcellular activity assays. Substrate amounts are based on the linear range of the phospho-ELISA (Figure 7), assay durations are based on the kinetics of the phosphatase (Figure 10).

Assay	SE Fraction	NE Fraction
pERK2	6250 cells	6250 cells
pp38α	6250 cells	6250 cells
pJNK1	6250 cells	3125 cells
pMK2	18750 cells	25000 cells
pCREB	25000 cells	25000 cells
pSTAT1	25000 cells	6250 cells

Table S2. Extract amounts used for the reaction kinetics (Figure 10) and phosphatase inhibitor experiments (Figure 12). Cell equivalents were titrated to fall near the top of the linear range of each calibration curve (Figure 11).

Assay	SE Fraction	NE Fraction
pERK2	1000 cells	3000 cells
pp38α	2000 cells	2000 cells
pJNK1	3000 cells	2000 cells
pMK2	3000 cells	10000 cells
pCREB	6000 cells	20000 cells
pSTAT1	6000 cells	3000 cells

Table S3. Extract amounts used for the full-factorial CVB3–IFNβ–IFNγ experiment (Figure 16). Cell equivalents were titrated to fall in the middle of the linear range of each calibration curve (Figure 11).

2.5 References

1. Downward, J. (2001) The ins and outs of signalling. *Nature* 411, 759-762
2. Hunter, T. (1995) Protein kinases and phosphatases: the yin and yang of protein phosphorylation and signaling. *Cell* 80, 225-236
3. Tonks, N. K. (2006) Protein tyrosine phosphatases: from genes, to function, to disease. *Nat Rev Mol Cell Biol* 7, 833-846
4. Cohen, P. T. W. (2002) Protein phosphatase 1 – targeted in many directions. *Journal of Cell Science* 115, 241-256
5. Owens, D. M., and Keyse, S. M. (2007) Differential regulation of MAP kinase signalling by dual-specificity protein phosphatases. *Oncogene* 26, 3203-3213
6. Heinrich, R., Neel, B. G., and Rapoport, T. A. (2002) Mathematical Models of Protein Kinase Signal Transduction. *Mol. Cell* 9, 957-970
7. Bhalla, U. S., Ram, P. T., and Iyengar, R. (2002) MAP kinase phosphatase as a locus of flexibility in a mitogen-activated protein kinase signaling network. *Science* 297, 1018-1023
8. Auger-Messier, M., Accornero, F., Goonasekera, S. A., Bueno, O. F., Lorenz, J. N., van Berlo, J. H., Willette, R. N., and Molkentin, J. D. (2013) Unrestrained p38 MAPK Activation in Dusp1/4 Double-Null Mice Induces Cardiomyopathy. *Circulation Research* 112, 48-56
9. Keyse, S. M. (2008) Dual-specificity MAP kinase phosphatases (MKPs) and cancer. *Cancer and Metastasis Reviews* 27, 253-261
10. Zhao, Q., Wang, X., Nelin, L. D., Yao, Y., Matta, R., Manson, M. E., Baliga, R. S., Meng, X., Smith, C. V., Bauer, J. A., Chang, C.-H., and Liu, Y. (2006) MAP kinase phosphatase 1 controls innate immune responses and suppresses endotoxic shock. *J Exp Med* 203, 131-140
11. Brewis, N., Ohst, K., Fields, K., Rapacciuolo, A., Chou, D., Bloor, C., Dillmann, W., Rockman, H., and Walter, G. (2000) Dilated cardiomyopathy in transgenic mice expressing a mutant A subunit of protein phosphatase 2A. *American Journal of Physiology - Heart and Circulatory Physiology* 279, H1307-H1318
12. Arena, S., Benvenuti, S., and Bardelli, A. (2005) Genetic analysis of the kinome and phosphatome in cancer. *Cellular and Molecular Life Sciences* 62, 2092-2099
13. Shi, Y. (2009) Serine/Threonine Phosphatases: Mechanism through Structure. *Cell* 139, 468-484
14. Zhang, Y. Y., Wu, J. W., and Wang, Z. X. (2011) A distinct interaction mode revealed by the crystal structure of the kinase p38alpha with the MAPK binding domain of the phosphatase MKP5. *Sci Signal* 4, ra88
15. Wood, C. D., Thornton, T. M., Sabio, G., Davis, R. A., and Rincon, M. (2009) Nuclear localization of p38 MAPK in response to DNA damage. *Int J Biol Sci* 5, 428-437
16. Gong, X., Ming, X., Deng, P., and Jiang, Y. (2010) Mechanisms regulating the nuclear translocation of p38 MAP kinase. *J Cell Biochem* 110, 1420-1429
17. Ben-Levy, R., Hooper, S., Wilson, R., Paterson, H. F., and Marshall, C. J. (1998) Nuclear export of the stress-activated protein kinase p38 mediated by its substrate MAPKAP kinase-2. *Curr Biol* 8, 1049-1057
18. Lenormand, P., Sardet, C., Pages, G., L'Allemain, G., Brunet, A., and Pouyssegur, J. (1993) Growth factors induce nuclear translocation of MAP kinases (p42mapk and p44mapk) but not of their activator MAP kinase kinase (p45mapkk) in fibroblasts. *J Cell Biol* 122, 1079-1088

19. Wang, J., Tang, R., Lv, M., Wang, Q., Zhang, X., Guo, Y., Chang, H., Qiao, C., Xiao, H., Li, X., Li, Y., Shen, B., and Zhang, J. (2011) Defective anchoring of JNK1 in the cytoplasm by MKK7 in Jurkat cells is associated with resistance to Fas-mediated apoptosis. *Mol Biol Cell* 22, 117-127
20. Alessi, D. R., Gomez, N., Moorhead, G., Lewis, T., Keyse, S. M., and Cohen, P. (1995) Inactivation of p42 MAP kinase by protein phosphatase 2A and a protein tyrosine phosphatase, but not CL100, in various cell lines. *Current Biology* 5, 283-295
21. Scott, J. D., and Pawson, T. (2009) Cell Signaling in Space and Time: Where Proteins Come Together and When They're Apart. *Science* 326, 1220-1224
22. Moorhead, G. B., Trinkle-Mulcahy, L., and Ulke-Lemee, A. (2007) Emerging roles of nuclear protein phosphatases. *Nat. Rev. Mol. Cell Biol.* 8, 234-244
23. Sacco, F., Perfetto, L., Castagnoli, L., and Cesareni, G. (2012) The human phosphatase interactome: An intricate family portrait. *Febs Letters* 586, 2732-2739
24. Kameshita, I., Baba, H., Umeda, Y., and Sueyoshi, N. (2010) In-gel protein phosphatase assay using fluorogenic substrates. *Anal. Biochem.* 400, 118-122
25. Burridge, K., and Nelson, A. (1995) An in-gel assay for protein tyrosine phosphatase activity: detection of widespread distribution in cells and tissues. *Anal. Biochem.* 232, 56-64
26. McAvoy, T., and Nairn, A. C. (2010) Serine/Threonine Protein Phosphatase Assays. *Curr Protoc Mol Biol* CHAPTER, Unit18.18
27. Montalibet, J., Skorey, K. I., and Kennedy, B. P. (2005) Protein tyrosine phosphatase: enzymatic assays. *Methods* 35, 2-8
28. Geladopoulos, T. P., Sotiroudis, T. G., and Evangelopoulos, A. E. (1991) A malachite green colorimetric assay for protein phosphatase activity. *Anal. Biochem.* 192, 112-116
29. Bose, A. K., and Janes, K. A. (2013) A high-throughput assay for phosphoprotein-specific phosphatase activity in cellular extracts. *Mol Cell Proteomics* 12, 797-806
30. Burch, G. E., Sun, S. C., Chu, K. C., Sohal, R. S., and Colcolough, H. L. (1968) Interstitial and coxsackievirus B myocarditis in infants and children. A comparative histologic and immunofluorescent study of 50 autopsied hearts. *JAMA* 203, 1-8
31. Cooper, L. T., Jr. (2009) Myocarditis. *N Engl J Med* 360, 1526-1538
32. Liu, P., Aitken, K., Kong, Y. Y., Opavsky, M. A., Martino, T., Dawood, F., Wen, W. H., Kozieradzki, I., Bachmaier, K., Straus, D., Mak, T. W., and Penninger, J. M. (2000) The tyrosine kinase p56lck is essential in coxsackievirus B3-mediated heart disease. *Nat. Med.* 6, 429-434
33. Shenoy-Scaria, A. M., Kwong, J., Fujita, T., Olszowy, M. W., Shaw, A. S., and Lublin, D. M. (1992) Signal transduction through decay-accelerating factor. Interaction of glycosyl-phosphatidylinositol anchor and protein tyrosine kinases p56lck and p59fyn 1. *J. Immunol.* 149, 3535-3541
34. Coyne, C. B., and Bergelson, J. M. (2006) Virus-induced Abl and Fyn kinase signals permit coxsackievirus entry through epithelial tight junctions. *Cell* 124, 119-131
35. Garmaroudi, F. S., Marchant, D., Si, X., Khalili, A., Bashashati, A., Wong, B. W., Tabet, A., Ng, R. T., Murphy, K., Luo, H., Janes, K. A., and McManus, B. M. (2010) Pairwise network mechanisms in the host signaling response to coxsackievirus B3 infection. *Proc. Natl. Acad. Sci. U.S.A.* 107, 17053-17058
36. Jensen, E. C. (2013) Quantitative analysis of histological staining and fluorescence using ImageJ. *Anat Rec (Hoboken)* 296, 378-381

37. Huber, M., Watson, K. A., Selinka, H. C., Carthy, C. M., Klingel, K., McManus, B. M., and Kandolf, R. (1999) Cleavage of RasGAP and phosphorylation of mitogen-activated protein kinase in the course of coxsackievirus B3 replication. *J Virol* 73, 3587-3594
38. Si, X., Luo, H., Morgan, A., Zhang, J., Wong, J., Yuan, J., Esfandiarei, M., Gao, G., Cheung, C., and McManus, B. M. (2005) Stress-activated protein kinases are involved in coxsackievirus B3 viral progeny release. *J. Virol.* 79, 13875-13881
39. Jensen, Karin J., Garmaroudi, Farshid S., Zhang, J., Lin, J., Boroomand, S., Zhang, M., Luo, Z., Yang, D., Luo, H., McManus, Bruce M., and Janes, Kevin A. (2013) An ERK-p38 Subnetwork Coordinates Host Cell Apoptosis and Necrosis during Coxsackievirus B3 Infection. *Cell Host & Microbe* 13, 67-76
40. Luo, H., Yanagawa, B., Zhang, J., Luo, Z., Zhang, M., Esfandiarei, M., Carthy, C., Wilson, J. E., Yang, D., and McManus, B. M. (2002) Coxsackievirus B3 Replication Is Reduced by Inhibition of the Extracellular Signal-Regulated Kinase (ERK) Signaling Pathway. *J. Virol.* 76, 3365-3373
41. Coyne, C. B., Bozym, R., Morosky, S. A., Hanna, S. L., Mukherjee, A., Tudor, M., Kim, K. S., and Cherry, S. (2011) Comparative RNAi screening reveals host factors involved in enterovirus infection of polarized endothelial monolayers. *Cell Host & Microbe* 9, 70-82
42. Li, Q., Zheng, Z., Liu, Y., Zhang, Z., Liu, Q., Meng, J., Ke, X., Hu, Q., and Wang, H. (2016) 2C Proteins of Enteroviruses Suppress IKKbeta Phosphorylation by Recruiting Protein Phosphatase 1. *J Virol* 90, 5141-5151
43. Seko, Y., Takahashi, N., Yagita, H., Okumura, K., and Yazaki, Y. (1997) Expression of cytokine mRNAs in murine hearts with acute myocarditis caused by coxsackievirus b3. *J Pathol* 183, 105-108
44. Huhn, M. H., Hultcrantz, M., Lind, K., Ljunggren, H. G., Malmberg, K. J., and Flodstrom-Tullberg, M. (2008) IFN-gamma production dominates the early human natural killer cell response to Coxsackievirus infection. *Cell Microbiol* 10, 426-436
45. Platanias, L. C. (2005) Mechanisms of type-I- and type-II-interferon-mediated signalling. *Nat Rev Immunol* 5, 375-386
46. Weil, J., Epstein, C. J., Epstein, L. B., Sedmak, J. J., Sabran, J. L., and Grossberg, S. E. (1983) A Unique Set of Polypeptides Is Induced by Gamma-Interferon in Addition to Those Induced in Common with Alpha-Interferon and Beta-Interferon. *Nature* 301, 437-439
47. Raingeaud, J., Whitmarsh, A. J., Barrett, T., Derijard, B., and Davis, R. J. (1996) MKK3- and MKK6-regulated gene expression is mediated by the p38 mitogen-activated protein kinase signal transduction pathway. *Mol Cell Biol* 16, 1247-1255
48. Enslen, H., Raingeaud, J., and Davis, R. J. (1998) Selective activation of p38 mitogen-activated protein (MAP) kinase isoforms by the MAP kinase kinases MKK3 and MKK6. *J Biol Chem* 273, 1741-1748
49. Yang, X., Boehm, J. S., Yang, X., Salehi-Ashtiani, K., Hao, T., Shen, Y., Lubonja, R., Thomas, S. R., Alkan, O., Bhimdi, T., Green, T. M., Johannessen, C. M., Silver, S. J., Nguyen, C., Murray, R. R., Hieronymus, H., Balcha, D., Fan, C., Lin, C., Ghamsari, L., Vidal, M., Hahn, W. C., Hill, D. E., and Root, D. E. (2011) A public genome-scale lentiviral expression library of human ORFs. *Nat Methods* 8, 659-661
50. Shin, K. J., Wall, E. A., Zavzavadjian, J. R., Santat, L. A., Liu, J., Hwang, J. I., Rebres, R., Roach, T., Seaman, W., Simon, M. I., and Fraser, I. D. (2006) A single lentiviral vector platform for microRNA-based conditional RNA interference and coordinated transgene expression. *Proc. Natl. Acad. Sci. U. S. A.* 103, 13759-13764

51. Debnath, J., Muthuswamy, S. K., and Brugge, J. S. (2003) Morphogenesis and oncogenesis of MCF-10A mammary epithelial acini grown in three-dimensional basement membrane cultures. *Methods* 30, 256-268
52. Janes, K. A., Wang, C. C., Holmberg, K. J., Cabral, K., and Brugge, J. S. (2010) Identifying single-cell molecular programs by stochastic profiling. *Nat. Methods* 7, 311-317
53. Davidson, M. M., Nesti, C., Palenzuela, L., Walker, W. F., Hernandez, E., Protas, L., Hirano, M., and Isaac, N. D. (2005) Novel cell lines derived from adult human ventricular cardiomyocytes. *J Mol Cell Cardiol* 39, 133-147
54. Wang, L., Brugge, J. S., and Janes, K. A. (2011) Intersection of FOXO- and RUNX1-mediated gene expression programs in single breast epithelial cells during morphogenesis and tumor progression. *Proc Natl Acad Sci U S A* 108, E803-812
55. Hill, M. M., and Hemmings, B. A. (2002) Analysis of protein kinase B/Akt. *Methods Enzymol.* 345, 448-463
56. Janes, K. A. (2015) An analysis of critical factors for quantitative immunoblotting. *Sci Signal* 8, rs2
57. Wiederschain, D., Wee, S., Chen, L., Loo, A., Yang, G., Huang, A., Chen, Y., Caponigro, G., Yao, Y. M., Lengauer, C., Sellers, W. R., and Benson, J. D. (2009) Single-vector inducible lentiviral RNAi system for oncology target validation. *Cell Cycle* 8, 498-504
58. Bajikar, S. S., Fuchs, C., Roller, A., Theis, F. J., and Janes, K. A. (2014) Parameterizing cell-to-cell regulatory heterogeneities via stochastic transcriptional profiles. *Proc. Natl. Acad. Sci. U. S. A.* 111, E626-635
59. Goldenthal, K. L., Hedman, K., Chen, J. W., August, J. T., and Willingham, M. C. (1985) Postfixation detergent treatment for immunofluorescence suppresses localization of some integral membrane proteins. *J Histochem Cytochem* 33, 813-820
60. Meng, T.-C., Fukada, T., and Tonks, N. K. (2002) Reversible Oxidation and Inactivation of Protein Tyrosine Phosphatases In Vivo. *Mol. Cell* 9, 387-399
61. Espina, V., Edmiston, K. H., Heiby, M., Pierobon, M., Sciro, M., Merritt, B., Banks, S., Deng, J., VanMeter, A. J., Geho, D. H., Pastore, L., Sennesh, J., Petricoin, E. F., and Liotta, L. A. (2008) A portrait of tissue phosphoprotein stability in the clinical tissue procurement process. *Mol. Cell Proteomics* 7, 1998-2018
62. Bretscher, M. S., and Munro, S. (1993) Cholesterol and the Golgi apparatus. *Science* 261, 1280-1281
63. Ribbeck, K., and Gorlich, D. (2001) Kinetic analysis of translocation through nuclear pore complexes. *EMBO J* 20, 1320-1330
64. Zheng, C. F., and Guan, K. L. (1994) Cytoplasmic localization of the mitogen-activated protein kinase activator MEK. *Journal of Biological Chemistry* 269, 19947-19952
65. Baeuerle, P. A., and Baltimore, D. (1988) I kappa B: a specific inhibitor of the NF-kappa B transcription factor. *Science* 242, 540-546
66. Laemmli, U. K. (1970) Cleavage of structural proteins during the assembly of the head of bacteriophage T4. *Nature* 227, 680-685
67. Paine, P. L., Moore, L. C., and Horowitz, S. B. (1975) Nuclear envelope permeability. *Nature* 254, 109-114
68. Masuda, K., Shima, H., Watanabe, M., and Kikuchi, K. (2001) MKP-7, a novel mitogen-activated protein kinase phosphatase, functions as a shuttle protein. *J Biol Chem* 276, 39002-39011

69. Jagiello, I., Van Eynde, A., Vulsteke, V., Beullens, M., Boudrez, A., Keppens, S., Stalmans, W., and Bollen, M. (2000) Nuclear and subnuclear targeting sequences of the protein phosphatase-1 regulator NIPP1. *J Cell Sci* 113 Pt 21, 3761-3768
70. Schwertassek, U., Buckley, D. A., Xu, C. F., Lindsay, A. J., McCaffrey, M. W., Neubert, T. A., and Tonks, N. K. (2010) Myristoylation of the dual-specificity phosphatase c-JUN N-terminal kinase (JNK) stimulatory phosphatase 1 is necessary for its activation of JNK signaling and apoptosis. *FEBS J* 277, 2463-2473
71. Van Den Maagdenberg, A. M., Bachner, D., Schepens, J. T., Peters, W., Fransen, J. A., Wieringa, B., and Hendriks, W. J. (1999) The mouse Ptprr gene encodes two protein tyrosine phosphatases, PTP-SL and PTPBR7, that display distinct patterns of expression during neural development. *Eur J Neurosci* 11, 3832-3844
72. Buschbeck, M., Eickhoff, J., Sommer, M. N., and Ullrich, A. (2002) Phosphotyrosine-specific phosphatase PTP-SL regulates the ERK5 signaling pathway. *J Biol Chem* 277, 29503-29509
73. Hendriks, W. J., Dilaver, G., Noordman, Y. E., Kremer, B., and Fransen, J. A. (2009) PTPRR protein tyrosine phosphatase isoforms and locomotion of vesicles and mice. *Cerebellum* 8, 80-88
74. Chirivi, R. G., Dilaver, G., van de Vorstenbosch, R., Wanschers, B., Schepens, J., Croes, H., Fransen, J., and Hendriks, W. (2004) Characterization of multiple transcripts and isoforms derived from the mouse protein tyrosine phosphatase gene Ptprr. *Genes Cells* 9, 919-933
75. Benson, J. R., and Hare, P. E. (1975) O-phthalaldehyde: fluorogenic detection of primary amines in the picomole range. Comparison with fluorescamine and ninhydrin. *Proceedings of the National Academy of Sciences* 72, 619-622
76. Schulze, I. T., and Colowick, S. P. (1969) The modification of yeast hexokinases by proteases and its relationship to the dissociation of hexokinase into subunits. *Journal of Biological Chemistry* 244, 2306-2316
77. Vambutas, V., Kaplan, D. R., Sells, M. A., and Chernoff, J. (1995) Nerve growth factor stimulates tyrosine phosphorylation and activation of Src homology-containing protein-tyrosine phosphatase 1 in PC12 cells. *Journal of Biological Chemistry* 270, 25629-25633
78. Resink, T. J., Hemmings, B. A., Tung, H. Y. L., and Cohen, P. (1983) Characterisation of a Reconstituted Mg-ATP-Dependent Protein Phosphatase. *European Journal of Biochemistry* 133, 455-461
79. Gordon, J. A. (1991) Use of vanadate as protein-phosphotyrosine phosphatase inhibitor. In: Tony Hunter, B. M. S., ed. *Methods Enzymol.*, pp. 477-482, Academic Press
80. Crans, D. C., Smee, J. J., Gaidamauskas, E., and Yang, L. (2004) The chemistry and biochemistry of vanadium and the biological activities exerted by vanadium compounds. *Chem Rev* 104, 849-902
81. Swingle, M., Ni, L., and Honkanen, R. E. (2007) Small-molecule inhibitors of ser/thr protein phosphatases: specificity, use and common forms of abuse. *Methods Mol. Biol.* 365, 23-38
82. MacKintosh, C., Beattie, K. A., Klumpp, S., Cohen, P., and Codd, G. A. (1990) Cyanobacterial microcystin-LR is a potent and specific inhibitor of protein phosphatases 1 and 2A from both mammals and higher plants. *FEBS Letters* 264, 187-192
83. Zhou, B., and Zhang, Z.-Y. (2002) The Activity of the Extracellular Signal-regulated Kinase 2 Is Regulated by Differential Phosphorylation in the Activation Loop. *Journal of Biological Chemistry* 277, 13889-13899

84. Askari, N., Beenstock, J., Livnah, O., and Engelberg, D. (2009) p38alpha is active in vitro and in vivo when monophosphorylated at threonine 180. *Biochemistry* 48, 2497-2504
85. Sun, H., Charles, C. H., Lau, L. F., and Tonks, N. K. (1993) MKP-1 (3CH134), an immediate early gene product, is a dual specificity phosphatase that dephosphorylates MAP kinase in vivo. *Cell* 75, 487-493
86. Kucharska, A., Rushworth, L. K., Staples, C., Morrice, N. A., and Keyse, S. M. (2009) Regulation of the inducible nuclear dual-specificity phosphatase DUSP5 by ERK MAPK. *Cellular Signalling* 21, 1794-1805
87. Park, J. E., Lee, J. A., Park, S. G., Lee, D. H., Kim, S. J., Kim, H. J., Uchida, C., Uchida, T., Park, B. C., and Cho, S. (2012) A critical step for JNK activation: isomerization by the prolyl isomerase Pin1. *Cell Death Differ.* 19, 153-161
88. Zhou, X. Z., Kops, O., Werner, A., Lu, P. J., Shen, M., Stoller, G., Kullertz, G., Stark, M., Fischer, G., and Lu, K. P. (2000) Pin1-dependent prolyl isomerization regulates dephosphorylation of Cdc25C and tau proteins. *Mol. Cell* 6, 873-883
89. Lee, T., Kim, S. J., and Sumpio, B. E. (2003) Role of PP2A in the regulation of p38 MAPK activation in bovine aortic endothelial cells exposed to cyclic strain. *J. Cell. Physiol.* 194, 349-355
90. Amit, I., Citri, A., Shay, T., Lu, Y., Katz, M., Zhang, F., Tarcic, G., Siwak, D., Lahad, J., Jacob-Hirsch, J., Amariglio, N., Vaisman, N., Segal, E., Rechavi, G., Alon, U., Mills, G. B., Domany, E., and Yarden, Y. (2007) A module of negative feedback regulators defines growth factor signaling. *Nat. Genet.* 39, 503-512
91. Fu, X. Y., and Zhang, J. J. (1993) Transcription factor p91 interacts with the epidermal growth factor receptor and mediates activation of the c-fos gene promoter. *Cell* 74, 1135-1145
92. Leaman, D. W., Pisharody, S., Flickinger, T. W., Commane, M. A., Schlessinger, J., Kerr, I. M., Levy, D. E., and Stark, G. R. (1996) Roles of JAKs in activation of STATs and stimulation of c-fos gene expression by epidermal growth factor. *Mol Cell Biol* 16, 369-375
93. Dorner, A. A., Wegmann, F., Butz, S., Wolburg-Buchholz, K., Wolburg, H., Mack, A., Nasdala, I., August, B., Westermann, J., Rathjen, F. G., and Vestweber, D. (2005) Coxsackievirus-adenovirus receptor (CAR) is essential for early embryonic cardiac development. *J Cell Sci* 118, 3509-3521
94. Noutsias, M., Fechner, H., de Jonge, H., Wang, X., Dekkers, D., Houtsmuller, A. B., Pauschinger, M., Bergelson, J., Warraich, R., Yacoub, M., Hetzer, R., Lamers, J., Schultheiss, H. P., and Poller, W. (2001) Human coxsackie-adenovirus receptor is colocalized with integrins alpha(v)beta(3) and alpha(v)beta(5) on the cardiomyocyte sarcolemma and upregulated in dilated cardiomyopathy: implications for cardiotropic viral infections. *Circulation* 104, 275-280
95. Crowell, R. L., and Syverton, J. T. (1961) The mammalian cell-virus relationship. VI. Sustained infection of HeLa cells by Coxsackie B3 virus and effect on superinfection. *J Exp Med* 113, 419-435
96. Carthy, C. M., Granville, D. J., Watson, K. A., Anderson, D. R., Wilson, J. E., Yang, D., Hunt, D. W. C., and McManus, B. M. (1998) Caspase Activation and Specific Cleavage of Substrates after Coxsackievirus B3-Induced Cytopathic Effect in HeLa Cells. *J. Virol.* 72, 7669-7675
97. Chow, L. H., Gauntt, C. J., and McManus, B. M. (1991) Differential effects of myocarditic variants of Coxsackievirus B3 in inbred mice. A pathologic characterization of heart tissue damage. *Lab. Invest.* 64, 55-64

98. Kühl, U., Pauschinger, M., Schwimmbeck, P. L., Seeberg, B., Lober, C., Noutsias, M., Poller, W., and Schultheiss, H.-P. (2003) Interferon-β Treatment Eliminates Cardiotropic Viruses and Improves Left Ventricular Function in Patients With Myocardial Persistence of Viral Genomes and Left Ventricular Dysfunction. *Circulation* 107, 2793-2798
99. Hahn, W. C., Dessain, S. K., Brooks, M. W., King, J. E., Elenbaas, B., Sabatini, D. M., DeCaprio, J. A., and Weinberg, R. A. (2002) Enumeration of the simian virus 40 early region elements necessary for human cell transformation. *Mol. Cell. Biol.* 22, 2111-2123
100. Kashimura, T., Kodama, M., Hotta, Y., Hosoya, J., Yoshida, K., Ozawa, T., Watanabe, R., Okura, Y., Kato, K., Hanawa, H., Kuwano, R., and Aizawa, Y. (2003) Spatiotemporal changes of coxsackievirus and adenovirus receptor in rat hearts during postnatal development and in cultured cardiomyocytes of neonatal rat. *Virchows Arch* 444, 283-292
101. Lamphear, B. J., Yan, R., Yang, F., Waters, D., Liebig, H. D., Klump, H., Kuechler, E., Skern, T., and Rhoads, R. E. (1993) Mapping the cleavage site in protein synthesis initiation factor eIF-4 gamma of the 2A proteases from human Coxsackievirus and rhinovirus. *Journal of Biological Chemistry* 268, 19200-19203
102. Saraste, A., Arola, A., Vuorinen, T., Kytö, V., Kallajoki, M., Pulkki, K., Voipio-Pulkki, L.-M., and Hyypiä, T. (2003) Cardiomyocyte apoptosis in experimental coxsackievirus B3 myocarditis. *Cardiovascular Pathology* 12, 255-262
103. Mukherjee, A., Morosky, S. A., Delorme-Axford, E., Dybdahl-Sissoko, N., Oberste, M. S., Wang, T., and Coyne, C. B. (2011) The coxsackievirus B 3C protease cleaves MAVS and TRIF to attenuate host type I interferon and apoptotic signaling. *PLoS Pathog* 7, e1001311
104. Heim, A., Canu, A., Kirschner, P., Simon, T., Mall, G., Hofschneider, P. H., and Kandolf, R. (1992) Synergistic interaction of interferon-beta and interferon-gamma in coxsackievirus B3-infected carrier cultures of human myocardial fibroblasts. *J Infect Dis* 166, 958-965
105. Schoggins, J. W., Wilson, S. J., Panis, M., Murphy, M. Y., Jones, C. T., Bieniasz, P., and Rice, C. M. (2011) A diverse range of gene products are effectors of the type I interferon antiviral response. *Nature* 472, 481-485
106. Najarro, P., Traktman, P., and Lewis, J. A. (2001) Vaccinia virus blocks gamma interferon signal transduction: viral VH1 phosphatase reverses Stat1 activation. *J. Virol.* 75, 3185-3196
107. David, M., Petricoin, E., 3rd, Benjamin, C., Pine, R., Weber, M. J., and Larner, A. C. (1995) Requirement for MAP kinase (ERK2) activity in interferon alpha- and interferon beta-stimulated gene expression through STAT proteins. *Science* 269, 1721-1723
108. Kotlyarov, A., Neininger, A., Schubert, C., Eckert, R., Birchmeier, C., Volk, H. D., and Gaestel, M. (1999) MAPKAP kinase 2 is essential for LPS-induced TNF-alpha biosynthesis. *Nat. Cell Biol.* 1, 94-97
109. Winzen, R., Kracht, M., Ritter, B., Wilhelm, A., Chen, C. Y., Shyu, A. B., Muller, M., Gaestel, M., Resch, K., and Holtmann, H. (1999) The p38 MAP kinase pathway signals for cytokine-induced mRNA stabilization via MAP kinase-activated protein kinase 2 and an AU-rich region-targeted mechanism. *EMBO J.* 18, 4969-4980
110. Valledor, A. F., Arpa, L., Sanchez-Tillo, E., Comalada, M., Casals, C., Xaus, J., Caelles, C., Lloberas, J., and Celada, A. (2008) IFN-{gamma}-mediated inhibition of MAPK phosphatase expression results in prolonged MAPK activity in response to M-CSF and inhibition of proliferation. *Blood* 112, 3274-3282
111. Kim, S. M., Park, J. H., Chung, S. K., Kim, J. Y., Hwang, H. Y., Chung, K. C., Jo, I., Park, S. I., and Nam, J. H. (2004) Coxsackievirus B3 infection induces cyr61 activation via JNK to mediate cell death. *J. Virol.* 78, 13479-13488

112. Bain, J., McLauchlan, H., Elliott, M., and Cohen, P. (2003) The specificities of protein kinase inhibitors: an update. *Biochem. J.* 371, 199-204
113. Zhang, T., Inesta-Vaquera, F., Niepel, M., Zhang, J., Ficarro, S. B., Machleidt, T., Xie, T., Marto, J. A., Kim, N., Sim, T., Laughlin, J. D., Park, H., LoGrasso, P. V., Patricelli, M., Nomanbhoy, T. K., Sorger, P. K., Alessi, D. R., and Gray, N. S. (2012) Discovery of potent and selective covalent inhibitors of JNK. *Chem Biol* 19, 140-154
114. Goentoro, L., and Kirschner, M. W. (2009) Evidence that fold-change, and not absolute level, of beta-catenin dictates Wnt signaling. *Mol. Cell* 36, 872-884
115. Janes, K. A., Reinhardt, H. C., and Yaffe, M. B. (2008) Cytokine-induced signaling networks prioritize dynamic range over signal strength. *Cell* 135, 343-354
116. Lee, R. E., Walker, S. R., Savery, K., Frank, D. A., and Gaudet, S. (2014) Fold change of nuclear NF-kappaB determines TNF-induced transcription in single cells. *Mol. Cell* 53, 867-879
117. Nakakuki, T., Birtwistle, M. R., Saeki, Y., Yumoto, N., Ide, K., Nagashima, T., Brusch, L., Ogunnaike, B. A., Okada-Hatakeyama, M., and Kholodenko, B. N. (2010) Ligand-specific c-Fos expression emerges from the spatiotemporal control of ErbB network dynamics. *Cell* 141, 884-896
118. Swameye, I., Muller, T. G., Timmer, J., Sandra, O., and Klingmuller, U. (2003) Identification of nucleocytoplasmic cycling as a remote sensor in cellular signaling by databased modeling. *Proc. Natl. Acad. Sci. U.S.A.* 100, 1028-1033
119. Schmierer, B., Tournier, A. L., Bates, P. A., and Hill, C. S. (2008) Mathematical modeling identifies Smad nucleocytoplasmic shuttling as a dynamic signal-interpreting system. *Proc. Natl. Acad. Sci. U.S.A.* 105, 6608-6613
120. Chitforoushzadeh, Z., Ye, Z., Sheng, Z., LaRue, S., Fry, R. C., Lauffenburger, D. A., and Janes, K. A. (2016) TNF-insulin crosstalk at the transcription factor GATA6 is revealed by a model that links signaling and transcriptomic data tensors. *Sci Signal* 9, ra59
121. Albeck, J. G., MacBeath, G., White, F. M., Sorger, P. K., Lauffenburger, D. A., and Gaudet, S. (2006) Collecting and organizing systematic sets of protein data. *Nat. Rev. Mol. Cell Biol.* 7, 803-812
122. Liu, C.-W., Li, X., Thompson, D., Wooding, K., Chang, T.-l., Tang, Z., Yu, H., Thomas, P. J., and DeMartino, G. N. (2006) ATP binding and ATP hydrolysis play distinct roles in the function of 26S proteasome. *Mol. Cell* 24, 39-50
123. Cruz, L. A. B., Hebly, M., Duong, G.-H., Wahl, S. A., Pronk, J. T., Heijnen, J. J., Daran-Lapujade, P., and van Gulik, W. M. (2012) Similar temperature dependencies of glycolytic enzymes: an evolutionary adaptation to temperature dynamics? *BMC Syst Biol* 6, 151
124. Andreassen, P. R., Lacroix, F. B., Villa-Moruzzi, E., and Margolis, R. L. (1998) Differential subcellular localization of protein phosphatase-1 alpha, gamma1, and delta isoforms during both interphase and mitosis in mammalian cells. *J. Cell Biol.* 141, 1207-1215
125. Bordería, A. V., Isakov, O., Moratorio, G., Henningsson, R., Agüera-González, S., Organtini, L., Gnädig, N. F., Blanc, H., Alcover, A., Hafenstein, S., Fontes, M., Shomron, N., and Vignuzzi, M. (2015) Group Selection and Contribution of Minority Variants during Virus Adaptation Determines Virus Fitness and Phenotype. *PLoS Pathog.* 11, e1004838
126. Zhang, Q.-M., Song, W.-Q., Li, Y.-J., Qian, J., Zhai, A.-X., Wu, J., Li, A.-M., He, J.-M., Zhao, J.-Y., Yu, X., Wei, L.-L., and Zhang, F.-M. (2012) Over-expression of mitochondrial antiviral signaling protein inhibits coxsackievirus B3 infection by enhancing type-I interferons production. *Virol. J.* 9, 312

127. Janes, K. A., Albeck, J. G., Peng, L. X., Sorger, P. K., Lauffenburger, D. A., and Yaffe, M. B. (2003) A high-throughput quantitative multiplex kinase assay for monitoring information flow in signaling networks: application to sepsis-apoptosis. *Mol. Cell. Proteomics* 2, 463-473
128. Gaudet, S., Janes, K. A., Albeck, J. G., Pace, E. A., Lauffenburger, D. A., and Sorger, P. K. (2005) A Compendium of Signals and Responses Triggered by Prodeath and Prosurvival Cytokines. *Mol. Cell. Proteomics* 4, 1569-1590
129. Jadwin, J. A., Oh, D., Curran, T. G., Ogiue-Ikeda, M., Jia, L., White, F. M., Machida, K., Yu, J., and Mayer, B. J. (2016) Time-resolved multimodal analysis of Src Homology 2 (SH2) domain binding in signaling by receptor tyrosine kinases. *Elife* 5, e11835
130. Blom, N., Hansen, J., Blaas, D., and Brunak, S. (1996) Cleavage site analysis in picornaviral polyproteins: discovering cellular targets by neural networks. *Protein Sci.* 5, 2203-2216
131. Jullien, P., Bougeret, C., Camoin, L., Bodeus, M., Durand, H., Disanto, J. P., Fischer, S., and Benarous, R. (1994) Tyr394 and Tyr505 are autophosphorylated in recombinant Lck protein-tyrosine kinase expressed in Escherichia coli. *Eur. J. Biochem.* 224, 589-596
132. Seeliger, M. A., Young, M., Henderson, M. N., Pellicena, P., King, D. S., Falick, A. M., and Kuriyan, J. (2005) High yield bacterial expression of active c-Abl and c-Src tyrosine kinases. *Protein Sci.* 14, 3135-3139
133. Bozym, R. A., Morosky, S. A., Kim, K. S., Cherry, S., and Coyne, C. B. (2010) Release of intracellular calcium stores facilitates coxsackievirus entry into polarized endothelial cells. *PLoS Pathog.* 6, e1001135
134. Huber, S. A., and Rincon, M. (2008) Coxsackievirus B3 induction of NFAT: requirement for myocarditis susceptibility. *Virology* 381, 155-160
135. Esfandiarei, M., and McManus, B. M. (2008) Molecular biology and pathogenesis of viral myocarditis. *Annu. Rev. Pathol.* 3, 127-155
136. Qin, M., Escuadro, B., Dohadwala, M., Sharma, S., and Batra, R. K. (2004) A novel role for the coxsackie adenovirus receptor in mediating tumor formation by lung cancer cells. *Cancer Res.* 64, 6377-6380
137. Miyamoto, S., Inoue, H., Nakamura, T., Yamada, M., Sakamoto, C., Urata, Y., Okazaki, T., Marumoto, T., Takahashi, A., Takayama, K., Nakanishi, Y., Shimizu, H., and Tani, K. (2012) Coxsackievirus B3 is an oncolytic virus with immunostimulatory properties that is active against lung adenocarcinoma. *Cancer Res.* 72, 2609-2621

Supplemental references

1. Bose, A. K., and Janes, K. A. (2013) A high-throughput assay for phosphoprotein-specific phosphatase activity in cellular extracts. *Mol. Cell. Proteomics* 12, 797-806
2. Schoggins, J. W., Wilson, S. J., Panis, M., Murphy, M. Y., Jones, C. T., Bieniasz, P., and Rice, C. M. (2011) A diverse range of gene products are effectors of the type I interferon antiviral response. *Nature* 472, 481-485
3. Halees, A. S., El-Badrawi, R., and Khabar, K. S. (2008) ARED Organism: expansion of ARED reveals AU-rich element cluster variations between human and mouse. *Nucleic Acids Res.* 36, D137-140

Chapter 3:

Transcriptomic and Phosphatase Regulatory Adaptations Determine Stimulus-Induced Cytokine Secretion in Cardiomyocytes Chronically Expressing Coxsackievirus B3

Millie Shah, Cheryl Borgman, and Kevin A. Janes

Department of Biomedical Engineering, University of Virginia, Charlottesville, VA 22908

3.1. Introduction

Persistent viral infection fundamentally alters tissue function. In the heart, persistent infection by positive-strand RNA virus coxsackievirus B3 (CVB3) is characterized by diffuse, low-level myocardial expression of viral genome (1, 2). CVB3 expression is not accompanied by lytic release of viral progeny. Instead, myocardial lesions occur as a result of prolonged inflammation (3, 4), leading to dilation and weakening of the heart known as dilated cardiomyopathy (DCM) (1, 5). Clinical studies have shown that cardiotropic viral RNA clearance through antiviral cytokine treatment leads to restored cardiac function and elimination of inflammation (6). This suggests that chronic viral genome expression may have a role in maintaining tissue inflammation through intracellular host-pathogen interactions.

In this study, we seek to understand chronic CVB3 disruption of host signaling networks. From in vitro acute infection experiments, we know that CVB3 perturbs several pathways in host signal processing. Previous work has shown hyperactivation of ERK pathway through direct viral protease cleavage of Ras-GAP and indirect activation of stress responsive pathways p38 and JNK (7-9). Network-level studies have been able to link these and other signaling perturbations to downstream consequences like viral life cycle progression and autocrine feedback mechanisms (10, 11). Such high-throughput studies have uncovered new signaling network topologies and viral modulation of cellular behavior in acute infection but have not been applied to chronic disease.

Linking host-pathogen interactions to inflammatory processes has been elusive in vivo. Mouse models of CVB3 infection accurately recapitulate human disease, including susceptibility and progression to chronic infection (12). Several studies have documented disease-associated changes in cardiac tissue architecture and function as well as immune cell infiltration (3, 13, 14). Taken together, it is clear that prolonged expression of proinflammatory cytokines plays a key role in chronic pathology (4, 15-17). These studies, however, cannot assess infected cardiomyocyte regulation of inflammation due to a lack of scalability.

Cell-based models are uniquely amenable to intracellular systems-level studies but chronic infection is difficult to establish in vitro. Models of persistent infection in immortalized cell lines manifest as prolonged viral infection-replication cycles, resulting in high viral titers not reflective of clinical data (18, 19). Neonatal rat primary cells expressing packaging deficient CVB3 have shown direct cytopathic effects of viral expression but have limited lifespan in culture (20). We address these hurdles by engineering immortalized AC16 cardiomyocytes stably expressing packaging deficient CVB3 at very low levels. This model system not only facilitates cataloging of transcriptomic changes but also allows us to delineate the contribution of infected myocytes to the inflammatory milieu. Further, this cell-based model is ideal for quantifying CVB3-mediated enzymatic alterations in signaling pathways.

An enzyme class of particular interest are protein phosphatases (PPase). PPases negatively regulate target substrate activity by removing activating phosphate groups. Because of their broad specificity, PPases coordinate signaling responses throughout the cell and are particularly important in response to stimulation. Theoretical studies have shown that inhibition of PPases can alter the amplitude and duration of stimulated pathways (21). It follows that prolonged dysregulation may result in changes to baseline pathway output. We have previously shown that PPase responses to interferon treatment are perturbed in the context of acute CVB3 infection; uncovering a role for JNK phosphatases in the Type I antiviral response (22). In this study we seek to understand how phosphatase regulation changes during chronic CVB3 infection and investigate downstream consequences for cytokine production.

Using our in vitro model of CVB3 infection, we find that phosphatase regulation is altered in cell lines chronically expressing CVB3 both at baseline and with stimulation. Baseline increases in phosphatase activity indicate dampening of MK2 pathway activity and correspond to lower baseline IL6 production. Further, we show that stimulus-mediated increases in phosphatase activity correspond to lowered proinflammatory cytokine production in infected cells. Taken together, this work suggests that chronic CVB3 infection initiates both transcriptomic and signaling adaptations which together influence infected cardiomyocyte crosstalk with the inflammatory milieu.

3.2 Results

Engineering AC16 cardiomyocyte model of chronic infection in vitro

To assess intracellular signaling alterations during chronic CVB3 infection, we first engineered an AC16 cardiomyocyte model of human disease. AC16 cells were generated by Davidson et al 2005 through the fusion of SV40 T-antigen transformed human fibroblasts and human primary cardiomyocytes (23). They retain expression of several cardiomyocyte markers including GATA4, MYCD, desmin, BNP, and gap junction connexins. Quiescence can be induced in these cells through short hairpin RNA (shRNA) knockdown of SV40 T-antigen. Upon proliferation arrest (Figure S1 B&C), AC16 cells elongate (Figure S1A) and form multinucleated syncytia characteristic of cardiomyocytes. Additionally, quiescent AC16 cells upregulate BMP2, a transcription factor important for cardiac development (24-26). We have previously shown that AC16 cells are permissive to acute infection upon reconstitution of CVB3 cognate receptor and display canonical downstream sequelae of intracellular viral replication (22). These data support that AC16 cardiomyocytes are a suitable cellular model for human chronic CVB3 infection.

Prolonged, low-level CVB3 genome expression without viral progeny release are key characteristics of chronic infection. To accomplish this in vitro, we delivered packaging deficient CVB3 (CVB3ΔVP0) to AC16 cardiomyocytes as a cDNA construct (Figure S1D). To preclude viral progeny release, this construct was mutated at the viral protease cleavage site between VP2 and VP4 capsid proteins (see Experimental Procedures for details). Without four mature capsid proteins, CVB3 transcripts cannot be packaged into new virions. The remaining sequence of the CVB3 construct is unaltered allowing for maturation of seven non-structural proteins important for viral replication and host-pathogen interactions. Because CVB3 is a non-integrating single stranded RNA virus, the molecular underpinnings of prolonged expression in the heart in unclear (27, 28). In this model system,

integrated CVB3 cDNA serves as a constant source of viral RNA and protein to offset intracellular degradation. Low-level expression is achieved through a leaky tet-tight promoter to prevent overwhelming cytopathic effects seen in previous studies where CVB3ΔVP0 expression is driven by a strong CMV promoter (20). Furthermore, infection of permissive cells with virions carrying CVB3ΔVP0 genome yielded responses highly consistent with wild-type CVB3 infection suggesting that this method only captures early-stage responses to viral genome delivery (Chapter 5).

Integration of CVB3ΔVP0 cDNA was achieved through lipofection of linearized pSLIK-TT-CVB3ΔVP0-Hygro plasmid (Figure 1A). A control cell line was engineered in the same way through delivery of linearized pSLIK-TT-Luciferase-Hygro. Free DNA ends of the construct should initiate DNA repair processes and encourage integration of the construct into the AC16 genome. Stable integrants were selected for with hygromycin antibiotic and single-cell clonal cell lines were established through limiting dilution (Figure 1A). Clonal cell lines ensure that population level measurements are not confounded by a pool of hetergenous integrants. Twelve clonal cell lines and a polyclonal control cell line (AC16-Luc) that maintained AC16 growth properties and capability for quiescence induction were chosen for further analysis (data not shown). Lack of viral progeny was confirmed by plaque assay for all 12 clones and control AC16-Luc (Figure 1B, representative images).

Construct integration and expression was assessed through RNA-seq of quiescent cell lines. Hygromycin expression was considered a readout of construct integration and varied between cell lines. Similarly, CVB3 expression varied between clones but did not necessarily correlate with hygromycin expression (Figure 1C). AC16-Luc cells, which do not express CVB3, displayed minimal read alignment to the viral genome (< 3 reads on average) and set the threshold for detectable CVB3 expression. Variability in the CVB3 to hygromycin ratio suggests host modulation of CVB3 expression.

Clonal adaptations to chronic CVB3 expression

To investigate possible clonal adaptations to viral genome expression, we assessed transcriptomic differences by RNA-seq analysis (see Experimental Procedures for details). We quantified clonal differential gene expression relative to our AC16-Luc control cells. Between 500 and 2600 genes were significantly altered by at least 1.5 -fold in each of the CVB3ΔVP0 cell lines. However, only 8 of these were consistently changed in all cell lines. Two of these genes, TNFa receptor TNFRSF1B (TNFR2) and its downstream transducer BIRC3 are downregulated (29). There are two major TNFα receptors expressed by most cells types, TNFR1 and TNFR2. While TNFR2 is known to be anti-apoptotic and cytoprotective in the heart, TNFR1 promotes proinflammatory cytokine production and apoptosis (30-32). Downregulated TNFR2 may shift cellular TNFα stimulated signaling to the proinflammatory TNFR1 cascade. Given that TNFα is documented to be elevated in clinical samples and mouse models, this may be involved in the maintenance of inflammation during chronic infection (4, 15, 33).

We next assessed clone-specific adaptations to CVB3 expression. Taking the top 100 most variable differentially expressed genes, we conducted principal component analysis (PCA) to see if groups of clones showed similar transcriptomic signatures (Figure 1D). PCA projection segregated the clones into three different quadrants. We visually evaluated differential expression and found each clone cluster could be characterized by distinct transcript groups (Figure 1E, colored boxes). Group A is likely distinguished from Group B because of increased downregulation of genes within the yellow box (Figure 1E). Gene-set enrichment of differentially expressed transcripts within each cluster showed that Group A and B clones are enriched for downregulated TNF pathway genes while Group C clones are enriched for upregulation of anti-viral and interferon genes (Figure 1E and Supplemental Table 1). Consistent with these transcriptomic signatures, we find that Group A and B clones have higher relative CVB3 expression on average compared to Group C clones (Figure S2A). Taken together, these different clonal adaptations may represent an array of responses to chronic CVB3 infection, modeling the pathological diversity observed in humans and mice (34-36).

Quantification of cellular responses to inflammatory and antiviral stimuli

Because the inflammatory context is a key player in chronic CVB3 infection, we sought to determine cardiomyocyte contribution to the inflammatory milieu. To accomplish this, we first defined a set of clinically relevant stimuli (inputs) and secreted cytokines (outputs). For inputs we chose proinflammatory cytokines TNFα and IL1β, and antiviral factors IFNβ and IFNγ. TNFα and IL1β have been implicated as detrimental in many inflammatory heart conditions including CVB3 infection. By contrast, IFNβ and IFNγ have shown efficacy in treatment of chronic CVB3 (6, 37, 38). For outputs we chose molecules known to be induced by our inputs; specifically, chemotactic factors CCL2 (39), IP10 (40), and MIP1α (41) as well as IL6 (42, 43). All of these cytokines modulate proinflammatory responses and IL6 specifically is important in acute CVB3 infection (44-50).

Input-output relationships between these factors are determined by intracellular signal transduction. For this study we focus on ERK, p38-MK2, JNK, CREB, and STAT1 signaling cascades. ERK and CREB pathways are known to be directly modified by CVB3 proteases (7, 51). Stress-responsive pathways p38-MK2 and JNK are independently activated during acute infection (8, 9), perhaps through autocrine signals like TNFα and IL1β. Similarly, STAT1 is activated downstream of interferon sensing (52). Transcriptional activation resultant from these pathways are important for cytokine production. We did not detect baseline protein activation or abundance alterations in these pathways in any of the 12 clonal cells lines (Figure S2B), suggesting that without stimulation signaling capacity in each cell line is relatively unchanged

Transmission of extracellular signals can be negatively modulated by protein phosphatases. In fact, we have shown that regulated changes in phosphatase activity can affect how extracellular cues are interpreted and responded to (22, 53). Furthermore, there is evidence that CVB3 proteins directly alter phosphatase activity (54, 55). Thus, we next wanted to evaluate the relationship between phosphatases and cytokine release. To measure phosphatase activity against our proteins of interest,

we used our previously published high-throughput phosphatase activity assays (22). Briefly, these assays measure substrate-specific phosphatase activity in cellular extracts using an ELISA format. Endogenous phosphatases can be extracted from adherent cells lines using our subcellular fractionation technique. This method yields extracts from two cellular compartments: saponin-extractable (SE) fraction, which contains cytoplasmic and low molecular weight nuclear proteins, and NP-40 extractable (NE) fraction, which includes nuclear and transmembrane proteins.

For these phosphatase activity and cytokine release studies we chose representative clones from each cluster (Figure 1D, colored points) and induced quiescence via SV40 T-antigen knockdown. We find that at baseline, there are mostly mild changes in phosphatase activity compared to AC16-Luc control cells (Figure 2A). One consistent change among the selected clones was an increase in SE phosphatase activity towards MK2 threonine 334 (T334) phosphorylation site. When threonine 334 is dephosphorylated, MK2 is shuttled to nucleus preventing it from carrying out downstream cytoplasmic functions (56-58). This suggests that even at baseline, these clonal cell lines dampen sporadic MK2 pathway activity. In parallel, we also measured baseline cytokine secretion and found that CCL2, IL6, and MIP1α are downregulated in our chronic cell lines compared to AC16-Luc control (Figure 2B). Interestingly, cytoplasmic MK2 is involved in the stabilization of IL6 mRNA (59-61). Thus, increased SE MK2 phosphatase activity is consistent with the observed decrease in IL6 secretion.

Next, we measured stimulated phosphatase responses to determine if CVB3 infection alters phosphatase regulation. Quiescent clonal cell lines and AC16-Luc control were treated with saturating doses (Figure S3) of a single input stimulus, TNFα, IL1β, IFNγ or IFNβ, for two hours before extraction of endogenous phosphatases. Overall, we found that each clonal cell line had a distinct phosphatase activation pattern (Figure 3A). In control cells, the response pattern is dominated by decreased SE ERK, JNK, and CREB phosphatase activity. The A1 clone displayed phosphatase responses similar to control cells with the exception of the TNFα response. By contrast, the B1 cell line increased phosphatase activity with stimulation overall while the C1 clone was unresponsive. This suggests that

CVB3 expression itself may not directly affect phosphatase activity but rather, transcriptomic adaptions to CVB3, like the interferon antiviral program, may globally disrupt phosphatase responsiveness.

We further performed cytokine ELISAs to determine if stimulated phosphatase activity patterns corresponded with cytokine release. We assayed conditioned media from quiescent clones after 24 hours of stimulation. In all cell lines, including control, we found strong induction of IP10 with interferon stimulation as expected (Figure 3B). Unlike control cells, both A1 and C1 cells produced CCL2, IL6, IP10 and MIP1α in response to IL1β and TNFα stimulation (Figure 3B 2nd and bottom panels). By contrast, B1 cells only induced IL6 with these stimuli (Figure 3B, 3rd panel). Taken together, this suggests that CVB3 infection results in increased proinflammatory cytokine production in cells that either have no phosphatase adaption (A1) or have globally unresponsive phosphatase (C1). Cytokine production is, however, decreased in CVB3-expressing B1 cells where phosphatase activity is increased in response to stimulation. It follows that increased phosphatase activity likely dampens stimulus-driven pathway activity and may prevent cytokine gene induction.

Predicting direct phosphatase activity to cytokine release relationships is difficult to do in this large dataset through visual inspection. Instead, we can use statistical modeling to make inferences about the data in a formalized way. We have reviewed different statistical modeling techniques in Chapter 5 of this dissertation. Wherein we use partial least squares regression (PLSR) to predict viral protein expression and cell death from signaling protein phosphorylation levels. PLSR is similar to PCA in that it projects the data into a new, lower dimensional space defined by principal components. Unlike PCA, PLSR uses linear regression to project a predictor data set and an output data set onto the same principal components. This new projection seeks to capture the maximum covariance in the predictor and output data sets. Thus, similar projections of predictor and output data points indicate covariation in those points and suggests that there may be an underlying causal link between that predictor and output. More on the mathematical formalisms can be found in Chapter 5.

To investigate phosphatase activity – cytokine release relationships, we first arranged our predictor (phosphatase) and output (cytokine) data in a way that was compatible with PLSR (Figure

4A). Then, using plsregress in Matlab, we made models comprised of 1 to 11 principal components. For each model we assessed how much variance in each data set was captured and how stable the model was (Figure 4B&C). Model stability was quantified as mean squared error (MSE) of four-fold cross validation (see methods for details). For our PLSR model we chose three components because this allowed us to capture the most variance in both data sets while minimizing the MSE (Figure 4B&C, grey dashed line).

This three component model captured ~50% of the variance in both the predictor and output data. Model predictions are plotted against experimental measurements in Figure 4D. Plotting the new projections of the data in each principal component pair, we find that IP10 is not strongly associated with any other outputs or phosphatase assays (Figure 4E). However, CCL2, MIP1α, and IL6 are clustered near each other in all PC mappings likely because they are covarying with TNFα and IL1β treatment in both A1 and C1 cell lines and to a lesser extent in B1 (Figure 3B). In each principal component biplot these cytokines are associated with different predictors, yet, these phosphatase activities are either not changed or inconsistently changed between different cell lines with respect to their CCL2, MIP1α, and IL6 expression. For example, in the PC1 vs PC2 plot we find close association with P38 NE and JNK NE activity (Figure 4E, bold boxed). Upon inspection of the phosphatase data (Figure 3A) we find that the P38 NE phosphatase activity only has a consistent change with respect to IL6 expression in the B1 cell line (Figure 3A 3rd panel). Furthermore, JNK NE phosphatase activity has an anti-correlated response with CCL2, IL6, and MIP1α only in A1 (Figure 3A 2nd panel). Neither of these phosphatase activities correspond to upregulation of these cytokines in the C1 cell line. Once again, this suggests that there may be underlying rewiring of phosphatase regulation related to different transcriptomic adaptations thus preventing the model from extracting phosphatase-cytokine relationships that are true across all cell lines. Indeed, the model seems to be predicting changes for conditions where no change was observed (Figure 4D, data points smeared along x-axis). Reinforcing

the idea that rewired phosphatase responses in some cell lines abrogate the expected phosphatase – cytokine link.

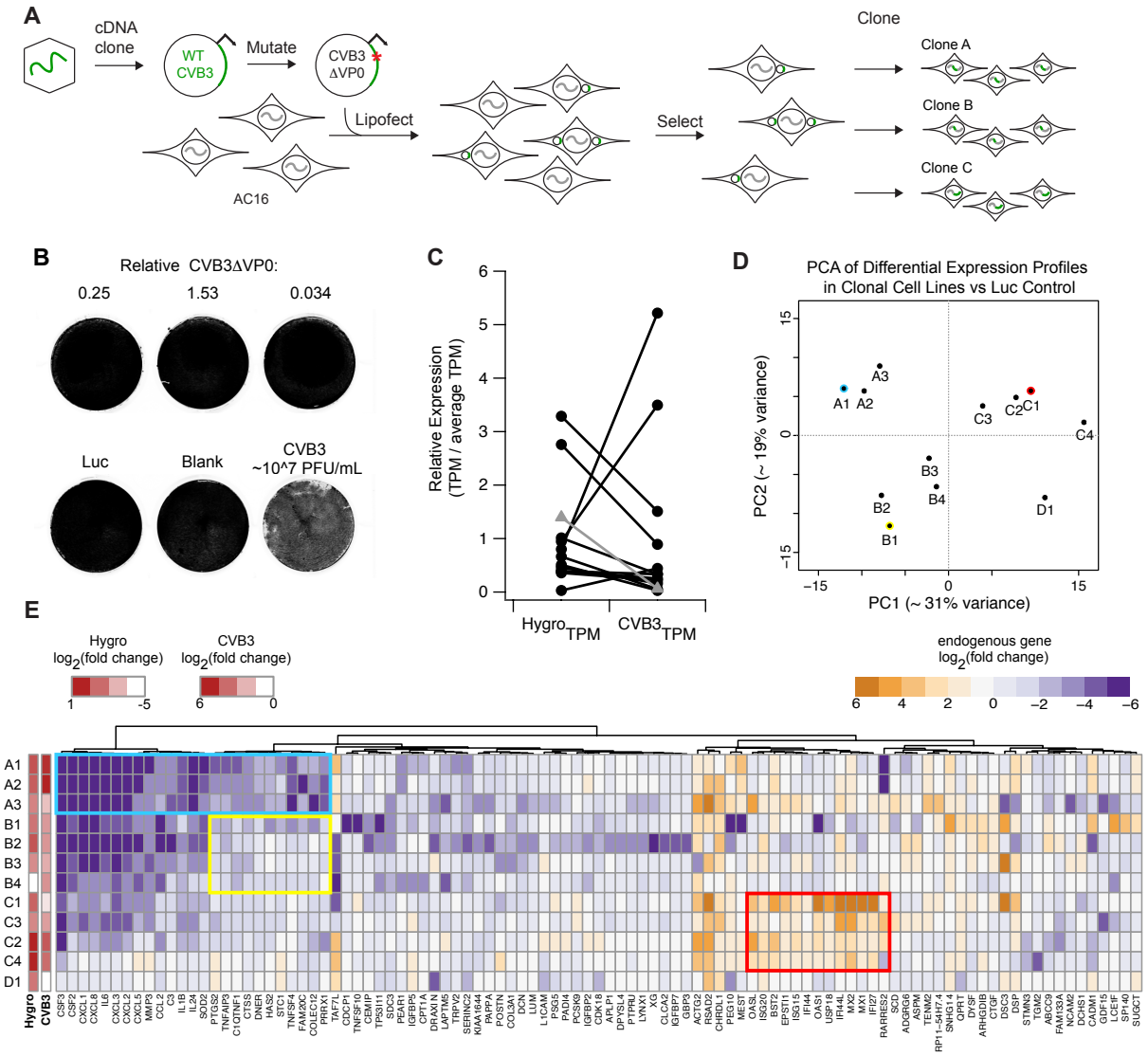

Figure 1. AC16 Clonal Cell Line Model of Chronic CVB3 Infection

A. Cellular engineering of AC16 expressing pSLIK-TT-CVB3ΔVP0-Hygro cell lines. B. Representative plaque assay of CVB3ΔVP0 clonal cell line conditioned media. Live CVB3 virus at ~10^7 PFU/mL was added as a positive control, resulting in clearance of the HeLa monolayer (grey well). Media from all clonal cell lines as well as Luc control and blank media left intact HeLa monolayers indicating no virion production (black wells). C. Hygro and CVB3 relative transcripts per million. CVB3ΔVP0 cell lines (black circles), AC16-Luc control (grey triangles). D. Principal component analysis (PCA) of top 100 most variable differentially expressed genes as determined through RNA sequencing. Differential expression compared to AC16 pSLIK-TT-Luciferase-Hygro expressing cells was determined through DESeq2 R package. See methods for details. Representative clones from each PCA defined cluster are highlighted in blue, yellow, and red. These colors correspond to the genes outlined in E. E. Heat map of top 100 most variable differentially expressed genes. CVB3 and Hygro expression is shown in leftmost offset columns (white to red color scale); CVB3 $\log_2$(fold change) = 0 indicates background level detection. Clusters of genes representing PCA-defined cell line clusters are outline in colored boxes (cyan, yellow, and red).

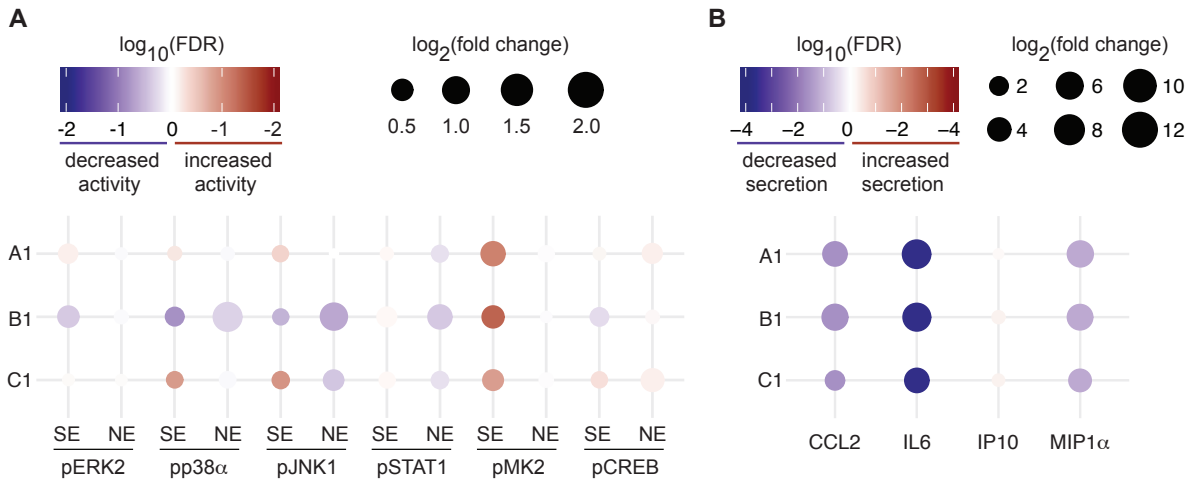

Figure 2. PPase activity and cytokine secretion are altered in CVB3ΔVP0 expressing clones compared to luciferase control cells at baseline

A. Phosphatase activity was assessed in three representative CVB3ΔVP0 cell lines and Luc control with n = 3 biological replicates for each cell line. Activity was quantified from subcellular lysate fractions as described previously (22) B. Cytokine secretion was assessed in the same three CVB3ΔVP0 cell lines and Luc control with n = 3 biological replicates. For both PPase and cytokine assays, the $\log_2$(fold change) in activity compared to Luc control cells is displayed as a circle. The size of the circle is proportional to the extent of change. The color of the circle indicates the direction of the change (blue = decreased, red = increased). The intensity of the color is proportional to the $\log_{10}$(FDR) calculated from Student's t-test and indicates the statistical significance of the change.

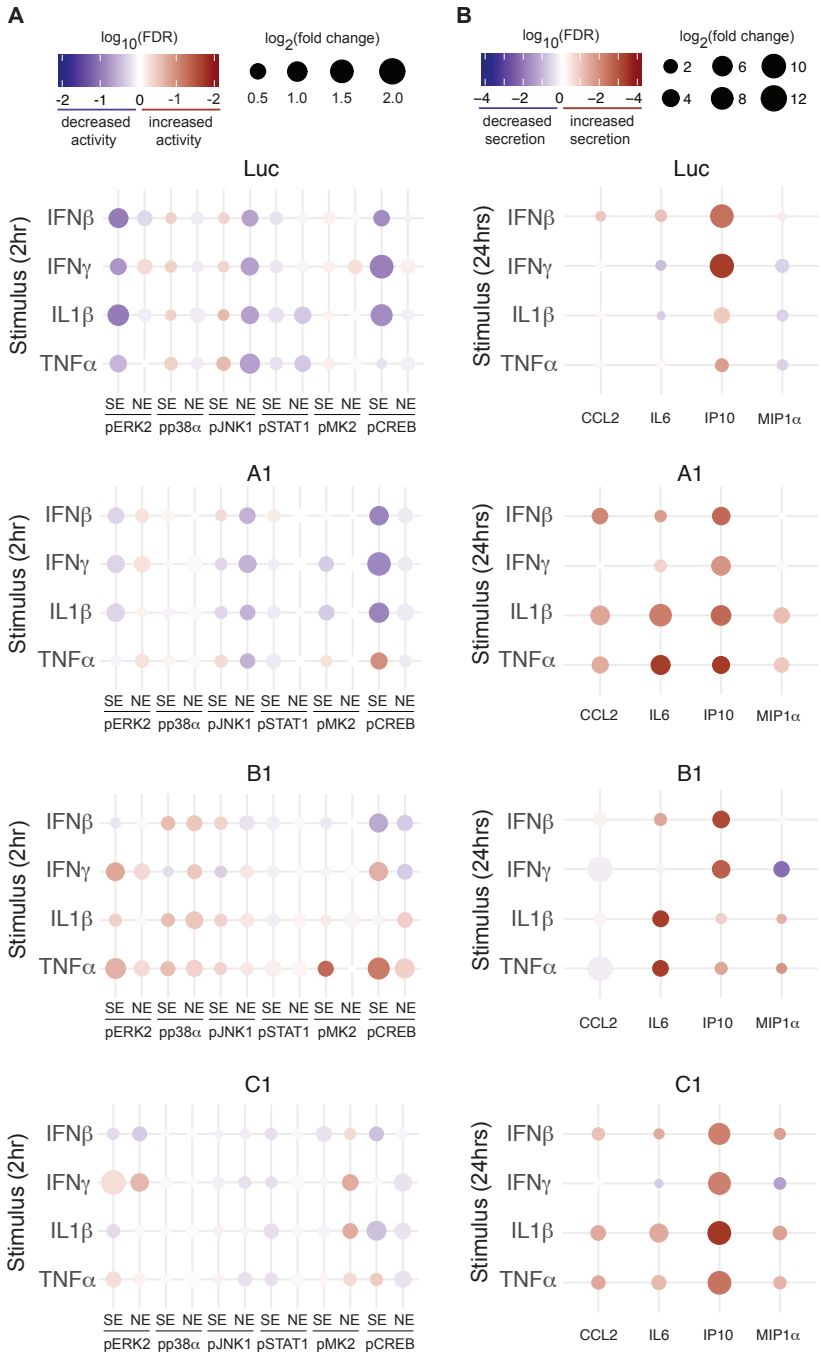

Figure 3. Inflammatory and antiviral stimulation result in altered PPase and cytokine responsiveness

A. PPase activity was quantified after 2hr stimulation with saturating amounts of the indicated stimulus. Differences from baseline ppase activity were assessed from n = 3 biological replicates for each cell line and stimulus condition. Student's t test was used to calculate p-values for each comparison which were then FDR adjusted. B. Cytokine secretion was quantified from cell culture supernatants collected 24hrs after stimulation with saturating amounts of the indicated stimulus. Differences in cytokine secretion were assessed from n = 3 biological replicates for each cell line and stimulus condition. Student's t test p-values were FDR adjusted.

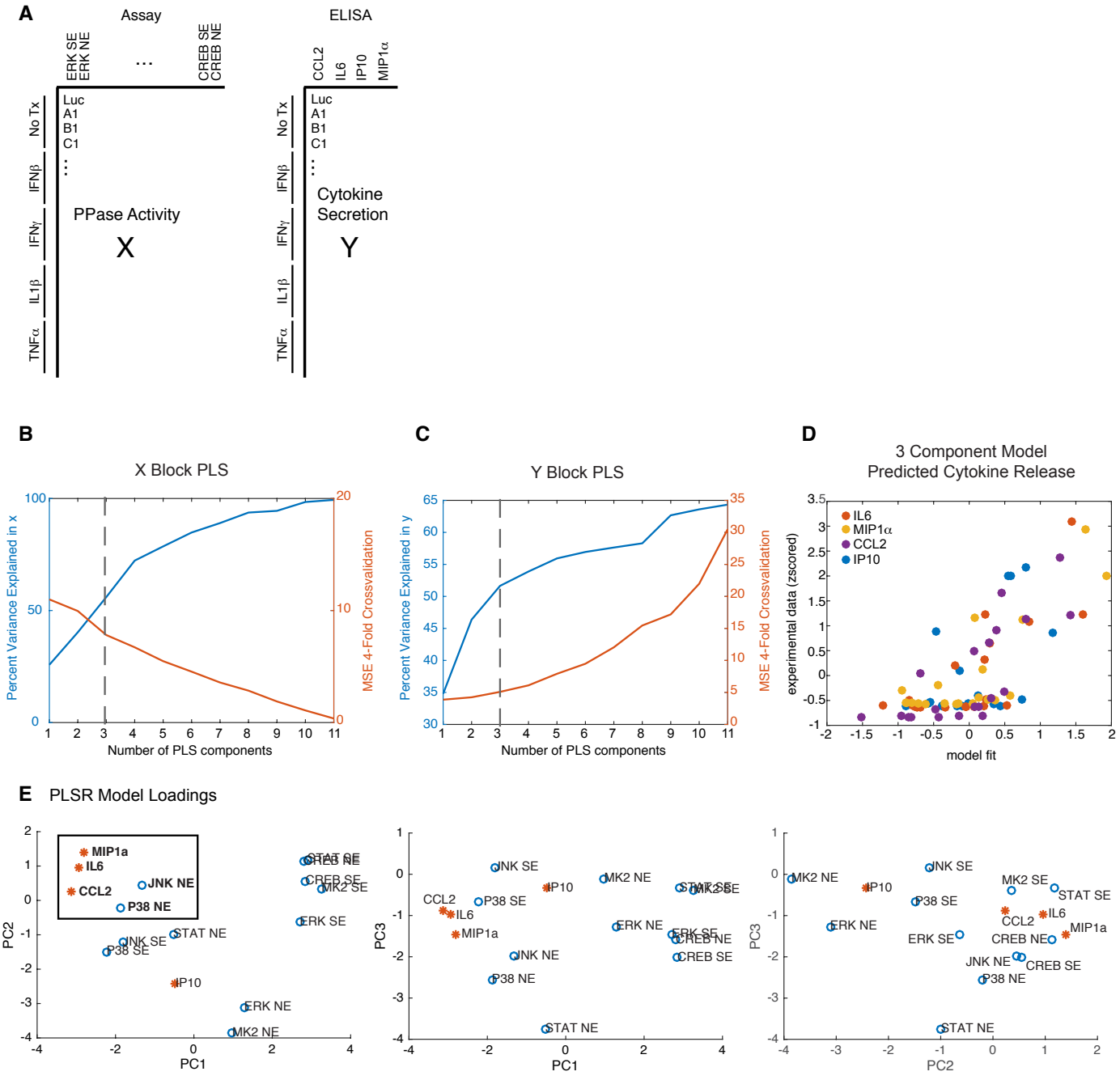

Figure 4. Phosphatase activity predicts cytokine release in cell line specific manner
A. Data configuration for partial least squares regression. X-block containing PPase data was used as predictor data while Y-block containing cytokine secretion data was used as output data. B & C Percent variance captured (blue trace) and mean-squared error (orange trace) of X (B) and Y(C) blocks from 4-fold cross-validated models. D. Ability of a three component model to predict cytokine release from PPase data. E. Principal component loadings of predictors (blue circles) and outputs (red asterisks) for each principal component pair.

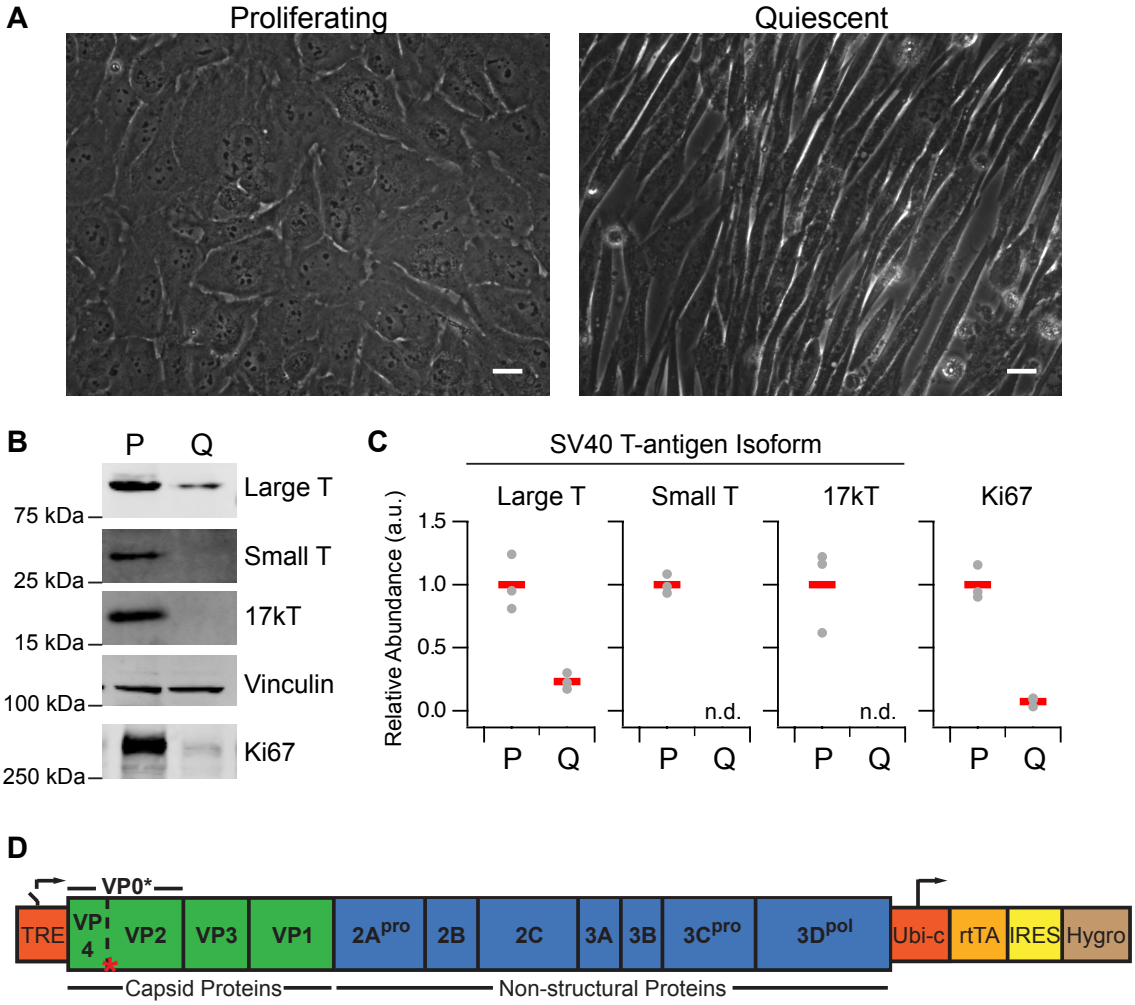

Figure S1. AC16 quiescence induction and pSLIK-TT-CVB3ΔVP0-Hygro construct schematic
A. Brightfield images of AC16 cells expressing SV40 T-antigen ("Proliferating", left image) and 48hrs after SV40 T-antigen knockdown ("Quiescent", right image). Scale bar = 40um. B. Immunoblot of transformed (P) and quiescent (Q) AC16 cells. Staining with SV40 T-antigen shows efficient knockdown of all three isoforms of SV40 T-antigen and down regulation of proliferation marker Ki67. C. Immunoblot quantification of n = 3 biological replicates. D. Schematic of construct delivered to AC16 cells. Tet-responsive element (TRE, orange) is the leaky, inducible promoter for CVB3ΔVP0 genome. CVB3 genome is mutated at a CVB3 protease site (red asterisk) to prevent maturation of VP0 into VP2 and VP4 capsid proteins. Reverse tetracycline-controlled transactivator (rtTa, light orange) and hygromycin (Hygro, brown) resistance gene are driven by a constitutive ubiquitin (Ubi-c, orange) promoter. This transcript fusion contains and internal ribosomal entry site (IRES) between the rtTa and Hygro where ribosomes can bind to translate the hygro gene.

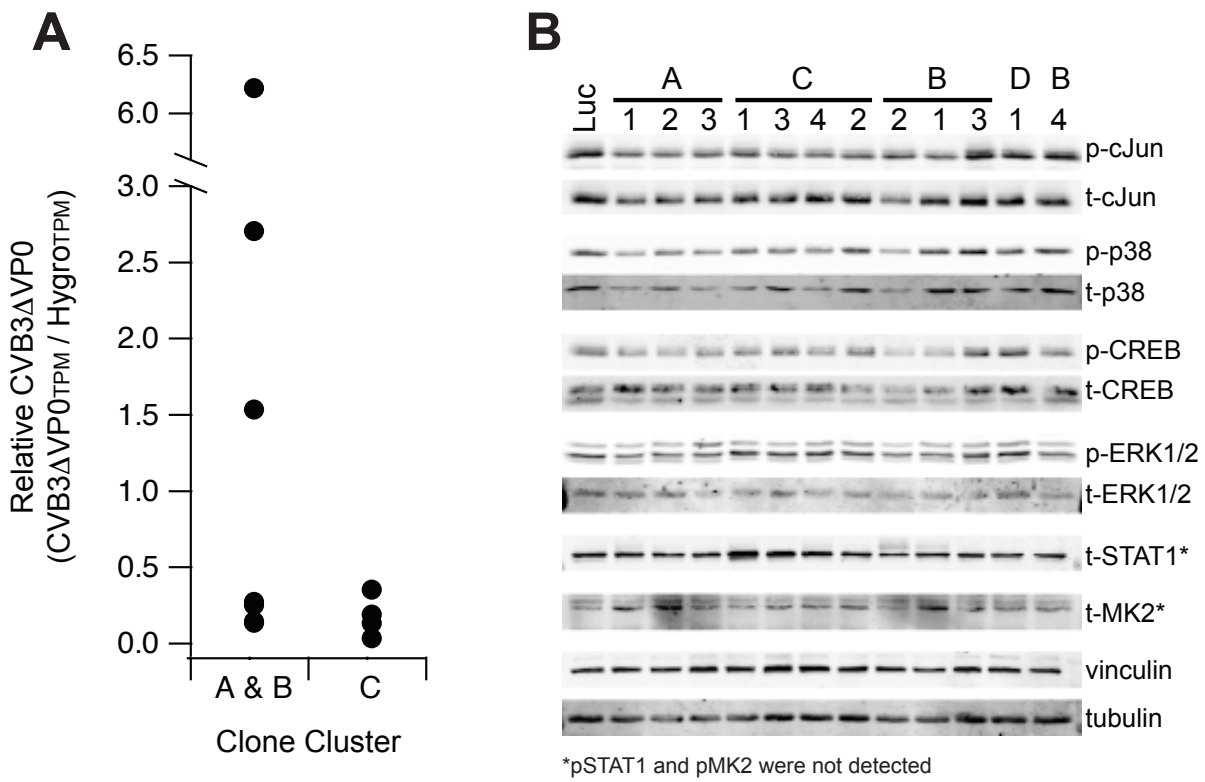

Figure S2. Clonal cell line cluster characterization
A. Relative CVB3 expression of clones in A and C clusters. Relative CVB3 was calculated as CVB3 transcripts per million (TPM) normalized to Hygromycin B TPM. B. Immunoblotting of quiescent cell line lysates to determine baseline perturbation of signaling pathways important in infection.

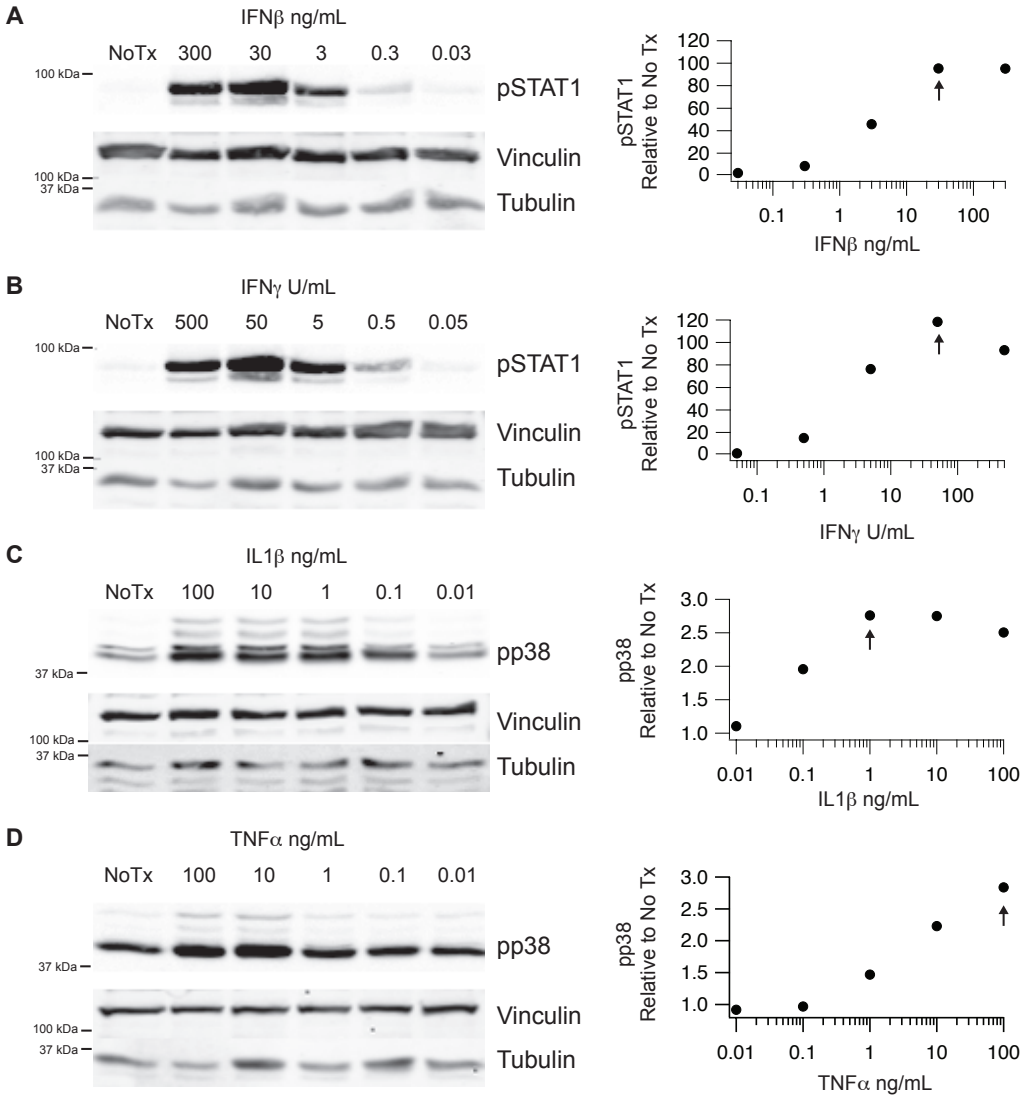

Figure S3. AC16-Luc dose response to inflammatory and antiviral stimuli
STAT1 phosphorylation in response to IFNβ (A) and IFNγ (B) treatment for 30 minutes. p38 phosphorylation in response to IL1β (C) and TNFα (D) treatment for 15 minutes. All subplots show immunoblot with loading controls vinculin and tubulin (left panels) and blot quantification (right panels). Saturating doses used for ppase and cytokine experiments are indicated by black arrows.

Table S1. GSEA of Differentially Expressed Genes in Clonal Cell Line Clusters
Gene lists were generated by filtering for genes differentially expressed by all clones in a given cluster. Differential expression was defined as at least 1.5-fold change with FDR < 0.1.

	Database	Term	DE genes (#)	% of term genes	FDR
Group A	KEGG_PATHWAY	hsa04668:TNF signaling pathway	20	4.17	4.02E-07
	GOTERM_BP_DIRECT	GO:0030198~extracellular matrix organization	22	4.58	6.39E-05
	GOTERM_BP_DIRECT	GO:0006954~inflammatory response	30	6.25	3.23E-04
	GOTERM_BP_DIRECT	GO:0071356~cellular response to tumor necrosis factor	15	3.13	1.55E-03
	GOTERM_BP_DIRECT	GO:0042060~wound healing	13	2.71	1.58E-03
Group B	KEGG_PATHWAY	hsa04668:TNF signaling pathway	15	6.70	3.91E-07
	KEGG_PATHWAY	hsa05134:Legionellosis	10	4.46	8.62E-05
	GOTERM_BP_DIRECT	GO:0006954~inflammatory response	19	8.48	1.31E-03
	GOTERM_BP_DIRECT	GO:0006955~immune response	20	8.93	1.38E-03
	GOTERM_BP_DIRECT	GO:0008284~positive regulation of cell proliferation	21	9.38	1.54E-03
Group C	GOTERM_BP_DIRECT	GO:0060337~type I interferon signaling pathway	12	12.12	5.61E-11
	GOTERM_BP_DIRECT	GO:0009615~response to virus	11	11.11	5.95E-07
	GOTERM_BP_DIRECT	GO:0045071~negative regulation of viral genome replication	7	7.07	1.07E-04
	GOTERM_BP_DIRECT	GO:0051607~defense response to virus	10	10.10	4.06E-04
	KEGG_PATHWAY	hsa05164:Influenza A	8	8.08	7.25E-02

3.3 Discussion

Chronic coxsackievirus B3 infection is known to have pleiotropic effects on cardiac intercellular inflammatory networks in vivo. In this work, we have shown that this concept extends to intracellular gene expression and signaling networks; prompting investigation into whether these micro and macro systems-level changes are causally linked through infected cell cytokine secretion. Broadly, we found that systematically increased stimulus-driven phosphatase activity dampens proinflammatory cytokine production in the context of chronic CVB3 infection.

Statistical derivations of phosphatase – cytokine relationships during chronic infection could be made in cells where phosphatase activity was altered with stimulation (A1 and B1). We predict with PLSR modeling that proinflammatory cytokine secretion in response to TNFα and IL1β are controlled by nuclear pp38 and pJNK. This is consistent with previous reports showing CCL2 dependency on these pathways (39, 62). This prediction did not hold for cells where phosphatase regulation was decoupled from stimulus inputs (C1). To extract cytokine secretion drivers in these rewired pathways it may be necessary to build adaptation specific statistical models. However, with these data, such models would be overdetermined in the predictor block because we have more observations (phosphatase assays, n = 12) than variables (stimulus conditions n = 5). Thus, this would require further data generation of different stimuli conditions. Additionally, because phosphatase activity is not changing in response to stimulation, this may indicate that kinase activation of those pathways may also be key drivers of differential cytokine expression. Thus, addition of parallel kinase activity measurements to this data set could provide non-redundant information to the statistical model. Data of this format would have three independent modes: phosphatase assays, kinase assays, and cellular condition, thus requiring the use of higher order PLSR which is reviewed in the following chapter.

3.4. Experimental Procedures:

Cloning of Packaging Deficient CVB3

CVB3 Nancy strain sequence was cloned from pCB3-M1 (63) into pcDNA3 plasmid. QuikChange mutagenesis (Agilent, Santa Clara, CA) was used to mutate nucleotides 942 (C) and 943 (T) to G in the VP0 sequence of CVB3 (20). This mutation eliminates the CVB3 protease site in VP0 and thus prevents the maturation of VP2 and VP4 capsid proteins. The mutated CVB3 cDNA sequence was then PCR cloned into pEN_TTmcs entry vector for Gateway cloning. The sequence was PCR amplified and ligated in two steps. In the first step, the 3' piece of the sequence was PCR amplified, digested with Mfe1 and EcoR1and ligated into pEN_TT digested with EcoR1. The 3' end ligation of Mfe1 and EcoR1 sites destroys the 3' EcoR1 site in the resulting pEN_TT_RHS vector leaving only the 5' EcoR1 site. In the next step, the 5' CVB3 sequence was PCR amplified, digested with EcoR1, and ligated into pEN_TT_RHS digested with EcoR1. The resulting pEN_TT_CVB3ΔVP0 was used as the donor vector for LR recombination with pSLIK-Hygro (Addgene #25737) entry vector. The resulting pSLIK-TT- CVB3ΔVP0-Hygro plasmid will be made available through Addgene.

shSV40 cloning and lentivirus preparation

The following shRNA oligosequence targeting SV40 T-antigen (uppercase) was cloned into pLKO-neo as previously described (22): ccggGCATAGAGTGTCTGCTATTAActgcagT-TAATAGCAGACACTCTATGCttttg. Lentivirus was packaged as previously described (64). Large batches of lentivirus were pooled, aliquoted, and frozen at -80°C. Each aliquot was limited to two freeze thaws before being disposed of. Hairpin efficiency was assessed by transient transduction of 293T (unpublished data) and AC16 cells (Figure S2B & C).

Cell culture and engineering

AC16 cells were cultured in DMEM/F12 media supplemented with 12.5% FBS and 1% penicillin/streptomycin at 37°C, 5% CO_2 as previously described (23).

Quiescence was induced in AC16 cells and clonal derivatives through SV40 T-antigen knockdown and nutrient alterations. Cells were plated at 100,000 cells per well on 0.02% gelatin coated tissue culture 12- well plates for 24 hours. After washing cells were refed with low serum media (LSM): DMEM/F12 media supplemented with ITS-G (ThermoFisher Scientific #41400-045), 2% horse serum and selection antibiotic if applicable. After 24 hours, cells were transduced with 125 uL shSV40 lentivirus diluted in 375 uL LSM with 8 ug/mL polybrene (Sigma #H9268), no selection antibiotics are added during this step. After 18-20 hours, cells were washed and refed with LSM containing selection antibiotics if applicable. The cells are washed and refed every 24 hours for two days. At this time cells were lysed or stimulated for further analyses.

AC16 cell lines stably expressing pSLIK-TT-CVB3ΔVP0-Hygro and control pSLIK-TT-3xFLAG-Luciferase-Hygro were engineered through transient transfection and selection with hygromycin (InvivoGen #ant-hg-5). Prior to cell delivery, plasmids were linearized by digestion with FseI enzyme for ~ 3 hours at 37C (New England BioLabs #R0588) followed by gel purification. Low passage AC16 cells were plated at 70-90% confluency in a 6-well dish overnight. The next day, cells were refed with growth media and incubated for 1 hour while DNA-liposome complexes were assembled. First, 10 uL of Lipofectamine 2000 reagent was diluted in DMEM/F12 media with 1% pen/strep and incubated for 5 minutes. 2 ug of linearized plasmid was diluted into 100 uL of DMEM/F12 media with 1% pen/strep. Diluted lipofectamine and DNA were gently mixed at a 1:1 volume ratio and DNA-liposome complexes were allowed to form for 20 minutes. Each well of the 6-well dish received 200 uL of DNA-liposome complexes and were refed with growth media after 4-6 hours. After 24 hours, cells were washed and refed with 0.5x hygromycin. After 48 hours, cells were replated into 10 cm dishes with 1x hygromycin. When small colonies of ~ 20-50 cells per colony emerged, the plate was then trypsinized and single-

cell cloned by limiting dilution. Cells stably expressing pSLIK-TT-Luciferase-Hygro were kept as a polyclonal population. All cell experiments were conducted on early passage cells (less than 10 passages from thaw).

Plaque Assay

Plaque assays were conducted as previously described (22). Conditioned media was collected from quiescent AC16 cell lines 24 hours after refeeding. Floating cells were gently spun down at 1000 g for 3 minutes and clarified supernatant was collected. Conditioned media and live virus controls were spun down at 100,000 g for 1 hour at 4°C to remove hygromycin from conditioned media samples. Spun down samples were resuspended in 200 uL of DMEM media (with 1% pen/strep) and added to HeLa monolayers for plaque assay. After 72 hours, wells were fixed and stained for viable cells with 0.5% (w/v) crystal violet. Plates were scanned on LICOR Odyssey in the 700 channel.

Immunoblotting

Immunoblotting of RIPA lysates was performed as described (65). The following primary antibodies were used:

p-cJun (Ser^{73}) (1:1000, #9164, Cell Signaling Technology, Beverly, MA)

t-cJun (1:1000, #9165, Cell Signaling Technology, Beverly, MA)

p-CREB (Ser^{133}) (1:1000, #9198, Cell Signaling Technology, Beverly, MA)

t-CREB (1:1000, #9197, Cell Signaling Technology, Beverly, MA)

p-ERK1/2 (Thr^{202}/Tyr^{204}) (1:1000, #4370, Cell Signaling Technology, Beverly, MA)

t-ERK1/2 (1:1000, #4696, Cell Signaling Technology, Beverly, MA)

Ki67 (1:1000, RM-9106-S0, ThermoFisher Scientific, USA)

p-MAPKAPK2 (Thr^{334}) (1:1000, #3007, Cell Signaling Technology, Beverly, MA)

t-MAPKAPK2 total MK2 (1:500, #ADI-KAP-MA015-F, Enzo Life Sciences, Farmingdale, NY)

p-p38 (Thr^{180}/Tyr^{182}) (1:1000, #4511, Cell Signaling Technology, Beverly, MA)

t-p38 (1:1000, #9217, Cell Signaling Technology, Beverly, MA)

p-STAT1 (Tyr^{709}) (1:1000, #9167, Cell Signaling Technology, Beverly, MA)

t-STAT1 (1:1000, #9172, Cell Signaling Technology, Beverly, MA)

SV40 T-antigen (1:1000, sc-58665, Santa Cruz Biotechnology, Dallas, TX)

tubulin (1:20,000, #ab89984, Abcam, Cambridge, MA)

Vinculin (1:10,000, #05-386, EMD Millipore, Dramstadt, Germany).

RNASeq and Differential Expression Analysis

Quiescent cells were lysed using buffer RLT and mRNA was extracted with Qiagen RNeasy kit (#74104, Qiagen). Sequencing libraries were created from mRNA from each cell line using TruSeq stranded mRNA library prep kit per manufacturer's recommendations (RS-122-2101 Illumina, San Diego, CA). Libraries were then pooled and sequenced with NextSeq 500/550 Mid Output v2 kit (150 cycles) according to manufacturer's recommendation (FC-404-2001, Illumina, San Diego, CA). Pooled samples were run in triplicate for a minimum sequencing depth of 20 million reads per sample. Reads were aligned to a custom reference genome using STAR algorithm (66). Our custom reference sequence included the human reference genome and pSLIK-TT- CVB3ΔVP0-Hygro plasmid sequence added as an artificial chromosome and split into five "gene" regions: 5' plasmid, CVB3ΔVP0, 3' plasmid_1, Hygro, and 3' plasmid_2. Mapped reads were quantified using featureCounts (67). Differential expression between CVB3ΔVP0 expressing clonal cell lines and Luciferase expressing polyclonal cell line was assessed using the DESeq2 package in R (68). Alignments were first filtered for genes with a minimum of 1000 reads mapped to at least one sample. Then, the data was normalized and fit to a negative binomial model as described previously (68). To assess different clonal adaptations to CVB3ΔVP0 expression, we first filtered the differentially expressed genes for those that were at least 2-fold different with a false discovery rate (FDR) of < 0.05 in at least one CVB3ΔVP0 clonal cell line. This stringent cutoff (rather than 1.5-fold and FDR < 0.1) reduced the differentially

expressed gene list by 54% and highlights genes of greatest interest. The 100 most variable genes in this list were used to generate PCA and heatmap plots. To assess genes that were similarly disrupted in all CVB3ΔVP0 clonal cell lines, differentially expressed genes were filtered for genes with at least 1.5 fold-change and FDR < 0.1.

Gene set enrichment analysis was performed using DAVID (https://david.ncifcrf.gov/ (69, 70). For each clone cluster, genes that were altered in all constituent clones with a false discovery rate of 10% and at least 1.5 fold change were selected as inputs. The top five outputs from GO_BP_DIRECT and KEGG databases are shown in Table S1.

Phosphatase Assays

Phosphatase assays were conducted as previously described (22). Lysates were generated from quiescent cells stimulated for 2 hours with either mock treatment, 30 ng/mL IFNβ (#300-02BC, Peprotech, Rocky Hill, NJ), 50 U/mL IFNγ (#11040596001, Roche, Mannheim, Germany), 1 ng/mL IL1β (#200-01B, Peprotech, Rocky Hill, NJ), or 100 ng/mL of TNFα (#300-01A, Peprotech, Rocky Hill, NJ). Lysates were diluted prior to phosphatase assay according to Table I. We assumed a concentration of 1000 cells/uL and total protein was assessed as previously described (22). Changes in phosphatase activity were assessed by Students t-test with FDR correction.

Table I: Phosphatase extract amounts used for each assay

Assay	SE Fraction	NE Fraction
pERK2	1000 cells	1000 cells
pp38α	2000 cells	1000 cells
pJNK1	2000 cells	1000 cells
pMK2	5000 cells	12500 cells
pCREB	5000 cells	12500 cells
pSTAT1	3000 cells	1000 cells

Cytokine ELISAs

Cytokine secretion was assessed through the following R&D Systems (Minneapolis, MN) DuoSet kits per manufacturer's recommendation: Human CCL2 (DY279-05), Human IL-6 (DY206-05), Human IP-10 (DY266-05), and Human IL6 (DY270-05). Quiescent cells were stimulated for 24 hours with the treatments described above. Conditioned media was collected and diluted according to Table II for each assay as necessary. Changes in cytokine secretion were assessed by Students t-test with FDR correction.

Table II: Conditioned media dilutions for each cytokine ELISA

Assay	Dilution
CCL2	1:50
MIP1α	1:50
IP10	No dilution
IL6	1:500*

*1:1000 for AC16-Luc

Partial Least Squares Regression

Standard adjusted phosphatase activity data in cell equivalents and cytokine data in pg/mL were formatted and inputted into MatLab. The median value of three replicates was used for PLSR modeling. Data was then mean centered and standardized. Matlab function plsregress was used to compute 4-fold cross-validated PLSR model. From cross-validation, data was grouped by stimulus condition such that training data for each cross-validation model contained equal representation from each stimulus condition (in other words, cell lines were removed). A three component model was built because it maximized the percent variance captured but while minimizing the mean-squared error of the cross-validation models (metric of model stability).

3.5. References

1. Li, Y., Bourlet, T., Andreoletti, L., Mosnier, J. F., Peng, T., Yang, Y., Archard, L. C., Pozzetto, B., and Zhang, H. (2000) Enteroviral capsid protein VP1 is present in myocardial tissues from some patients with myocarditis or dilated cardiomyopathy. *Circulation* 101, 231-234
2. Grumbach, I. M., Heim, A., Pring-Akerblom, P., Vonhof, S., Hein, W. J., Müller, G., and Figulla, H. R. (1999) Adenoviruses and enteroviruses as pathogens in myocarditis and dilated cardiomyopathy. *Acta Cardiol* 54, 83-88
3. Klingel, K., Hohenadl, C., Canu, A., Albrecht, M., Seemann, M., Mall, G., and Kandolf, R. (1992) Ongoing enterovirus-induced myocarditis is associated with persistent heart muscle infection: quantitative analysis of virus replication, tissue damage, and inflammation. *Proc. Natl. Acad. Sci. U.S.A.* 89, 314-318
4. Satoh, M., Tamura, G., Segawa, I., Tashiro, A., Hiramori, K., and Satodate, R. (1996) Expression of cytokine genes and presence of enteroviral genomic RNA in endomyocardial biopsy tissues of myocarditis and dilated cardiomyopathy. *Virchows Arch.* 427, 503-509
5. Esfandiarei, M., and McManus, B. M. (2008) Molecular biology and pathogenesis of viral myocarditis. *Annu Rev Pathol* 3, 127-155
6. Kühl, U., Pauschinger, M., Schwimmbeck, P. L., Seeberg, B., Lober, C., Noutsias, M., Poller, W., and Schultheiss, H.-P. (2003) Interferon-beta treatment eliminates cardiotropic viruses and improves left ventricular function in patients with myocardial persistence of viral genomes and left ventricular dysfunction. *Circulation* 107, 2793-2798
7. Huber, M., Watson, K. A., Selinka, H. C., Carthy, C. M., Klingel, K., McManus, B. M., and Kandolf, R. (1999) Cleavage of RasGAP and phosphorylation of mitogen-activated protein kinase in the course of coxsackievirus B3 replication. *J. Virol.* 73, 3587-3594
8. Marchant, D., Si, X., Luo, H., McManus, B., and Yang, D. (2008) The impact of CVB3 infection on host cell biology. *Curr. Top. Microbiol. Immunol.* 323, 177-198
9. Si, X., Luo, H., Morgan, A., Zhang, J., Wong, J., Yuan, J., Esfandiarei, M., Gao, G., Cheung, C., and McManus, B. M. (2005) Stress-activated protein kinases are involved in coxsackievirus B3 viral progeny release. *J. Virol.* 79, 13875-13881
10. Jensen, K. J., Garmaroudi, F. S., Zhang, J., Lin, J., Boroomand, S., Zhang, M., Luo, Z., Yang, D., Luo, H., McManus, B. M., and Janes, K. A. (2013) An ERK-p38 subnetwork coordinates host cell apoptosis and necrosis during coxsackievirus B3 infection. *Cell Host Microbe* 13, 67-76
11. Garmaroudi, F. S., Marchant, D., Si, X., Khalili, A., Bashashati, A., Wong, B. W., Tabet, A., Ng, R. T., Murphy, K., Luo, H., Janes, K. A., and McManus, B. M. (2010) Pairwise network mechanisms in the host signaling response to coxsackievirus B3 infection. *Proc. Natl. Acad. Sci. U.S.A.* 107, 17053-17058
12. Huber, S. A., and Pfaeffle, B. (1994) Differential Th1 and Th2 cell responses in male and female BALB/c mice infected with coxsackievirus group B type 3. *J. Virol.* 68, 5126-5132
13. Woodruff, J. F. (1980) Viral myocarditis. A review. *Am. J. Pathol.* 101, 425-484
14. Onyimba, J. A., Coronado, M. J., Garton, A. E., Kim, J. B., Bucek, A., Bedja, D., Gabrielson, K. L., Guilarte, T. R., and Fairweather, D. (2011) The innate immune response to coxsackievirus B3 predicts progression to cardiovascular disease and heart failure in male mice. *Biol Sex Differ* 2, 2
15. Glück, B., Schmidtke, M., Merkle, I., Stelzner, A., and Gemsa, D. (2001) Persistent expression of cytokines in the chronic stage of CVB3-induced myocarditis in NMRI mice. *J. Mol. Cell. Cardiol.* 33, 1615-1626
16. Abston, E. D., Coronado, M. J., Bucek, A., Bedja, D., Shin, J., Kim, J. B., Kim, E., Gabrielson, K. L., Georgakopoulos, D., Mitzner, W., and Fairweather, D. (2012) Th2 regulation of viral myocarditis in mice: different roles for TLR3 versus TRIF in progression to chronic disease. *Clin. Dev. Immunol.* 2012, 129486

17. Neumann, D. A., Lane, J. R., Allen, G. S., Herskowitz, A., and Rose, N. R. (1993) Viral myocarditis leading to cardiomyopathy: do cytokines contribute to pathogenesis? *Clin. Immunol. Immunopathol.* 68, 181-190
18. Rehren, F., Ritter, B., Dittrich-Breiholz, O., Henke, A., Lam, E., Kati, S., Kracht, M., and Heim, A. (2013) Induction of a broad spectrum of inflammation-related genes by Coxsackievirus B3 requires Interleukin-1 signaling. *Med. Microbiol. Immunol.* 202, 11-23
19. Pinkert, S., Klingel, K., Lindig, V., Dörner, A., Zeichhardt, H., Spiller, O. B., and Fechner, H. (2011) Virus-host coevolution in a persistently coxsackievirus B3-infected cardiomyocyte cell line. *J. Virol.* 85, 13409-13419
20. Wessely, R., Henke, A., Zell, R., Kandolf, R., and Knowlton, K. U. (1998) Low-level expression of a mutant coxsackieviral cDNA induces a myocytopathic effect in culture: an approach to the study of enteroviral persistence in cardiac myocytes. *Circulation* 98, 450-457
21. Heinrich, R., Neel, B. G., and Rapoport, T. A. (2002) Mathematical models of protein kinase signal transduction. *Mol Cell* 9, 957-970
22. Shah, M., Smolko, C. M., Kinicki, S., Chapman, Z. D., Brautigan, D. L., and Janes, K. A. (2017) Profiling Subcellular Protein Phosphatase Responses to Coxsackievirus B3 Infection of Cardiomyocytes. *Mol. Cell Proteomics* 16, S244-S262
23. Davidson, M. M., Nesti, C., Palenzuela, L., Walker, W. F., Hernandez, E., Protas, L., Hirano, M., and Isaac, N. D. (2005) Novel cell lines derived from adult human ventricular cardiomyocytes. *J. Mol. Cell. Cardiol.* 39, 133-147
24. Behfar, A., Zingman, L. V., Hodgson, D. M., Rauzier, J.-M., Kane, G. C., Terzic, A., and Pucéat, M. (2002) Stem cell differentiation requires a paracrine pathway in the heart. *FASEB J.* 16, 1558-1566
25. Zhang, H., and Bradley, A. (1996) Mice deficient for BMP2 are nonviable and have defects in amnion/chorion and cardiac development. *Development* 122, 2977-2986
26. Schlange, T., Andrée, B., Arnold, H. H., and Brand, T. (2000) BMP2 is required for early heart development during a distinct time period. *Mech. Dev.* 91, 259-270
27. Kandolf, R., Klingel, K., Zell, R., Selinka, H. C., Raab, U., Schneider-Brachert, W., and Bültmann, B. (1993) Molecular pathogenesis of enterovirus-induced myocarditis: virus persistence and chronic inflammation. *Intervirology* 35, 140-151
28. Lévêque, N., Garcia, M., Bouin, A., Nguyen, J. H. C., Tran, G. P., Andreoletti, L., and Semler, B. L. (2017) Functional Consequences of RNA 5'-Terminal Deletions on Coxsackievirus B3 RNA Replication and Ribonucleoprotein Complex Formation. *J. Virol.* 91
29. Rothe, M., Pan, M. G., Henzel, W. J., Ayres, T. M., and Goeddel, D. V. (1995) The TNFR2-TRAF signaling complex contains two novel proteins related to baculoviral inhibitor of apoptosis proteins. *Cell* 83, 1243-1252
30. Hamid, T., Gu, Y., Ortines, R. V., Bhattacharya, C., Wang, G., Xuan, Y.-T., and Prabhu, S. D. (2009) Divergent tumor necrosis factor receptor-related remodeling responses in heart failure: role of nuclear factor-kappaB and inflammatory activation. *Circulation* 119, 1386-1397
31. Higuchi, Y., McTiernan, C. F., Frye, C. B., McGowan, B. S., Chan, T. O., and Feldman, A. M. (2004) Tumor necrosis factor receptors 1 and 2 differentially regulate survival, cardiac dysfunction, and remodeling in transgenic mice with tumor necrosis factor-alpha-induced cardiomyopathy. *Circulation* 109, 1892-1897
32. Wang, M., Tsai, B. M., Crisostomo, P. R., and Meldrum, D. R. (2006) Tumor necrosis factor receptor 1 signaling resistance in the female myocardium during ischemia. *Circulation* 114, I282-289
33. Calabrese, F., Carturan, E., Chimenti, C., Pieroni, M., Agostini, C., Angelini, A., Crosato, M., Valente, M., Boffa, G. M., Frustaci, A., and Thiene, G. (2004) Overexpression of tumor necrosis factor (TNF)alpha and TNFalpha receptor I in human viral myocarditis: clinicopathologic correlations. *Mod. Pathol.* 17, 1108-1118
34. Lodge, P. A., Herzum, M., Olszewski, J., and Huber, S. A. (1987) Coxsackievirus B-3 myocarditis. Acute and chronic forms of the disease caused by different immunopathogenic mechanisms. *Am J Pathol* 128, 455-463

35. Frisancho-Kiss, S., Nyland, J. F., Davis, S. E., Frisancho, J. A., Barrett, M. A., Rose, N. R., and Fairweather, D. (2006) Sex differences in coxsackievirus B3-induced myocarditis: IL-12Rbeta1 signaling and IFN-gamma increase inflammation in males independent from STAT4. *Brain Res* 1126, 139-147
36. Huber, S. A. (1997) Coxsackievirus-induced myocarditis is dependent on distinct immunopathogenic responses in different strains of mice. *Lab. Invest.* 76, 691-701
37. Fairweather, D., Frisancho-Kiss, S., Yusung, S. A., Barrett, M. A., Davis, S. E., Steele, R. A., Gatewood, S. J. L., and Rose, N. R. (2005) IL-12 protects against coxsackievirus B3-induced myocarditis by increasing IFN-gamma and macrophage and neutrophil populations in the heart. *J. Immunol.* 174, 261-269
38. Heim, A., Canu, A., Kirschner, P., Simon, T., Mall, G., Hofschneider, P. H., and Kandolf, R. (1992) Synergistic interaction of interferon-beta and interferon-gamma in coxsackievirus B3-infected carrier cultures of human myocardial fibroblasts. *J. Infect. Dis.* 166, 958-965
39. Thompson, W. L., and Van Eldik, L. J. (2009) Inflammatory cytokines stimulate the chemokines CCL2/MCP-1 and CCL7/MCP-3 through NFkB and MAPK dependent pathways in rat astrocytes [corrected]. *Brain Res.* 1287, 47-57
40. Luster, A. D., and Ravetch, J. V. (1987) Genomic characterization of a gamma-interferon-inducible gene (IP-10) and identification of an interferon-inducible hypersensitive site. *Mol. Cell. Biol.* 7, 3723-3731
41. Zang, Y. C., Halder, J. B., Samanta, A. K., Hong, J., Rivera, V. M., and Zhang, J. Z. (2001) Regulation of chemokine receptor CCR5 and production of RANTES and MIP-1alpha by interferon-beta. *J. Neuroimmunol.* 112, 174-180
42. Zhang, Y. H., Lin, J. X., Yip, Y. K., and Vilcek, J. (1988) Enhancement of cAMP levels and of protein kinase activity by tumor necrosis factor and interleukin 1 in human fibroblasts: role in the induction of interleukin 6. *Proc. Natl. Acad. Sci. U.S.A.* 85, 6802-6805
43. Cahill, C. M., and Rogers, J. T. (2008) Interleukin (IL) 1beta induction of IL-6 is mediated by a novel phosphatidylinositol 3-kinase-dependent AKT/IkappaB kinase alpha pathway targeting activator protein-1. *J. Biol. Chem.* 283, 25900-25912
44. Yuan, J., Liu, Z., Lim, T., Zhang, H., He, J., Walker, E., Shier, C., Wang, Y., Su, Y., Sall, A., McManus, B., and Yang, D. (2009) CXCL10 inhibits viral replication through recruitment of natural killer cells in coxsackievirus B3-induced myocarditis. *Circ. Res.* 104, 628-638
45. Yue, Y., Gui, J., Ai, W., Xu, W., and Xiong, S. (2011) Direct gene transfer with IP-10 mutant ameliorates mouse CVB3-induced myocarditis by blunting Th1 immune responses. *PLoS ONE* 6, e18186
46. Poffenberger, M. C., Straka, N., El Warry, N., Fang, D., Shanina, I., and Horwitz, M. S. (2009) Lack of IL-6 during coxsackievirus infection heightens the early immune response resulting in increased severity of chronic autoimmune myocarditis. *PLoS ONE* 4, e6207
47. Yue, Y., Gui, J., Xu, W., and Xiong, S. (2011) Gene therapy with CCL2 (MCP-1) mutant protects CVB3-induced myocarditis by compromising Th1 polarization. *Mol. Immunol.* 48, 706-713
48. Shen, Y., Xu, W., Chu, Y.-W., Wang, Y., Liu, Q.-S., and Xiong, S.-D. (2004) Coxsackievirus group B type 3 infection upregulates expression of monocyte chemoattractant protein 1 in cardiac myocytes, which leads to enhanced migration of mononuclear cells in viral myocarditis. *J. Virol.* 78, 12548-12556
49. Göser, S., Ottl, R., Brodner, A., Dengler, T. J., Torzewski, J., Egashira, K., Rose, N. R., Katus, H. A., and Kaya, Z. (2005) Critical role for monocyte chemoattractant protein-1 and macrophage inflammatory protein-1alpha in induction of experimental autoimmune myocarditis and effective anti-monocyte chemoattractant protein-1 gene therapy. *Circulation* 112, 3400-3407
50. Yao, H.-L., Song, J., Sun, P., Song, Q.-Q., Sheng, L.-J., Chi, M.-M., and Han, J. (2016) Gene expression analysis during recovery process indicates the mechanism for innate immune injury and repair from Coxsackievirus B3-induced myocarditis. *Virus Res.* 213, 314-321
51. Yalamanchili, P., Datta, U., and Dasgupta, A. (1997) Inhibition of host cell transcription by poliovirus: cleavage of transcription factor CREB by poliovirus-encoded protease 3Cpro. *J. Virol.* 71, 1220-1226

52. Platanias, L. C. (2005) Mechanisms of type-I- and type-II-interferon-mediated signalling. *Nat. Rev. Immunol.* 5, 375-386
53. Bose, A. K., and Janes, K. A. (2013) A high-throughput assay for phosphoprotein-specific phosphatase activity in cellular extracts. *Mol. Cell Proteomics* 12, 797-806
54. Ekerot, M., Stavridis, M. P., Delavaine, L., Mitchell, M. P., Staples, C., Owens, D. M., Keenan, I. D., Dickinson, R. J., Storey, K. G., and Keyse, S. M. (2008) Negative-feedback regulation of FGF signalling by DUSP6/MKP-3 is driven by ERK1/2 and mediated by Ets factor binding to a conserved site within the DUSP6/MKP-3 gene promoter. *Biochem J* 412, 287-298
55. Zheng, Z., Li, H., Zhang, Z., Meng, J., Mao, D., Bai, B., Lu, B., Mao, P., Hu, Q., and Wang, H. (2011) Enterovirus 71 2C protein inhibits TNF-alpha-mediated activation of NF-kappaB by suppressing IkappaB kinase beta phosphorylation. *J Immunol* 187, 2202-2212
56. Engel, K., Kotlyarov, A., and Gaestel, M. (1998) Leptomycin B-sensitive nuclear export of MAPKAP kinase 2 is regulated by phosphorylation. *EMBO J* 17, 3363-3371
57. Meng, W., Swenson, L. L., Fitzgibbon, M. J., Hayakawa, K., Ter Haar, E., Behrens, A. E., Fulghum, J. R., and Lippke, J. A. (2002) Structure of mitogen-activated protein kinase-activated protein (MAPKAP) kinase 2 suggests a bifunctional switch that couples kinase activation with nuclear export. *J. Biol. Chem.* 277, 37401-37405
58. Ben-Levy, R., Hooper, S., Wilson, R., Paterson, H. F., and Marshall, C. J. (1998) Nuclear export of the stress-activated protein kinase p38 mediated by its substrate MAPKAP kinase-2. *Curr. Biol.* 8, 1049-1057
59. Winzen, R., Kracht, M., Ritter, B., Wilhelm, A., Chen, C. Y., Shyu, A. B., Müller, M., Gaestel, M., Resch, K., and Holtmann, H. (1999) The p38 MAP kinase pathway signals for cytokine-induced mRNA stabilization via MAP kinase-activated protein kinase 2 and an AU-rich region-targeted mechanism. *EMBO J* 18, 4969-4980
60. Neininger, A., Kontoyiannis, D., Kotlyarov, A., Winzen, R., Eckert, R., Volk, H.-D., Holtmann, H., Kollias, G., and Gaestel, M. (2002) MK2 targets AU-rich elements and regulates biosynthesis of tumor necrosis factor and interleukin-6 independently at different post-transcriptional levels. *J. Biol. Chem.* 277, 3065-3068
61. Tran, H., Maurer, F., and Nagamine, Y. (2003) Stabilization of urokinase and urokinase receptor mRNAs by HuR is linked to its cytoplasmic accumulation induced by activated mitogen-activated protein kinase-activated protein kinase 2. *Mol. Cell. Biol.* 23, 7177-7188
62. Ho, A. W. Y., Wong, C. K., and Lam, C. W. K. (2008) Tumor necrosis factor-alpha up-regulates the expression of CCL2 and adhesion molecules of human proximal tubular epithelial cells through MAPK signaling pathways. *Immunobiology* 213, 533-544
63. Kandolf, R., and Hofschneider, P. H. (1985) Molecular cloning of the genome of a cardiotropic Coxsackie B3 virus: full-length reverse-transcribed recombinant cDNA generates infectious virus in mammalian cells. *Proc. Natl. Acad. Sci. U.S.A.* 82, 4818-4822
64. Wang, L., Brugge, J. S., and Janes, K. A. (2011) Intersection of FOXO- and RUNX1-mediated gene expression programs in single breast epithelial cells during morphogenesis and tumor progression. *Proc. Natl. Acad. Sci. U.S.A.* 108, E803-812
65. Janes, K. A. (2015) An analysis of critical factors for quantitative immunoblotting. *Sci Signal* 8, rs2
66. Dobin, A., Davis, C. A., Schlesinger, F., Drenkow, J., Zaleski, C., Jha, S., Batut, P., Chaisson, M., and Gingeras, T. R. (2013) STAR: ultrafast universal RNA-seq aligner. *Bioinformatics* 29, 15-21
67. Liao, Y., Smyth, G. K., and Shi, W. (2014) featureCounts: an efficient general purpose program for assigning sequence reads to genomic features. *Bioinformatics* 30, 923-930
68. Anders, S., and Huber, W. (2010) Differential expression analysis for sequence count data. *Genome Biol* 11, R106
69. Huang, D. W., Sherman, B. T., and Lempicki, R. A. (2009) Bioinformatics enrichment tools: paths toward the comprehensive functional analysis of large gene lists. *Nucleic Acids Res.* 37, 1-13

70. Huang, D. W., Sherman, B. T., and Lempicki, R. A. (2009) Systematic and integrative analysis of large gene lists using DAVID bioinformatics resources. *Nat Protoc* 4, 44-57

Chapter 4:

Statistical Data Analysis and Modeling

Millie Shah, Zeinab Chitforoushzadeh, Kevin A. Janes

Department of Biomedical Engineering, University of Virginia, Charlottesville, VA 22908 USA

Keywords

Data-driven modeling, statistical modeling, eigenvalue-based approaches, singular value decomposition (SVD), principal component analysis (PCA), partial least squares regression (PLSR)

Abstract

The availability of large structured datasets has prompted the need for efficient data analysis and modeling techniques. In systems biology, data-driven modeling approaches create models of complex cellular systems without making assumptions about the underlying mechanisms. In this chapter, we will discuss eigenvalue-based approaches, which identify important characteristics (information) of big datasets through decomposition and dimensionality reduction. We intend to address singular value decomposition (SVD), principal component analysis (PCA), and partial least squares regression (PLSR) approaches for data-driven modeling. In multi-linear systems (that share characteristics such as time points, measurements, etc.), tensor decomposition becomes particularly important for understanding higher-order datasets. Therefore, we will also discuss how to scale up these methods to tensor decomposition using an example dealing with host-cell responses to viral infection.

4.1. Introduction

A recurring uncertainty in biology is the molecular underpinnings of an observed cellular or tissue-level phenomenon. With sufficient knowledge about the relevant molecular mechanisms, it is now possible to model large systems of biochemical reactions accurately by simulation (1-4). However, even for well-studied pathways such as receptor tyrosine kinases (5), these hypothesis driven models, including

ODE/PDE and stochastic models, quickly uncover gaps in our understanding (6). Often, the phenomenon of interest is so poorly characterized that we only really have a sense of the pathways that are important and a rudimentary rule set for how they could interact (7, 8).

In these circumstances, it can be advantageous to pursue statistical models that do not prescribe mechanisms but allow the data to define the system of interest (9, 10). In statistical modeling, one must first collect a systematic dataset that has been designed to capture as many relevant variations and covariations as possible among genes, proteins, and cellular phenotypes (11, 12). Although not absolutely required, it is strongly recommended that the statistical approach be chosen conceptually before the data acquisition. Each class of models has its own set of strengths and weaknesses (9), and ideally the dataset should be tailored to exploit a model's strengths and avoid its weaknesses. Bayesian modeling is most effective for inferring the network structure of the phenomena being studied while techniques like partial least squares are ideal for predicting new behaviors (10). Statistical models may be "mechanism free", but it is possible to guide models toward identifying new mechanisms by selecting the right biomolecular measurements and designing the experiments appropriately (10, 13).

With current technologies in molecular biology, any laboratory can now generate datasets that are highly multivariate. Statistical modeling serves as a powerful way to extract as much information as possible from these often expensive and difficult-to-conceptualize datasets. The resulting patterns and relationships identified by statistical models are not always apparent when analyzing the full spectrum of the dataset, as it often contains measurements not significant to the system. Thus, the class of

statistical models that we will discuss in this chapter center around those that build simplified representations of data to give a clearer picture of possible mechanisms underlying the system.

Usually, in modern biological datasets, we have many more variables per observation than observations of each variable. These “short and fat” data tables (or matrices) are inherently underconstrained; in frequentist statistics, it is equivalent to having fewer than zero degrees of freedom. Consequently, many of the dimensions are redundant with one another, in that they can be expressed as linear combinations of other variables. This redundancy allows the data matrix to be “reduced” in interesting and useful ways, depending on the type of statistical model and the overall goals of the study.

Here, we will review three main categories of statistical models that reduce the dimensions of multivariate datasets. We begin with singular value decomposition (SVD), which draws on the concept of eigenvalues and eigenvectors to decompose a matrix according to its eigenvalue spectrum. Then, we will discuss principal components analysis (PCA), which is conceptually akin to SVD but yields a factorized model that is more directly interpretable with respect to the starting dataset. Finally, we will link reduced dimensions to the concept of predictive statistical modeling through partial least squares regression (PLSR). As case studies, we include more modern implementations of SVD, PCA and PLSR, including tensor decomposition of data cubes or hypercubes, in anticipation for the types of structured datasets that will be forthcoming in molecular and cellular biology.

4.2. Singular Value Decomposition

Before going into detail about SVD computation, it is important to introduce some basic concepts from vector and matrix algebra. Most datasets can be organized as matrices with the rows indicating experimental observation, such as treatments and time points and the columns indicating variables, such as enzymatic activity and phosphoprotein levels.

One way to simplify multidimensional data is to focus on parts of the data that show the most variation. Linear algebra serves this purpose by finding orthogonal or linearly independent vectors in the data matrix. Since orthogonal vectors have zero projections into one another, they can act as latent variables onto which the data can be mapped (14). Orthogonal vectors of a data matrix can be identified by calculating eigenvectors. The nonzero *eigenvector* (x) of matrix A satisfies the equation:

$$Ax = \lambda x \qquad (1)$$

Where A is a square matrix and λ is a scalar called “eigenvalue”.

An eigenvector can serve as a new dimension along which the data can be projected. By definition, matrix A is an n $\times$ n square matrix. However, typical biological datasets have fewer observations than variables and thus are rarely square matrices with full rank. One way to solve this problem is by factorizing the data matrix using singular value decomposition.

4.2.1. Mathematical Framework

Singular Value Decomposition

Suppose that we define an m × n data matrix A that can be broken down into the product of three other matrices U, S, and V. This factorization results in the following equation:

$$A_{m\times n} = U_{m\times l} S_{l\times l} V^{\mathrm{T}}_{l\times n} \quad (2)$$

Where U is an m × l left-singular matrix, S is a square l × l diagonal matrix, V is an l × n right matrix, and U and V^T are orthogonal matrices. The diagonal entries in S are the singular values of A (square roots of non-zero eigenvalues of U and V^T) descending in magnitude from top left to bottom right, the columns in V^T are right-singular vectors and the columns in U are left-singular vectors (15) (Figure 1). Once singular vectors are extracted, the significant ones can be determined and used for visualizing the data.

4.2.2. Application of SVD to gene expression data analysis

Gene expression data is a good candidate for singular value decomposition based analysis due to the inherent noise in the measurements that makes the detection of small signals rather difficult. Alter et al. performed SVD analysis on the budding yeast elutriation gene microarray data published in (16). The elutriation dataset used by Alter et al. contained 5,981 genes (n=5,981 genes) captured over the course of one yeast cell cycle (fourteen time points; m=14). The dataset can be tabulated to an n × m matrix with each row reflecting the expression of a single gene in 14 different time points (14-arrays) and each column showing the expression of n-genes in a single array (timepoint). SVD transforms this

dataset from an n × m space to a reduced l-eigengenes × l-eigenarrays subspace where l= [min m, n] (Figure 1). The diagonals in the l × l matrix $\mathcal{E}$ are eigenvalues here called "eigenexpression levels" [ε_l] which can be used to calculate "fractions of eigenexpression" for the l^{th} eigenvalue from the equation below:

$$p_l = \frac{\varepsilon_l^2}{\sum_{k=1}^{l} \varepsilon_k^2} \qquad (3)$$

Alter et al. used fractions of eigenexpression as a mean to infer the significance of eigengenes and their corresponding eigenarrays (singular vectors). Once the significance of singular values (SVs) was determined, the relationship between these mathematical concepts and biological processes or cellular states, in this case cell cycle, were investigated. To this end, the authors visualized individual singular values by plotting the expression level of each eigengene over time. Since the authors were interested in gene programs involved in a specific cellular state, they filtered out the first singular vector because it followed a steady state expression pattern. The next three SVs showed biologically meaningful oscillations during cell cycle. The oscillations of the second and fourth SVs at early time points corresponded to a transient response to elutriation. Thus SVD naturally decomposed the dynamical patterns of gene expression in the yeast cell cycle.

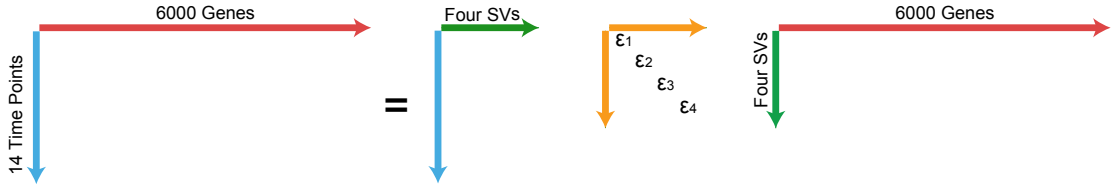

Figure 1. SVD Decomposition Schematic.
Decomposition of the yeast elutriation data from Spellman et al., 1998 into a left singular-value matrix, a square matrix of eigenvalues (four eigenvalues shown), and a right singular-value matrix.

4.3. Principal Components Analysis

Following SVD, principal components analysis (PCA) can be used to compress a dataset to relevant measurements that approximate the data. Both computational and visual analysis is often hard to do in higher order datasets as each measurement (observation) constitutes its own dimension in space and the value of each sample (variable) constitutes a point in each of these dimensions. By transforming the data using PCA, we can identify important relationships in the data.

First, eigenvalues and eigenvectors are derived from the data covariance matrix (17, 18). These eigenvectors make up an orthogonal basis set, or set of linearly independent vectors that, when combined, can describe the data. The eigenvectors paired with the smallest eigenvalues are eliminated to yield a compressed basis set. This basis set of eigenvectors is then used to generate a transformed data matrix, the dimensions of which are called latent dimensions or principal components (PCs) (17-19). A principal component is by analogy a singular vector in SVD.

A latent dimension is a new dimension created to capture the majority of information in multiple of the original dimensions (20). Mathematically, a principal component is a linear combination of the original data dimensions, weights for which are determined by the magnitude of the eigenvector corresponding to that principal component (18, 21). The eigenvector paired with the largest eigenvalue defines the first principal component and captures the greatest amount of variance in the data (18, 19). In this component, the original dimensions with the most variance in variable data will have the largest weighting. Because the PCs are orthogonal, the second principal component will point in a

direction perpendicular to the first component and capture the majority of the leftover variance. This iteration continues for all subsequent PCs. Thus, the transformed dataset is usually only made up of a handful of latent dimensions because they can capture the majority of the data variance eliminating any statistical noise from subsequent PCs. This filtering makes relevant relationships between samples more readily apparent.

Further, one can create predictive models with latent dimensions by searching for relationships between PCs using principal components regression (PCR). This method utilizes established regression techniques to find the relationship between several variables (predictor variables) and dependent variables not included in the predictors (21). PCR uses the first few principal components to simplify the analysis of many variables to linear or multilinear regression between the components (predictors) and the desired measurements (18, 21). Resulting coefficients of the PCs, fitted using least-squares approaches, can be decomposed to regression coefficients of each of the original variables in the component. The variable with the largest magnitude coefficient is the most correlated to the desired dependent variable while the sign of the coefficient indicates positive or negative correlation (21). In this way, decomposition by PCR can be used to extract relationships between different variables in the dataset.

Thus, PCA and PCR can be used not only to generate hypotheses about sample relationships but also to generate data-driven predictions. PCA is often used to analyze DNA (or cDNA) microarrays by clustering observational data such that relevant coregulations of genes or relevant similarities or disparities between cellular samples such as different cancer tumors are exposed (22-24).

4.3.1. Mathematical Framework

Principal Component Analysis (PCA)

First, the dataset should be mean-centered so that the mean of each variable across all observations is zero. This adjustment greatly simplifies the covariance matrix calculation as well as eigenvector determination. For centering, the means of each variable (column) should be subtracted from each observation of that variable (row) in an element-wise manner as shown in Eqn (4).

$$\begin{bmatrix} M_{1,1} & M_{1,2} \\ M_{2,1} & M_{2,2} \end{bmatrix} - \begin{bmatrix} \overline{M_1} & \overline{M_2} \\ \overline{M_1} & \overline{M_2} \end{bmatrix} = \begin{bmatrix} A_{1,1} & A_{1,2} \\ A_{2,1} & A_{2,2} \end{bmatrix} \quad (4)$$

Here M is a representative 2×2 data matrix and another matrix of the same size, containing the means of each sample (columns), is subtracted to generate the adjusted data matrix A. Notice that the mean of all columns should now be zero.

Now the covariance matrix of the dataset can be found from A. While in SVD the original dataset was used for decomposition, in PCA the chief interest is in the covariance of the data not the absolute magnitude (20). Thus, the sample covariance matrix is used for decomposition as shown in Eqn (5).

$$C = \begin{bmatrix} \mathrm{cov}(1,1) & \mathrm{K} & \mathrm{cov}(1,N) \\ \mathrm{M} & \mathrm{O} & \mathrm{M} \\ \mathrm{cov}(M,1) & \mathrm{K} & \mathrm{cov}(M,N) \end{bmatrix} = \frac{1}{N-1}\sum_{i=1}^{N}(A_i - \overline{A})(A_i - \overline{A})^T \qquad (5)$$

which simplifies to $C = AA^T/(N-1)$

Here C is a symmetric sample covariance matrix, where the elements of the matrix are the covariances of each observation (row) with every other variable dimension, M denotes the number of observations, and N is the number of variables (columns) in A. Because A is mean-centered ($\overline{A}$ = 0), this equation simplifies to $AA^T/(N-1)$. Using this notation, we can find the eigenvectors of C by decomposing it into a diagonal matrix D. (Schlens, 2003).

We can rewrite Eqn (2) as,

$$C = VDV^T \qquad (6)$$

such that the columns of V are the eigenvectors of A which correspond to the eigenvalues in the diagonal matrix D. Here, eigenvalues correspond to the contribution of that eigenvector to the reconstruction of C from the decomposition. For the covariance matrix, small eigenvalues correspond to eigenvectors that contain a small amount of the variance in the data. Thus, columns corresponding to low-magnitude eigenvalues can be eliminated from V to yield a compressed eigenvector matrix (B) that will make up the basis set of the data A (25).

Multiplying the compressed eigenvector matrix B with A transforms the adjusted data into principal component space as given by Eqn (7).

$$P = B^{\mathrm{T}} A \tag{7}$$

Here P is the approximated data matrix where the rows correspond to latent dimensions or principal components and the columns correspond to samples. The elements of the matrix are the values of samples in each component. As previously mentioned, the eigenvectors are ordered from greatest corresponding eigenvalue to smallest. Therefore, the first principal component (first eigenvector) accounts for the most variance in the data. If P is composed of three or fewer principal components, the sample values can be plotted in a 2D or 3D fashion to group covarying samples.

Implementation of this method and example plots will be discussed later in the context of host-cell responses to CVB3 viral infection (26).

Principal Component Regression (PCR) Using Total Least Squares

After the principal components have been defined, there may be instances in which knowing the relationship between principal components or principal components and an independent observation dimension are useful. Linear or planar orthogonal regression techniques can be used to determine these relationships (18, 19, 21). In this section we focus on total least squares regression (TLSR).

As opposed to ordinary least squares regression, TLSR aims to minimize the perpendicular residual error from the regression fit (Pearson, 1901). This is an important distinction as it implies variance or measurement error in all the dimensions. Measurement inaccuracies create uncertainty or associated variance in the position of each data point in principal component space. Therefore, regression models should take this into account when minimizing residual error to create an unbiased fit. For PCA, all the observation dimensions used to create latent dimensions are subject to measurement error or variance (Pearson, 1901).

First, appropriate PCs must be chosen as predictor variables. In most cases choosing the first one or two principal components is the most relevant (Jeffers, 1967; Jolliffe, 2002). However, this is not always the case and a more in-depth discussion of choosing appropriate PCs can be found in Jolliffe 2002.

Once predictor variables have been chosen, iterative computational optimization algorithms, in environments like Matlab, can be used to identify the best-fit line or plane. In general, these computational methods attempt to minimize Eqn (8) (Figure 2).

$$E = \sum_{i=1}^{N} \left| r_i^2 \right| \qquad (8)$$

where E is the residual error and r_i is the orthogonal distance of a data point (o) from the regression. The schematic Figure 2 illustrates the orthogonal distance (r_i) of a representative data point (o) from the linear regression line.

While PCA is an unsupervised decomposition method that does not take into account the inherent variance between variables, it can extract valuable information from multidimensional datasets. This information can be used to generate simplified regression models by using the principal components themselves as predictors rather than the original observations.

4.3.2. Application of PCA: Decomposition of Experimental Data

In this section we will use data published in Jensen et al. 2013 quantifying host-cell viral infection responses to demonstrate the utility of multidimensional decomposition in systems modeling.

Biological Introduction

Viral myocarditis including heart failure and dilated cardiomyopathy are most commonly attributed to coxsackievirus B3 (CVB3) infection of cardiomyocytes. Acute infections cause host-cell damage and viral progeny release. These progeny then infect neighboring cells and advance tissue damage until the immune system can clear the infection.

CVB3 induced myocarditis is the most common cause of heart failure in young adults, children, and immunocompromised patients. The only late-stage treatment available in these cases is heart

transplantation suggesting that once the virus has begun to successfully replicate in host-cells, there is little that can be done other than remove the diseased tissue. Thus, early-stage treatments remain the best hope for reducing tissue damage.

However, no successful treatment currently exists because initial host-cell responses to infection are poorly understood. CVB3 must interact with several host-cell intracellular components to replicate successfully (27). Such interactions include degrading certain machinery while taking over others, suggesting that numerous cellular signaling pathways are disrupted (28). Treatments developed to recover normal function of these pathways before viral progeny are released remain the best hope for attenuation of disease severity.

Experimental Measurements and Generated Data

Because host-cell signaling consists of highly connected networks of proteins, perturbations in these pathways must be studied simultaneously to truly understand, at a systems level, how CVB3 affects the host. To accomplish this, (26) surveyed several kinase activities in response to viral infection. The activities of eight canonical stress and inflammatory response kinases were quantified by phosphoprotein abundance in a phopho (p)-ELISA format. Each of these measurements was made in response to five different CVB3 viral doses (MOI) at several time points. In addition, six host-cell responses were quantified in a parallel experimental set-up. The resulting datasets form tensor structures (three-dimensional matrices) as shown in Figure 3

To draw parallels between the temporal patterns of kinase activation and cellular output, the data can be plotted in several 2D plots and then visually compared to each other. An example of this method is displayed in Figure 4.

From visual inspection we can see that the data does not have correlated or simple activation patterns with respect to time or MOI. Some of the kinases show an increase then decrease in activation with time like Hsp27, ATF2, AKT, GSK3 and p38. Others have more complex bimodal temporal patterns like CREB, ERK, and IκBα. Further, some kinases show increased activation with respect to MOI that decreases after a certain MOI threshold is reached (Akt and IκBα, Figure 4) while others show less generalizable patterns. Additionally, while the cellular outputs all show increases in expression (VP1), activation (casp-8, casp-9, casp-3), or abundance (RVP, Death) with respect to both MOI and time, their relationship to the kinases cannot be inferred. Taken as a system, there is no simple way to explain the relationships between kinases, cellular outputs, time, and MOI using this type of data processing.

Tensor Decomposition

In such cases, tensor decomposition can illuminate important correlations in the data. Higher order data structures can be decomposed and modeled with either of two generalized SVD and PCA methods. Tucker decomposition (29) and CANDCOMP/PARAFAC (CP) (30, 31) are established methods that were first developed in the fields of psychometrics and chemometrics.

CP expresses an N-mode data tensor as a sum of rank one tensors, while Tucker decomposition factorizes the data into a core tensor and N-corresponding matrices (31, 32). Thus, for a three mode tensor, CP factorizes the data into a sum of rank one tensors expressed as the outer product (⊗) of vectors from three matrices (A, B, and C) (Eqn. 9, Figure 5A). This operation is also known as the Khatri-Rao product of A, B, and C. Tucker decomposition yields one core tensor W) and three matrices (A, B, and C) (Eqn. 10, Figure 5B). In both cases, the matrices A, B, and C correspond to mode 1, 2, and 3 respectively and contain the loadings or eigenvectors that define each principal component within that mode.

$$X_{P\times Q\times R} = \sum_{n=1}^{N} a_n \otimes b_n \otimes c_n \qquad (9)$$

where N is the number of components or rank one tensors being used to approximate the data tensor X and a_n, b_n, and c_n are the vectors corresponding to the *nth* component.

$$X_{P\times Q\times R} = \sum_{p=1}^{P}\sum_{q=1}^{Q}\sum_{r=1}^{R} g_{pqr} a_p \otimes b_q \otimes c_r \qquad (10)$$

where g_{pqr} is an element in the core tensor G and a_p, b_q, and c_r are column vectors from the matrices A, B, and C.

It is important to note these generalized methods differ from PCA in that they usually result in unique solutions. In two-way PCA, the PCs can be rotated in space and still maintain the amount of variance captured by changing the scaling within the PCs. This is not true for higher order PCA as rotation will cause a loss of fit (32). Consequently, CP and Tucker models differing in the number of components

calculated must be done iteratively; each component cannot be found serially. In this way, CP and Tucker decomposition expand on the concepts of bilinear PCA to model important covariations in the data while maintaining the information-rich tensor structure.

To apply these methods to our CVB3 host-cell kinase signaling dataset (Figure 3A) we must first mean center and standardize our tensor (32). We want to center along the first mode or the observation mode, which, in this case, is the MOI dimension. It follows then that our variables are the different kinases (mode 2) through time (mode 3). Just as in bilinear PCA, mean centering along the first mode gives us a zero offset to calculate the variances in phosphosignal of each phosphoprotein. Next, standardization, or scaling by the standard deviation, in modes 2 (phosphoprotein) and 3 (time) allows us to compare these variances between phosphoproteins, time points, and MOIs.

Now we can decompose this adjusted tensor using the PARAFAC (CP) algorithm. Unique solutions or sets of principal components (A, B, and C) are fit using an alternating least squares (ALS) approach (32). In short, this algorithm uses the adjusted data and an initial guess for B and C (mode 2 and 3 principal components respectively) to fit A by least squares regression. This is then repeated for each matrix A, B, and C until a convergence condition is reached.

As mentioned before, these steps have to be repeated for models with differing numbers of components. To determine the optimal number of components for the model, several different numbers of components can be surveyed, each followed by inspection of certain fit and stability metrics. These metrics include percent variance of the original dataset captured, sum-of-squared

residuals between the model and original data, crossvalidation or leave-one-out stability analysis, and concordance with the Tucker core tensor (20). The last of these utilizes the idea that PARAFAC will yield the same answer as Tucker decomposition with a core tensor of ones on the superdiagonal and zeros elsewhere (33). Thus, 100% concordance means the A, B, and C matrices are the best possible fit of the data and do not need to be scaled by a non-superidentical core matrix.

After mean centering and standardizing the host-cell phosphoprotein dataset, a two compartment PARAFAC model can be generated which captures 80% of the variance in the original data. Two components were considered optimal as larger models did not meet concordance requirements and smaller models did not capture as much variance. To interpret this simplified model, we can visualize both the kinase and time loadings in PC1 and PC2 (Figure 6). The magnitudes of the loadings indicate the amount it contributes to the respective principal component. The greater the magnitude of the loading, the greater contribution that variable has to the model generated from the Khatri-Rao product of the principal components.

Thus, when interpreting Figure 6, we want to focus on clusters that lie far from zero on at least one PC, because those signaling proteins and times that lie close to the origin have little to no influence on the model. As labeled in the figure, the PARAFAC model exposes two interesting clusters: 1) ERK and time 0.17 hrs and 2) p38 and time 24 hrs. This suggests that p38 signaling is responsible for most the variance associated with MOI at later time points while ERK signaling is responsible for most of the variance associated with MOIs at early time points. Biologically, we can now hypothesize that the ERK and p38 pathways are the relaying the most information about CVB3 mediated viral infection at early

and late times respectively (26). How the viral genome interacts with these pathways would still need to be studied in carefully designed experiments that isolate the role of these pathways in vitro or in vivo. However, this demonstrates the ability of higher order decomposition techniques to uncover new hypothesis that lead to more targeted systems-biology studies.

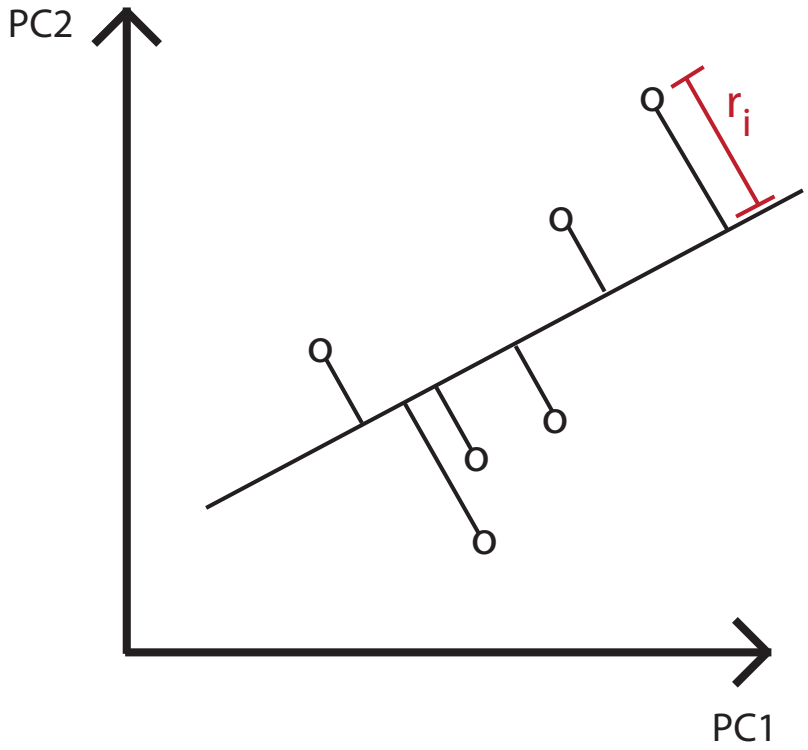

Figure 2. TSLR Orthogonal Residual Schematic.
TLSR uses orthogonal residuals (red – r_i) to fit a regression line to data (o) displayed in PC space.

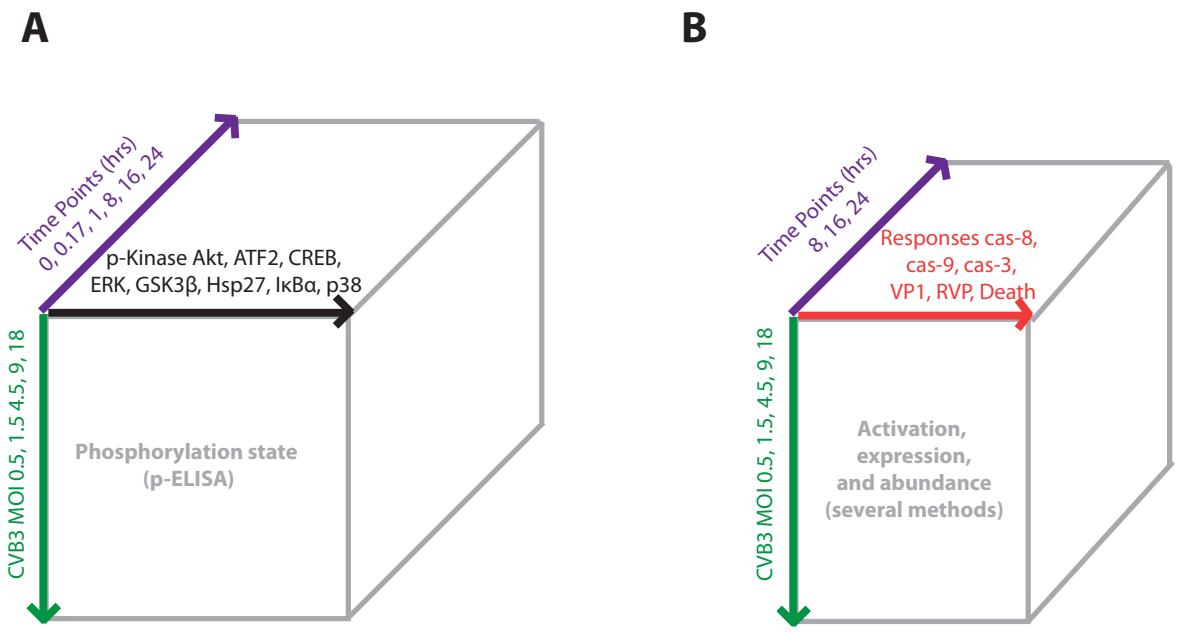

Figure 3. Tensor structure of host-cell response data.
Tensor data structure of phosphoprotein ELISA signal (A) and cell response data (B).

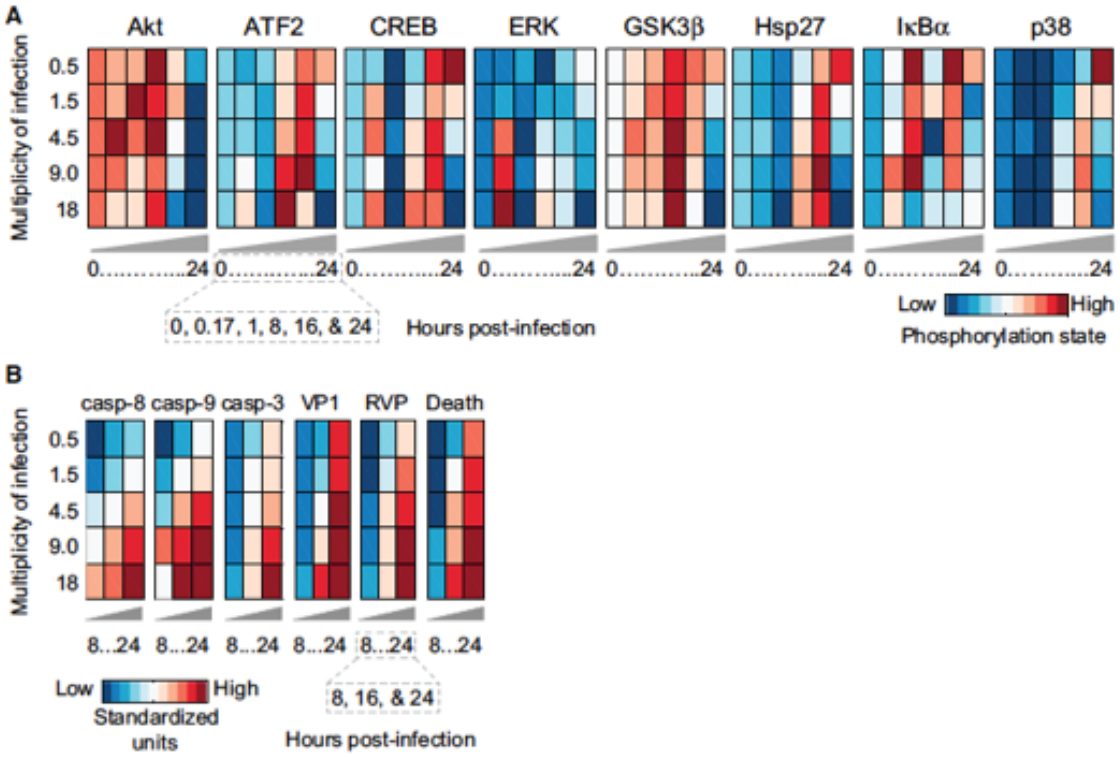

Figure 4. Visualization of host-cell response data.
Heat map visualization of phosphoprotein signals (A) and cell response data (B) given 5 different viral doses (MOIs)measured at 6 (A) or 3 (B) time points post-infection. Data are reprinted from Jensen et al., 2013.

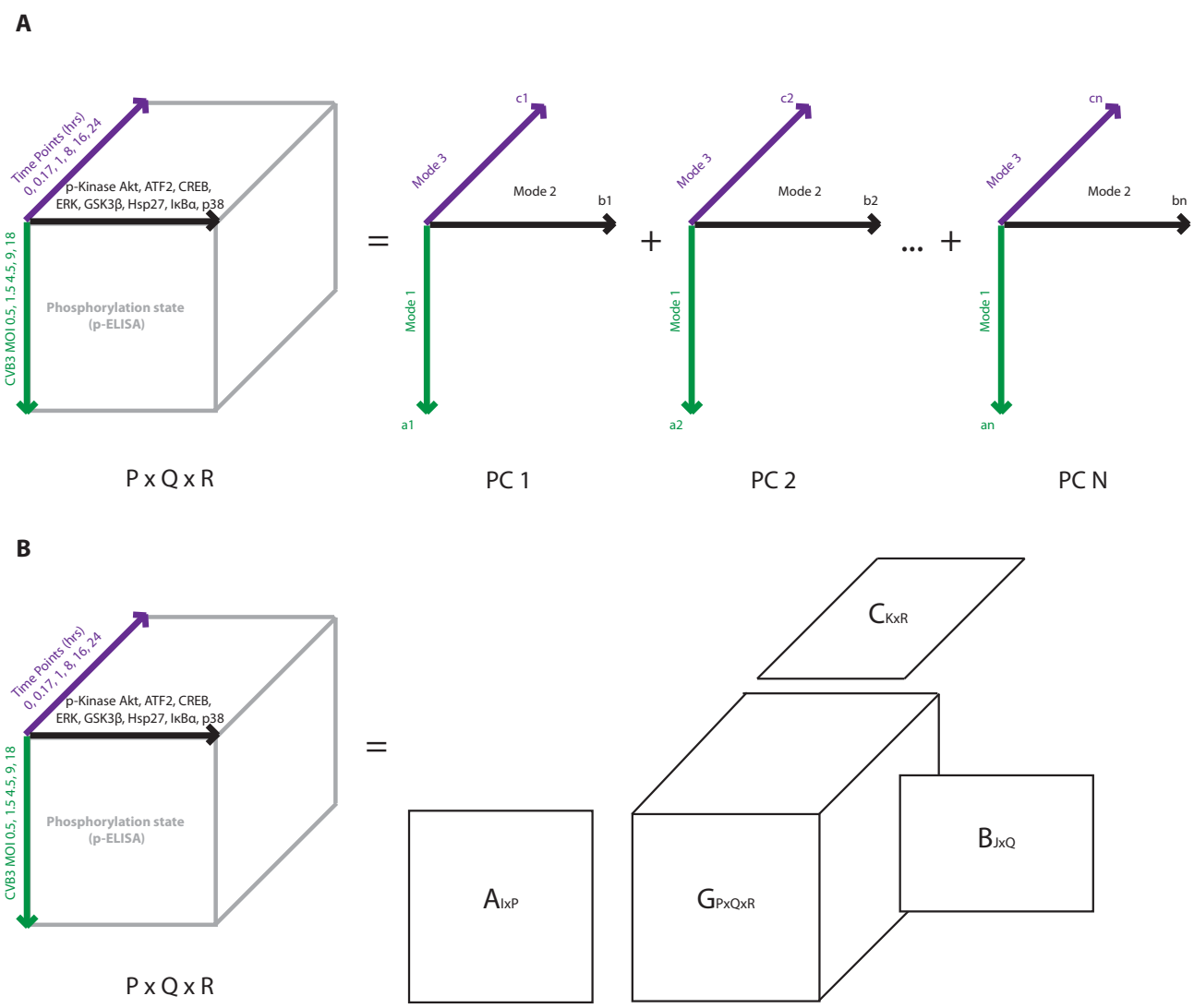

Figure 5. Schematic of Tensor Decomposition Techniques.
Schematic of CP (A) and Tucker (B) decomposition using experimental phosphoprotein data structure from Figure 4. The data matrix and core matrix G have dimensions
$P \times Q \times R$, PC = principal component, lowercase letters a, b, c denote vectors, and uppercase letters A, B, C denote matrices.

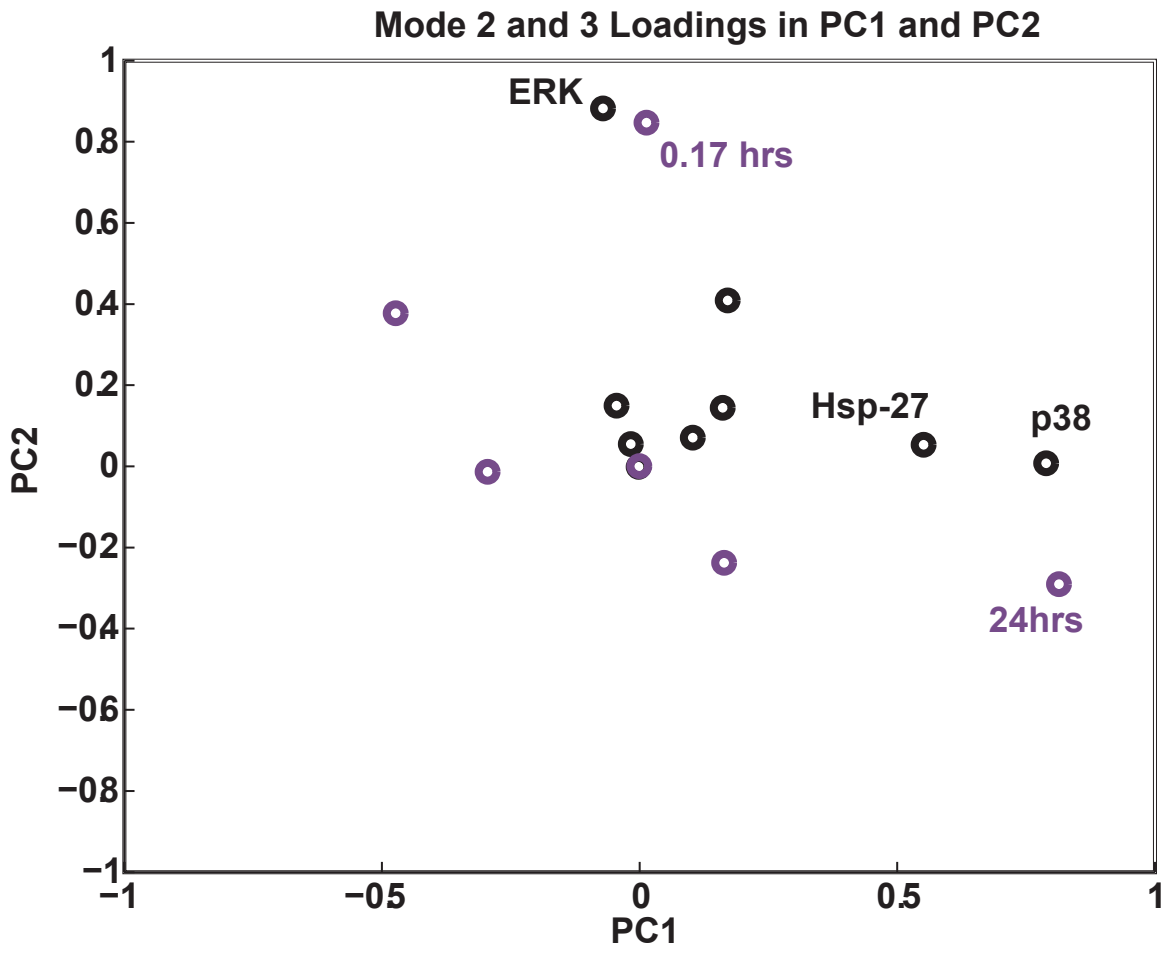

Figure 6. Visualization of phosphoprotein status in principal component space. Phosphoprotein (mode 2, black) and time post-infection (mode 3, purple) loadings are mapped in principal component space to show clusters with similar loadings in each PC. Loadings and PCs were generated using PARAFAC analysis.

4.4. Partial least squares regression (PLSR)

As mentioned in the previous section with data matrices, PCA defines principal components that are optimized to capture the overall variance in the data matrix *A*. However, this does not mean that the resulting principal components are optimally interpretable, nor that they are the best regressors for predicting another data matrix. In such circumstances, it is preferred to rotate the leading principal components (14), which is easily achieved in two dimensions with the following linear operator:

$$\begin{bmatrix} \cos\theta & -\sin\theta \\ \sin\theta & \cos\theta \end{bmatrix} \qquad (11)$$

(Similar operators can be defined for rotations in three dimensions.) A key point is that this "subspace rotation" does not affect the overall variance captured by the PCA model, because the solution is rotationally degenerate. Rather, it rebalances the variance among the retained principal components. Subspace rotation is commonly employed when building statistical models of biological processes (17, 34).

For statistical modeling of signal transduction, PLSR has proved widely useful and informative. Successful models have been built to link signaling to cell death (17, 35-38), cell-cycle progression (36, 39), proliferation (40-42), and cytokine secretion (37, 38, 41, 43). More-recent theoretical work has suggested that, because of the fundamental chemical-reaction kinetics of biochemical networks, PLSR

is virtually guaranteed to reduce a signaling circuit down to a handful of principal components for follow-on analysis (44). Of course, there are caveats about framing a proper X $\rightarrow$ Y hypothesis (10), but it is reassuring to know that the approach is fundamentally sound and highly versatile. Consequently, PLSR has entered into the standard curricula for many systems-biology courses (45).

4.4.1. Mathematical Framework

For regression modeling within high-dimensional datasets, there is a more effective way of identifying correlated principal components than PCR followed by subspace rotation. In partial least squares regression (PLSR), principal components are identified numerically that maximize the covariance between an independent data matrix (*X*) and a dependent data matrix (*Y*). (Note the distinction from PCA, which simply maximizes capture of the overall variance of a single data matrix.) Computationally, PLSR arrives at a covariance model by jointly factorizing *X* and *Y* as follows:

$$X = TP^{\mathrm{T}} \tag{12}$$

$$Y = UQ^{\mathrm{T}} \tag{13}$$

Where *T* and *U* are scores vectors and *P* and *Q* are loading matrices

The regression between *X* and *Y* is linear between the "scores vectors" of the independent and dependent matrices:

$$U = TB \quad (14)$$

Thus, $Y = TBQ^{T}$ (15)

The simplest protocol for building a PLSR model is by using the nonlinear iterative partial least squares (NIPALS) algorithm. In this algorithm, a row from *Y* is randomly chosen as the first guess for a scores vector (*u*), and then X is projected onto *u* to define the first guess at a "loadings vector" *p*. Here, the exchange of scores vectors (using *u* with *X* and *t* with *Y*) is critical for linking the two matrices together and building a PLSR model that maximizes the covariance between *X* and *Y* (46). The first iteration of the loadings vector is then normalized and projected onto *X* to define a provisional *t*, which is subsequently projected onto *Y* to calculate the first iteration of its loadings vector, *q*. This loadings vector is normalized to unit length as done previously for *p*, and then the normalized *q* is projected onto *Y* to define the second iteration of *u*. This process continues until *u* converges to a fixed value within a specified tolerance. Software for building PLSR models is readily available in MATLAB, R, as well as independent commercial platforms (10).

4.4.2. Application of PLSR: Modeling Tensor Data Sets

In the previously discussed example from Jensen et al. 2013, two datasets were generated, a phosphoprotein signal tensor and a cell response tensor (Figure 3). Unlike PCA, PLSR is a powerful technique that can help identify relationships between these two tensors and point to kinases that dictate viral infection responses in cardiomyocytes.

As mentioned previously, PLSR generates principal components that capture the maximal variances in both an input tensor and an output tensor. In this way, PLSR is a supervised decomposition and regression method that can be used as a predictive model. In this example, the predictor dataset is the signaling activity tensor (Figure 3A) and the dependent data is the cellular response tensor (Figure 3B). Note that the dimensions of the tensor datasets do not have to be equal except in mode 1 (observations). Before attempting PLSR, the tensor must be centered and standardized as described for the PARAFAC model.

Once each dataset is adjusted, a crossvalidated PLSR model can be developed by using a NIPALS algorithm to solve Eqns. 12 & 13 (47). These equations are essentially the same as those for the PARAFAC model; the difference is that NIPALS solves them simultaneously, until some convergence criterion is met.

The four-component solution captures 89% of the variance in the predictor tensor and 91% variance in the output tensor. The resulting model can accurately predict all cellular outputs as shown in Figure 7. To visualize the significant players in this multi-component model, we must choose which principal component combinations to look at. In general, we want to look at PCs that capture the most variance in the data, which are usually PC1 and PC2. However, in this case, PC3 and PC4 captured substantial amounts of non-redundant variance in the data. By analyzing Figure 8 in a similar fashion to Figure 6, we find that p38, Hsp27, CREB, GSK3B, and Akt cluster with four of the six cellular outputs (caspase 3 activation, viral progeny release, VP1 expression, and cell death).

We can then hypothesize that these signaling proteins are influential in deciding cellular responses to CVB3 infection and could be potential treatment targets to attenuate subsequent tissue damage. By utilizing the powerful extraction capabilities of tensor decomposition and PLSR modeling we have effectively eliminated half the potential targets we started with. We could eliminate more by looking at other PCs and isolating those that correlate with early time points. This example illustrates the utility of different tensor decomposition and modeling techniques that result in rational experiment design invaluable to systems biologists struggling to understand and manipulate immensely complex cellular networks.

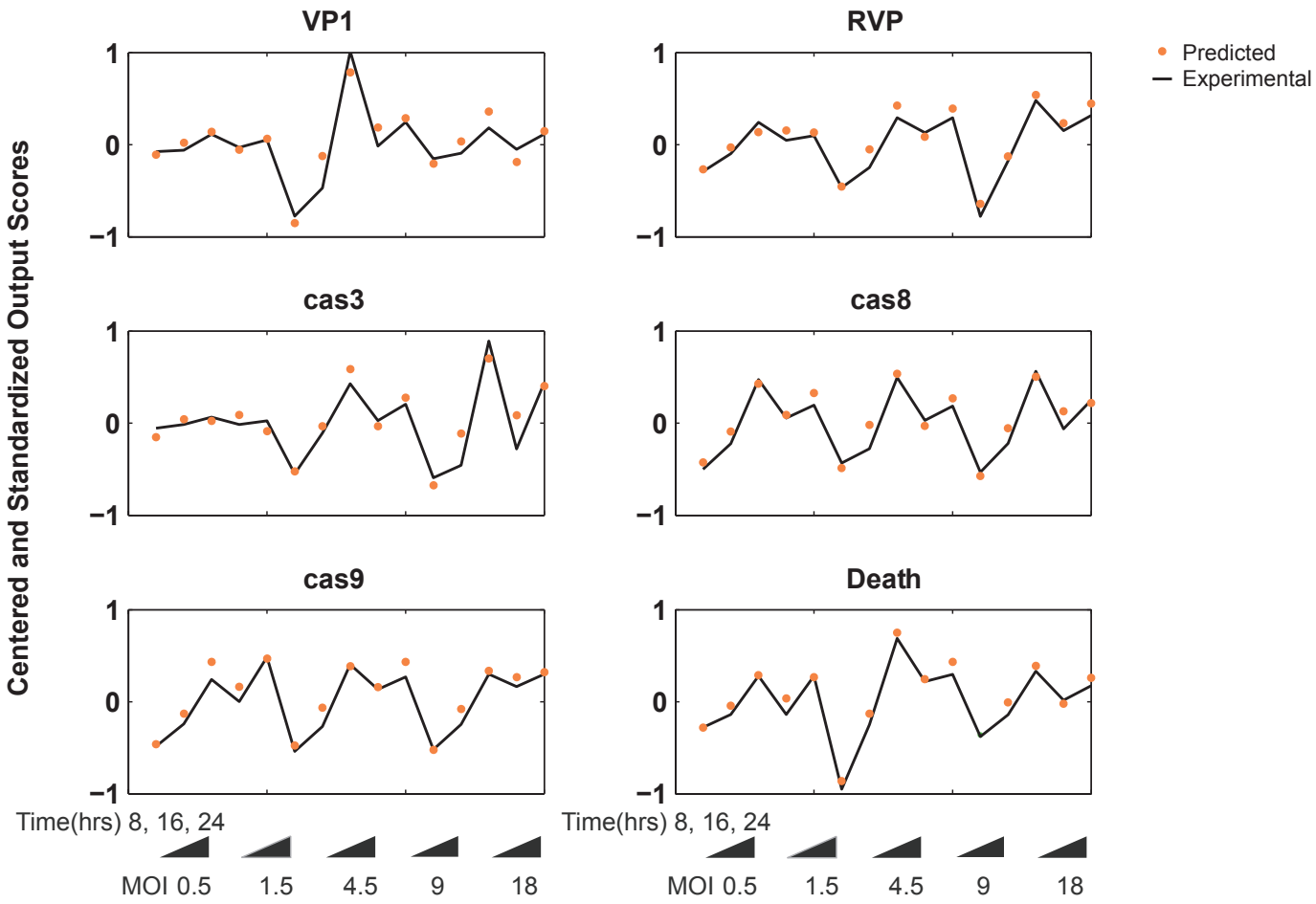

Figure 7. PLSR model of experimental host-cell response data.
All six of the cellular response measurements (black) can be successfully predicted by a four component PLSR model (orange). (VP1 – viral capsid protein 1, RVP- release of viral progeny, cas3 – caspase 3, cas8 – caspase 8, cas9 – caspase 9, Death – cellular death via MTS assay).

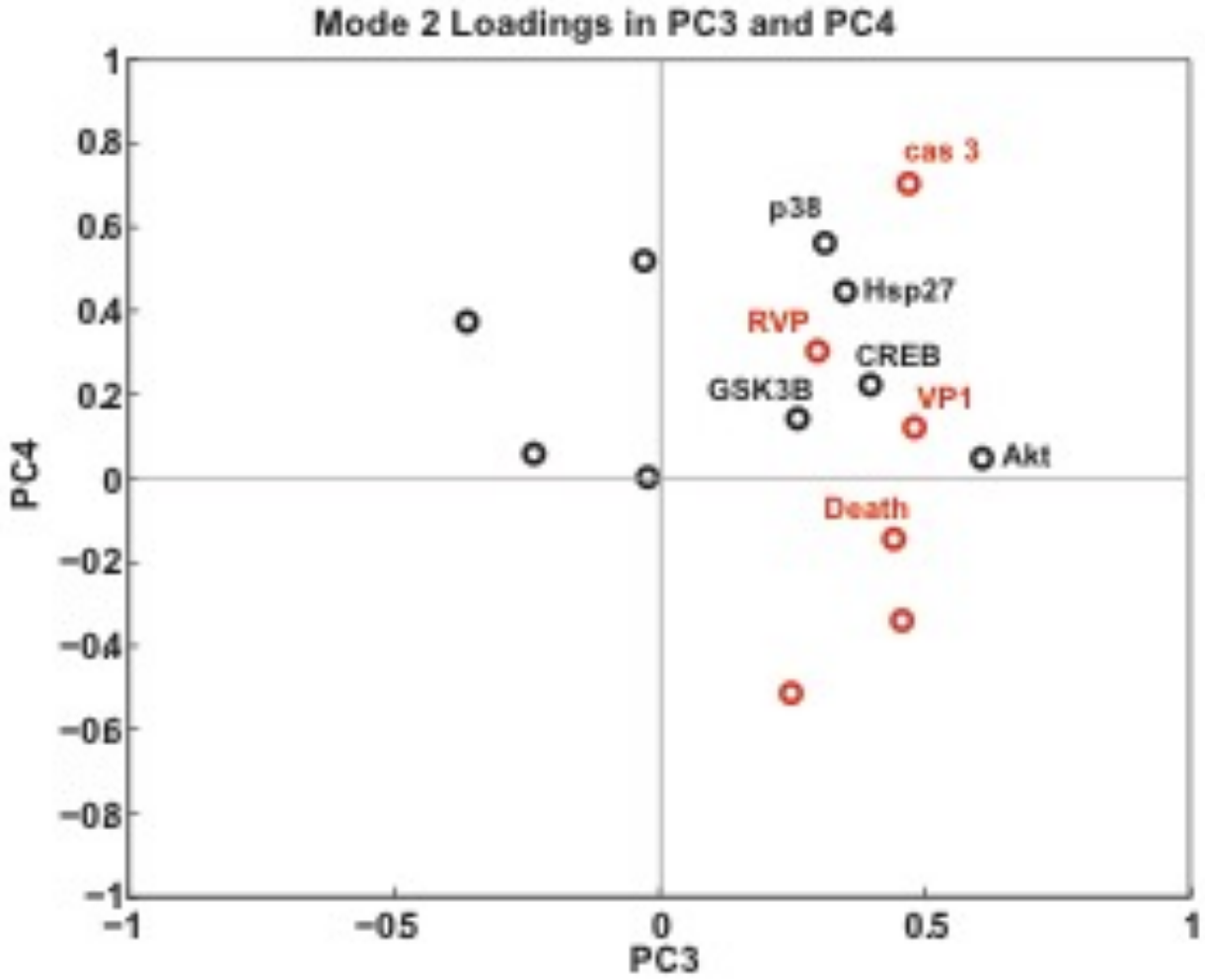

Figure 8. Visualization of phosphoprotein and cellular output data in principal component space.

Phosphoprotein (mode 2 of predictor tensor, black) and cellular output (mode 2 of output tensor, red) loadings are mapped in principal component space to show clusters with similar loadings in each PC. Loadings and PCs were generated using a four component PLS model.

4.5. Concluding remarks

Will the age-old methods of SVD, PCA, and PLSR become obsolete in the midst of this new era of biomedical Big Data? We have many reasons to think not. First, the statistical models introduced in this chapter are among the simplest linear methods for reducing complex datasets. Invoking Occam's razor, these models should be proved to be insufficient before more-complicated alternatives are sought. Simple models are more-easily interpretable—by generating principal components that can be immediately mapped back onto the primary data, the models stay grounded in what they were derived from. Statistical models therefore avoid the pitfalls of machine-learning approaches, such as support-vector machines and neural networks, which can make remarkable predictions but leave the user confused about how the predictions were made (48, 49).

Second, the iterative methods for PCA and PLSR are very scalable to large datasets, because they do not require calculating the covariance matrix as with older implementations of SVD. To circumvent problems interpreting PCs with many variables, there are sparse variants that use different constraints to generate PCs with more-limited mixtures of the original variables (50). The computational simplicity allows model stability be easily assessed by standard numerical methods such as cross validation, bootstrapping, and permutation (51). Statistical models thus provide a direct indication of their uncertainty based upon the data provided, which stands in contrast to physico-chemical models where uncertainty can be more cryptic (52).

Last and most important, even if the methods here are eventually supplanted by superior alternatives, they nonetheless serve as an important entry point for those interested in statistical modeling. Biologists are already accustomed to looking at their results—statistical models provide a more-formal way of inspecting complex data and illustrating the power of computation in real terms (53). Just as it is difficult to imagine life now without a computer or a smartphone, biological research will soon become unfathomable without the aid of statistical models.

4.6. References:

1. Schoeberl, B., Eichler-Jonsson, C., Gilles, E. D., and Muller, G. (2002) Computational modeling of the dynamics of the MAP kinase cascade activated by surface and internalized EGF receptors. *Nat Biotechnol* 20, 370-375
2. Hoffmann, A., Levchenko, A., Scott, M. L., and Baltimore, D. (2002) The IkappaB-NF-kappaB signaling module: temporal control and selective gene activation. *Science* 298, 1241-1245
3. Chen, W. W., Schoeberl, B., Jasper, P. J., Niepel, M., Nielsen, U. B., Lauffenburger, D. A., and Sorger, P. K. (2009) Input-output behavior of ErbB signaling pathways as revealed by a mass action model trained against dynamic data. *Mol Syst Biol* 5, 239
4. Albeck, J. G., Burke, J. M., Spencer, S. L., Lauffenburger, D. A., and Sorger, P. K. (2008) Modeling a snap-action, variable-delay switch controlling extrinsic cell death. *PLoS Biol* 6, 2831-2852
5. Wiley, H. S., Shvartsman, S. Y., and Lauffenburger, D. A. (2003) Computational modeling of the EGF-receptor system: a paradigm for systems biology. *Trends Cell Biol* 13, 43-50
6. Nakakuki, T., Birtwistle, M. R., Saeki, Y., Yumoto, N., Ide, K., Nagashima, T., Brusch, L., Ogunnaike, B. A., Okada-Hatakeyama, M., and Kholodenko, B. N. (2010) Ligand-specific c-Fos expression emerges from the spatiotemporal control of ErbB network dynamics. *Cell* 141, 884-896
7. Saez-Rodriguez, J., Alexopoulos, L. G., Epperlein, J., Samaga, R., Lauffenburger, D. A., Klamt, S., and Sorger, P. K. (2009) Discrete logic modelling as a means to link protein signalling networks with functional analysis of mammalian signal transduction. *Mol Syst Biol* 5, 331
8. Aldridge, B. B., Saez-Rodriguez, J., Muhlich, J. L., Sorger, P. K., and Lauffenburger, D. A. (2009) Fuzzy logic analysis of kinase pathway crosstalk in TNF/EGF/insulin-induced signaling. *PLoS Comput Biol* 5, e1000340
9. Janes, K. A., and Lauffenburger, D. A. (2006) A biological approach to computational models of proteomic networks. *Curr Opin Chem Biol* 10, 73-80
10. Janes, K. A., and Yaffe, M. B. (2006) Data-driven modelling of signal-transduction networks. *Nat Rev Mol Cell Biol* 7, 820-828
11. Gaudet, S., Janes, K. A., Albeck, J. G., Pace, E. A., Lauffenburger, D. A., and Sorger, P. K. (2005) A Compendium of Signals and Responses Triggered by Prodeath and Prosurvival Cytokines. *Mol Cell Proteomics* 4, 1569-1590
12. Albeck, J. G., MacBeath, G., White, F. M., Sorger, P. K., Lauffenburger, D. A., and Gaudet, S. (2006) Collecting and organizing systematic sets of protein data. *Nat Rev Mol Cell Biol* 7, 803-812
13. Vilela, M., and Danuser, G. (2011) What's wrong with correlative experiments? *Nat Cell Biol* 13, 1011
14. Jensen, K. J., and Janes, K. A. (2012) Modeling the latent dimensions of multivariate signaling datasets. *Phys Biol* 9, 045004
15. Alter, O. (2007) Genomic signal processing: from matrix algebra to genetic networks. *Methods in molecular biology* 377, 17-60
16. Spellman, P. T., Sherlock, G., Zhang, M. Q., Iyer, V. R., Anders, K., Eisen, M. B., Brown, P. O., Botstein, D., and Futcher, B. (1998) Comprehensive identification of cell cycle-regulated

genes of the yeast Saccharomyces cerevisiae by microarray hybridization. *Molecular biology of the cell* 9, 3273-3297
17. Janes, K. A., Albeck, J. G., Gaudet, S., Sorger, P. K., Lauffenburger, D. A., and Yaffe, M. B. (2005) A systems model of signaling identifies a molecular basis set for cytokine-induced apoptosis. *Science* 310, 1646-1653
18. Jolliffe, I. T. (2002) Principal Component Analysis. *Springer Series in Statistics*
19. Pearson, K. (1901) On Lines and Planes of Closest Fit to Systems of Points in Space. *Philosphical Magazine* 2, 559-572
20. Martens, H., and Martens, M. (2001) Analysis of One Data Table X: Principal Component Analysis. *Multivariate Analysis of Quality: An Introduction*, 1st Ed., pp. 93-110, Wiley
21. Jeffers, J. (1967) Two Case Studies in the Application of Principal Component Analysis. *Journal of the Royal Statistical Society* 16, 225-236
22. Crescenzi, M., and Giuliani, A. (2001) The main biological determinants of tumor line taxonomy elucidated by a principal component analysis of microarray data. *FEBS letters* 507, 114-118
23. Hu, J., Locasale, J. W., Bielas, J. H., O'Sullivan, J., Sheahan, K., Cantley, L. C., Vander Heiden, M. G., and Vitkup, D. (2013) Heterogeneity of tumor-induced gene expression changes in the human metabolic network. *Nature biotechnology* 31, 522-529
24. Misra, J., Schmitt, W., Hwang, D., Hsiao, L. L., Gullans, S., Stephanopoulos, G., and Stephanopoulos, G. (2002) Interactive exploration of microarray gene expression patterns in a reduced dimensional space. *Genome research* 12, 1112-1120
25. Schlens, J. (2003) A Tutorial On Principal Component Analysis: Derivation, Discussion, and Singular Value Decomposition. .
26. Jensen, K. J., Garmaroudi, F. S., Zhang, J., Lin, J., Boroomand, S., Zhang, M., Luo, Z., Yang, D., Luo, H., McManus, B. M., and Janes, K. A. (2013) An ERK-p38 subnetwork coordinates host cell apoptosis and necrosis during coxsackievirus B3 infection. *Cell Host Microbe* 13, 67-76
27. Whitton, J. L., Cornell, C. T., and Feuer, R. (2005) Host and virus determinants of picornavirus pathogenesis and tropism. *Nature reviews. Microbiology* 3, 765-776
28. Esfandiarei, M., and McManus, B. M. (2008) Molecular biology and pathogenesis of viral myocarditis. *Annu Rev Pathol* 3, 127-155
29. Tucker, L. R. (1966) Some mathematical notes on three-mode factor analysis. *Psychometrika* 31, 279-311
30. Carroll, J. D., Chang, J. J. (1970) Analysis of individual differences in multidimensional scaling via an N-way generalization of 'Eckart-Young' decomposition. *Psychometrika* 35, 283-319
31. Kolda, T. G., Bader, B. B. (2007) Tensor Decompositions and Applications *Sandia National Laboratories Report* SAND2007-6702
32. Bro, R. (1997) PARAFAC. Tutorial and applications. *Chemometrics and intelligent laboratory systems* 38, 149-171
33. Bro, R., Kiers, H. A. L. (2003) A new efficient method for determining the number of components in PARAFAC models. *Journal of Chemometrics* 17, 274-286
34. Alter, O., Brown, P. O., and Botstein, D. (2000) Singular value decomposition for genome-wide expression data processing and modeling. *Proc Natl Acad Sci U S A* 97, 10101-10106

35. Lau, K. S., Juchheim, A. M., Cavaliere, K. R., Philips, S. R., Lauffenburger, D. A., and Haigis, K. M. (2011) In vivo systems analysis identifies spatial and temporal aspects of the modulation of TNF-alpha-induced apoptosis and proliferation by MAPKs. *Sci Signal* 4, ra16
36. Lee, M. J., Ye, A. S., Gardino, A. K., Heijink, A. M., Sorger, P. K., Macbeath, G., and Yaffe, M. B. (2012) Sequential application of anticancer drugs enhances cell death by rewiring apoptotic signaling networks. *Cell* 149, 780-794
37. Miller-Jensen, K., Janes, K. A., Brugge, J. S., and Lauffenburger, D. A. (2007) Common effector processing mediates cell-specific responses to stimuli. *Nature* 448, 604-608
38. Kreeger, P. K., Mandhana, R., Alford, S. K., Haigis, K. M., and Lauffenburger, D. A. (2009) RAS mutations affect tumor necrosis factor-induced apoptosis in colon carcinoma cells via ERK-modulatory negative and positive feedback circuits along with non-ERK pathway effects. *Cancer Res* 69, 8191-8199
39. Tentner, A. R., Lee, M. J., Ostheimer, G. J., Samson, L. D., Lauffenburger, D. A., and Yaffe, M. B. (2012) Combined experimental and computational analysis of DNA damage signaling reveals context-dependent roles for Erk in apoptosis and G1/S arrest after genotoxic stress. *Mol Syst Biol* 8, 568
40. Kumar, N., Wolf-Yadlin, A., White, F. M., and Lauffenburger, D. A. (2007) Modeling HER2 effects on cell behavior from mass spectrometry phosphotyrosine data. *PLoS Comput Biol* 3, e4
41. Kumar, D., Srikanth, R., Ahlfors, H., Lahesmaa, R., and Rao, K. V. (2007) Capturing cell-fate decisions from the molecular signatures of a receptor-dependent signaling response. *Mol Syst Biol* 3, 150
42. Beyer, E. M., and MacBeath, G. (2012) Cross-talk between receptor tyrosine kinase and tumor necrosis factor-alpha signaling networks regulates apoptosis but not proliferation. *Mol Cell Proteomics* 11, M111 013292
43. Kemp, M. L., Wille, L., Lewis, C. L., Nicholson, L. B., and Lauffenburger, D. A. (2007) Quantitative network signal combinations downstream of TCR activation can predict IL-2 production response. *J Immunol* 178, 4984-4992
44. Dworkin, M., Mukherjee, S., Jayaprakash, C., and Das, J. (2012) Dramatic reduction of dimensionality in large biochemical networks owing to strong pair correlations. *J R Soc Interface* 9, 1824-1835
45. Kreeger, P. K. (2013) Using partial least squares regression to analyze cellular response data. *Sci Signal* 6, tr7
46. Geladi, P., and Kowalski, B. R. (1986) Partial Least-Squares Regression - a Tutorial. *Anal Chim Acta* 185, 1-17
47. Andersson, C. A., and Bro, R. (2000) The N-way Toolbox for MATLAB. *Chemometr Intell Lab Syst* 52, 1-4
48. Noble, W. S. (2006) What is a support vector machine? *Nat Biotechnol* 24, 1565-1567
49. Krogh, A. (2008) What are artificial neural networks? *Nat Biotechnol* 26, 195-197
50. Zou, H., Hastie, T., and Tibshirani, R. (2006) Sparse principal component analysis. *J Comput Graph Stat* 15, 265-286
51. Efron, B., and Tibshirani, R. J. (1993) *An Introduction to the Bootstrap*, Chapman and Hall, London
52. Gutenkunst, R. N., Waterfall, J. J., Casey, F. P., Brown, K. S., Myers, C. R., and Sethna, J. P. (2007) Universally sloppy parameter sensitivities in systems biology models. *PLoS Comput Biol* 3, 1871-1878

53. Janes, K. A., and Lauffenburger, D. A. (2013) Models of signalling networks - what cell biologists can gain from them and give to them. *Journal of cell science* 126, 1913-1921

Chapter 5:

Comparing AC16 and stem cell derived cardiomyocytes as an in vitro model to study CVB3 infection

Millie Shah and Kevin Janes

Department of Biomedical Engineering, University of Virginia, Charlottesville, VA, 22908

5.1. Introduction

Understanding CVB3-cardiomyocyte interactions at the signaling level relies upon an accurate in vitro model system. Advances in induced-pluripotent stem cell (iPSC) technology have provided researchers with the ability to generate and culture cardiac myocytes from human donors in a dish (1). These iPSC-derived cardiomyocytes (iPSC-CM) have become the gold-standard for human cardiomyocytes in vitro because of their recapitulation of essential cardiac functions including synchronous beating and stimulus-induced hypertrophy (2-5). By comparison, AC16 cells do not display these phenotypes, although initial validation shows that they retain some cardiac characteristics (Chapter 3.1) (6). A holistic analysis of AC16 cardiomyocyte fidelity has yet to be done. To determine what aspects of cardiac biology are conserved in AC16 cells we compared their transcriptome to iPSC-CMs. Further, because iPSC-CMs have only been used to model acute cardiac CVB3 infection (7), we will investigate the utility of human iPSC-CMs as a model system for chronic CVB3 infection.

Using RNA-seq, we profile the transcriptomes of quiescent AC16 cells and iPSC-CMs. We found that overall, iPSC-CMs differ from AC16 cells mainly in structural and contraction related cardiac markers. We also measure transcriptomic changes induced by CVB3 infection in both cell models. We found that AC16 cells and iPSC-CMs share some responses characteristic of CVB3 infection in vivo though AC16 cells have a more proinflammatory response while iPSC-CMs have a growth and hypertrophy response. We conclude with a discussion of using mutated CVB3 virions to model chronic infection in iPSC-CMs.

5.2. Results

To compare AC16 cells and iPSC-CMs as cardiomyocyte models of CVB3 infection we conducted RNA sequencing on both uninfected and infected cells. We used two types of viruses, wild type CVB3 and a mutated virus $CVB3_{\Delta VP0}$ which will be discussed later. Additionally, we used iPSC-CMs after 2 days of culture (iPSC-2D) before syncytial formation (asynchronous beating) as well as

after 4 days of culture when syncytia had formed and cells were beating in synchrony. We first wanted to look at transcript expression in these cells with and without infection (Figure 1A). We focused on genes that were highly expressed in at least one sample. Overall, iPSC-CMs and AC16 cells had different transcriptomic signatures under all conditions. This may be partially due to differences in human donors and culture conditions. However, the most differentially expressed genes (ranked by |log2(fold change)|) were predominately involved in cardiac contractile function (Figure 1B). This is consistent with previous work characterizing AC16s showing that while they express contractile proteins, they do not have organized sarcomeres and do not contract (6).

Interestingly, syncytial iPSC-CMs (iPSC-4D) had very similar expression patterns to non-syncytial iPSC-2D cells (Figure 2A). This suggests that phenotypic differences, like synchronous beating, between syncytial and non-syncytial iPSCs are likely due to the maturation of cell-cell contacts and gap junctions. Despite phenotypic differences, syncytial and non-syncytial iPSCs have similar gene-expression programs in the context of infection (Figure 2B & C). Thus, further analysis between AC16 and iPSC-CMs was done with iPSC-4D data.

We next wanted to determine whether AC16 cells and iPSC-CMs responded the same way to coxsackievirus infection. Cells were infected with an MOI of 10 and RNA collected 8 hours post infection. This time point was chosen because after 8 hours, iPSC-CM display overt cytopathic effects consistent with a previous model of CVB3 infection (7). At 8 hours post infection we saw loss of beating in iPSC-CM and were able to detect viral protein expression in AC16-CAR cells (data not shown). For each cell line we compared transcript expression between infected and uninfected cells. Differential gene expression for each contrast was assessed as at least a 1.5-fold change in expression with a FDR of less than 10%. Then, differential gene lists for each cell line were filtered for genes that were shared. We found subsets of correlated gene changes and anti-correlated gene changes (Figure 3). Correlated gene changes were consistent with aspects of CVB3 infection including upregulation of thrombospondin 1 (THSB1) and immediate early gene 1 (IER3). CVB3-mediated ERK hyperactivation induces immediate early transcriptional responses (8). Similarly, thrombospondin 1 is likely induced in

response to ER-stress caused by CVB3 replication centers (9). Interestingly, AC16-CAR cells induced expression of proiflammatory cytokines known to be produced during CVB3 infection such as IL1β, IL6, and CCL2, while iPSC-CMs did not (10, 11). By contrast, iPSC-CMs uniquely upregulated many genes downstream of ERK hyperactivation such as phosphatase DUSP6 (12, 13). Additionally, immediate early genes, early growth response (EGR1-3) and transcription factor c-fos as well as cardiac hormone natriuretic peptide B were upregulated which have been implicated in cardiac growth and heart failure respectively (14-18). The response may indicate ERK-mediated pathological growth consistent with CVB3 infection in vivo (19). Overall, both AC16-CAR and iPSC-CMs capture aspects of CVB3 infection with AC16-CARs recapitulating inflammatory processes while iPSC-CMs displaying growth related gene expression.

To attempt to model chronic infection in iPSC-CMs we generated CVB3 virions loaded with CVB3ΔVP0 genomes ($CVB3_{\Delta VP0}$). Because iPSC-CMs are terminally differentiated, the cloning method presented in Chapter 3 for chronic CVB3 modeling would not be possible as this requires actively proliferating cells. Instead, we generated virus particles that would efficiently deliver the same mutated CVB3 genome to iPSC-CMs while still precluding generation of viral progeny. As before, these genomes retain the ability to produce viral proteins and replicate. We infected iPSC-2D, iPSC-4D, and AC16-CAR cells with $CVB3_{\Delta VP0}$ at an MOI of ~3 for 16 hours. At this time point, we found that transcriptional programs in all three cell lines were highly correlated with those induced by live CVB3 (Figure 4). This suggests that responses to $CVB3_{\Delta VP0}$ may be associated with viral entry and early viral replication, processes which are the same in acute infection. This is consistent with the observed onset of cytopathic effects (loss of beating, cell apoptosis) in iPSC-CMs at 16 hours post infection. This delayed onset compared to live CVB3 infection is likely due to a lack of reinfection events. It was previously shown that at an MOI of 5, iPSC-CMs express copious amounts of viral proteins 6 hours post infection (7). This suggests that viral progeny release and reinfection events can take place before 10 hours post infection and accelerate the on-set of cytopathic effects. In our $CVB3_{\Delta VP0}$ model, the lack

of viral progeny release likely delays cell death. Nonetheless, this model does not provide us with chronic infection specific information as cytopathic effects prevent longer timescale studies.

A

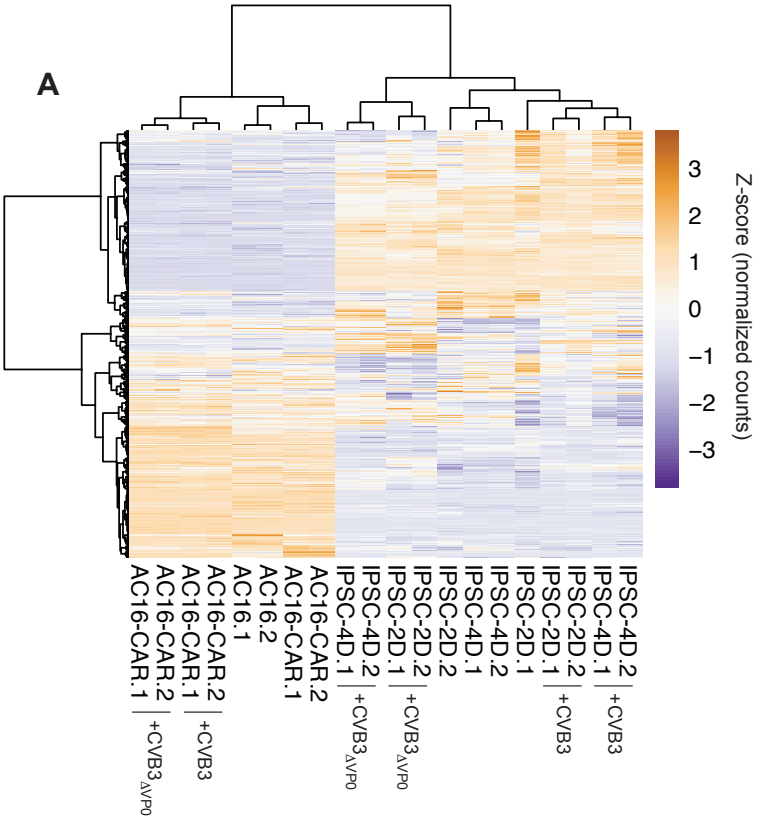

B

Database	Term	DE Genes (#)	% of term genes	FDR
BP_DIRECT	GO:0060048 cardiac muscle contraction	15	7.58	1.63E-14
BP_DIRECT	GO:0030049 muscle filament sliding	13	6.57	3.03E-12
BP_DIRECT	GO:0055010 ventricular cardiac muscle tissue morphogenesis	9	4.55	1.54E-07
KEGG	hsa04260 Cardiac muscle contraction	9	4.55	8.75E-04
BP_DIRECT	GO:0002026 regulation of the force of heart contraction	6	3.03	1.8E-03

Figure 1. Transcriptomic analysis of AC16 and iPSC-CM
A. Heatmap of normalized read counts for each sample including replicates. Columns and rows were clustered using Ward's method. Read counts were filtered for genes with at least 1000 reads in at least one sample. B. GSEA on 200 most differentially expressed genes ranked by $|\log_2(\text{fold change})|$.

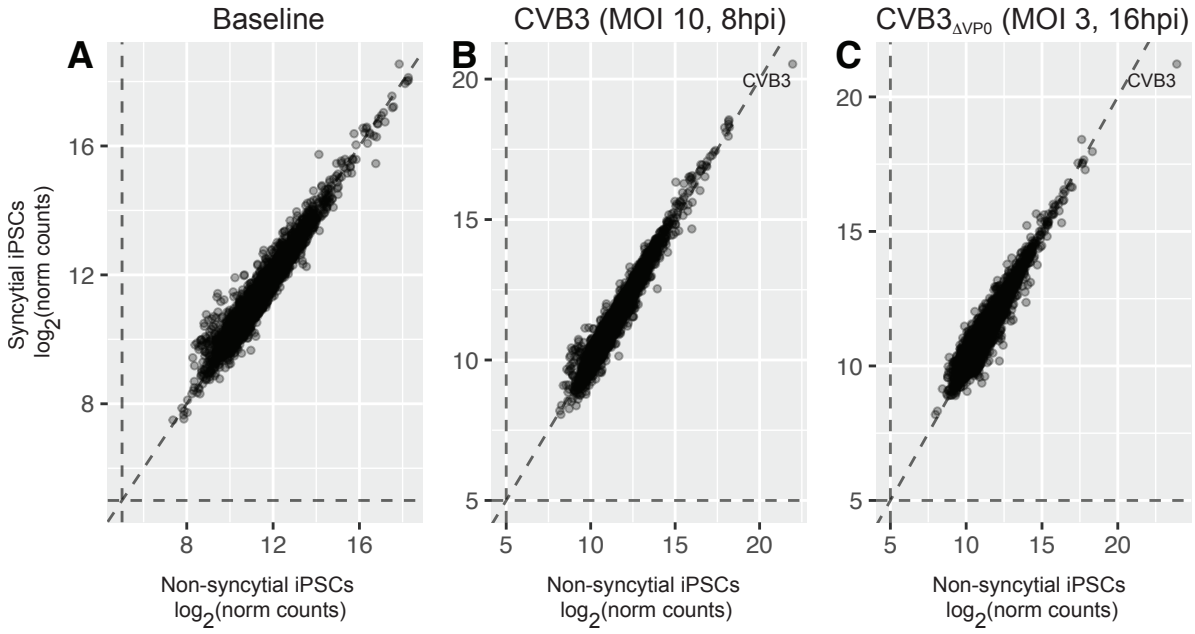

Figure 2. Gene expression programs in syncytial and non-syncytial iPSC-CMs are conserved
Log2-transformed normalized read counts for abundant genes expressed by syncytial and non-syncytial cells at baseline (A), with CVB3 infection (B), and with mutant $CVB3_{\Delta VP0}$ infection (C).

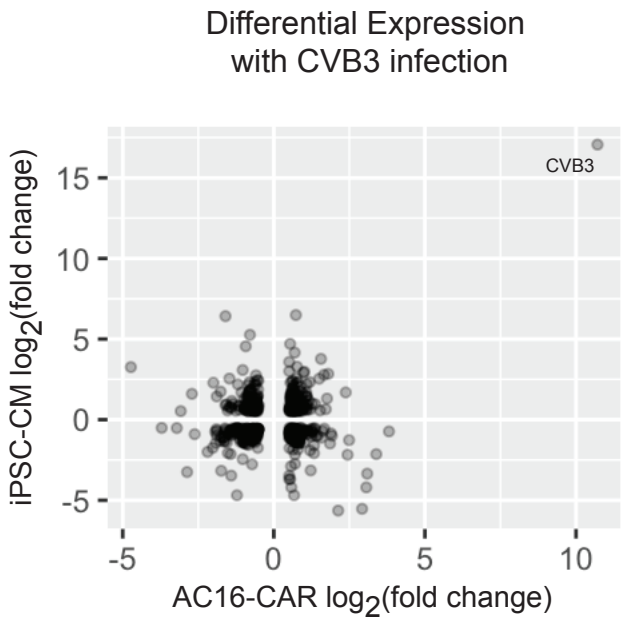

Figure 3. Infection induced differential gene expression in AC16-CAR versus iPSC-CMs
Each point corresponds to the $\log_2$(fold change from uninfected) of a gene. X-axis corresponds to changes observed in AC16-CAR cells and the Y-axis corresponds to changes observed in iPSC-CMs. Only genes that were significantly altered with FDR < 0.1 and |log2(fold change)| > 0.5 in both iPSC-CMs and AC16-CAR cells are plotted. Cells were infected with an MOI of 10 and lysed after 8hrs of infection.

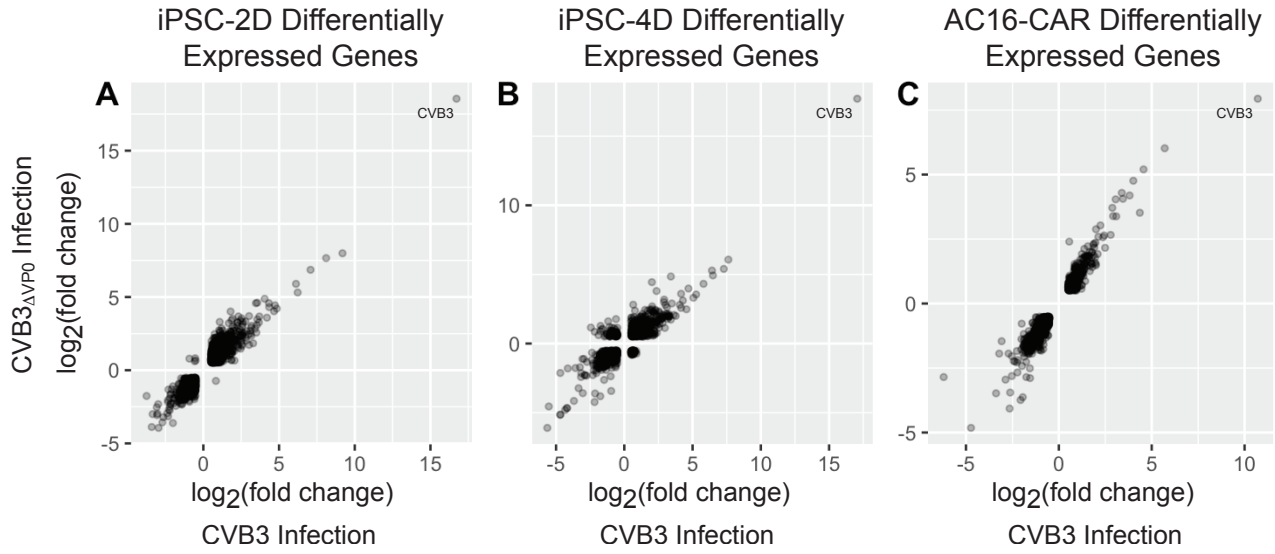

Figure 4. Consistent differential gene expression post-infection with live CVB3 and CVB3$_{\Delta VP0}$
Each point corresponds to the log_2(fold change from uninfected) of a gene in iPSC-2D (A.), iPSC-4D (B.) and AC16-CAR cells (C.). All genes meet FDR < 0.1 and |log2(fold change)| > 0.5 cut offs.

5.3. Discussion

Through transcriptomic studies, we have found that AC16 cells and iPSC-CMs differ mainly in their contractile capacity. Further, we find some shared and some unique responses to CVB3 infection. These responses suggest that iPSC-CM are a useful model for studying structural changes resulting from CVB3 infection, while AC16 cells maybe a better model for studying inflammatory responses to CVB3 infection. The latter is predicated on in vivo studies showing increases in cardiac localized inflammatory cytokines or mRNA from whole cardiac tissue (10, 20). While the majority of cardiac volume is occupied by myocytes, other cells types including cardiac fibroblasts and tissue resident immune cells are present in non-negligible numbers (21). Fibroblasts and monocytes are both susceptible to CVB3 infection and fibroblasts maintain carrier state infections (22, 23). These cell types contribute to immune-related phenotypes during acute infection but their role in chronic infection, where virion production is not detected, is unclear. With the emergence of new high-throughput in situ methods for measuring mRNA, it would be interesting to quantify cell-type specific cytokine gene induction within acutely infected and chronically infected hearts in animal models of infection (24). Such data would help assess the fidelity of both iPSC-CM and AC16 models of CVB3 infection.

Modeling chronic infection in iPSC-CM presents a challenge. A previous study by Sharma et. al 2014 showed that iPSC-CM infection with single-digit virus particles (MOI ~ 10^{-5}) leads to apoptosis in all cells by 120 hours post infection. This precludes the possibility of long-term chronic infections beginning from acute infection. Delivery of $CVB3_{\Delta VP0}$ to iPSC-CM induces similar transcriptomic and cytopathic effects as live CVB3 infection likely because of high replication rates and viral load of mutated CVB3 genomes. One alternative to this approach could be to deliver a replication-restricted, 5' terminally deleted CVB3 genome instead. Without a complete 5' terminus, CVB3 replication complexes are inefficiently assembled (25, 26). This limits viral nucleic acid copying but, importantly, does not affect viral protein translation. Such genomes have been isolated from a chronically infected patient and may represent a more realistic chronic model (27).

5.4. Methods

iPSC-CM Cell Culture

iCell-Cardiomyocytes^2 were obtained from Cellular Dynamics International (#R1017, CDI, Madison, WI) and cultured to manufacturer's specifications. Cells were plated in 12-well dishes at ~ 600,000 cells/well and cultured for either 2 days (asynchronous beating) or 4 days (syncytial formation and synchronous beating). RNA extraction and CVB3 infection was conducted at both 2 days and 4 days post-plating.

Generation of packaging-deficient CVB3 virions ($CVB3_{\Delta VP0}$)

CVB3 virions loaded with packaging-deficient CVB3ΔVP0 genomes were generated by co-transfection of 293T HEK cells with plasmids carrying the mutated genome sequence and the wild-type VP0 capsid sequence. DNA-liposome complexes were created using Lipofectamine 2000 and pcDNA3-CVB3DVP0 and pcDNA3-VP0wt plasmids. Cells where lipofected according to manufacturer's recommendation and $CVB3_{\Delta VP0}$ virions were collected in culture media supernatants 72hrs later. Cellular debris were removed from supernatants by gentle centrifugation at 1000 gs for 5 minutes. To concentrate viral stocks, clarified media supernatants were spun down at 100,000 gs for 1hr at 4°C and resuspended in DMEM/F12 (+1% pen/strep) or iCell-Cardiomyocytes^2 maintenance media.

CVB3 and $CVB3_{\Delta VP0}$ Infection

Quiescent AC16-CAR cells were cultured and infected as previously described (Chapter 2.4 and Chapter 3.4). iCell-Cardiomyocytes^2 were infected by gently washing with 500 uL of maintenance media followed by addition of 300 uL of virus containing maintenance media. Infection was incubated for 1 hour before gently washing with 500 uL of maintenance media and refeeding with 1000 uL of maintenance media. Both AC16-CAR and iCell-Cardiomyocytes^2 were infected with live CVB3 at MOI

of 10 and $CVB3_{\Delta VP0}$ at an MOI of ~3. RNA from live CVB3 infections were collected at 8 hours post infection. RNA from $CVB3_{\Delta VP0}$ infections were collected at 16 hours post infection.

RNA-seq

RNA samples were prepped and RNA-seq was conducted as previously described (Chapter 3.4). Gene set enrichment analysis (GSEA) was performed using DAVID (https://david.ncifcrf.gov/ (28, 29). Genes differentially expressed between iCell-Cardiomyocytes[2] (4 days of culture) and AC16 cells were filtered for FDR > 0.05 and |log2(fold change)| > 0.5. The top 100 upregulated genes and top 100 downregulated genes were used for GSEA.

5.5. References

1. Yu, J., Vodyanik, M. A., Smuga-Otto, K., Antosiewicz-Bourget, J., Frane, J. L., Tian, S., Nie, J., Jonsdottir, G. A., Ruotti, V., Stewart, R., Slukvin, I. I., and Thomson, J. A. (2007) Induced pluripotent stem cell lines derived from human somatic cells. *Science* 318, 1917-1920
2. Cameron, B. J., Gerry, A. B., Dukes, J., Harper, J. V., Kannan, V., Bianchi, F. C., Grand, F., Brewer, J. E., Gupta, M., Plesa, G., Bossi, G., Vuidepot, A., Powlesland, A. S., Legg, A., Adams, K. J., Bennett, A. D., Pumphrey, N. J., Williams, D. D., Binder-Scholl, G., Kulikovskaya, I., Levine, B. L., Riley, J. L., Varela-Rohena, A., Stadtmauer, E. A., Rapoport, A. P., Linette, G. P., June, C. H., Hassan, N. J., Kalos, M., and Jakobsen, B. K. (2013) Identification of a Titin-derived HLA-A1-presented peptide as a cross-reactive target for engineered MAGE A3-directed T cells. *Sci Transl Med* 5, 197ra103
3. Aggarwal, P., Turner, A., Matter, A., Kattman, S. J., Stoddard, A., Lorier, R., Swanson, B. J., Arnett, D. K., and Broeckel, U. (2014) RNA expression profiling of human iPSC-derived cardiomyocytes in a cardiac hypertrophy model. *PLoS ONE* 9, e108051
4. Drawnel, F. M., Boccardo, S., Prummer, M., Delobel, F., Graff, A., Weber, M., Gérard, R., Badi, L., Kam-Thong, T., Bu, L., Jiang, X., Hoflack, J.-C., Kiialainen, A., Jeworutzki, E., Aoyama, N., Carlson, C., Burcin, M., Gromo, G., Boehringer, M., Stahlberg, H., Hall, B. J., Magnone, M. C., Kolaja, K., Chien, K. R., Bailly, J., and Iacone, R. (2014) Disease modeling and phenotypic drug screening for diabetic cardiomyopathy using human induced pluripotent stem cells. *Cell Rep* 9, 810-821
5. Ma, J., Guo, L., Fiene, S. J., Anson, B. D., Thomson, J. A., Kamp, T. J., Kolaja, K. L., Swanson, B. J., and January, C. T. (2011) High purity human-induced pluripotent stem cell-derived cardiomyocytes: electrophysiological properties of action potentials and ionic currents. *Am. J. Physiol. Heart Circ. Physiol.* 301, H2006-2017
6. Davidson, M. M., Nesti, C., Palenzuela, L., Walker, W. F., Hernandez, E., Protas, L., Hirano, M., and Isaac, N. D. (2005) Novel cell lines derived from adult human ventricular cardiomyocytes. *J. Mol. Cell. Cardiol.* 39, 133-147
7. Sharma, A., Marceau, C., Hamaguchi, R., Burridge, P. W., Rajarajan, K., Churko, J. M., Wu, H., Sallam, K. I., Matsa, E., Sturzu, A. C., Che, Y., Ebert, A., Diecke, S., Liang, P., Red-Horse, K., Carette, J. E., Wu, S. M., and Wu, J. C. (2014) Human induced pluripotent stem cell-derived cardiomyocytes as an in vitro model for coxsackievirus B3-induced myocarditis and antiviral drug screening platform. *Circ. Res.* 115, 556-566
8. Sgambato, V., Pagès, C., Rogard, M., Besson, M. J., and Caboche, J. (1998) Extracellular signal-regulated kinase (ERK) controls immediate early gene induction on corticostriatal stimulation. *J. Neurosci.* 18, 8814-8825
9. Lynch, J. M., Maillet, M., Vanhoutte, D., Schloemer, A., Sargent, M. A., Blair, N. S., Lynch, K. A., Okada, T., Aronow, B. J., Osinska, H., Prywes, R., Lorenz, J. N., Mori, K., Lawler, J., Robbins, J., and Molkentin, J. D. (2012) A thrombospondin-dependent pathway for a protective ER stress response. *Cell* 149, 1257-1268
10. Glück, B., Schmidtke, M., Merkle, I., Stelzner, A., and Gemsa, D. (2001) Persistent expression of cytokines in the chronic stage of CVB3-induced myocarditis in NMRI mice. *J. Mol. Cell. Cardiol.* 33, 1615-1626
11. Rehren, F., Ritter, B., Dittrich-Breiholz, O., Henke, A., Lam, E., Kati, S., Kracht, M., and Heim, A. (2013) Induction of a broad spectrum of inflammation-related genes by Coxsackievirus B3 requires Interleukin-1 signaling. *Med. Microbiol. Immunol.* 202, 11-23

12. Kondoh, K., and Nishida, E. (2007) Regulation of MAP kinases by MAP kinase phosphatases. *Biochim. Biophys. Acta* 1773, 1227-1237
13. Sarközi, R., Miller, B., Pollack, V., Feifel, E., Mayer, G., Sorokin, A., and Schramek, H. (2007) ERK1/2-driven and MKP-mediated inhibition of EGF-induced ERK5 signaling in human proximal tubular cells. *J. Cell. Physiol.* 211, 88-100
14. Sadoshima, J., Takahashi, T., Jahn, L., and Izumo, S. (1992) Roles of mechano-sensitive ion channels, cytoskeleton, and contractile activity in stretch-induced immediate-early gene expression and hypertrophy of cardiac myocytes. *Proc. Natl. Acad. Sci. U.S.A.* 89, 9905-9909
15. Neyses, L., Nouskas, J., Luyken, J., Fronhoffs, S., Oberdorf, S., Pfeifer, U., Williams, R. S., Sukhatme, V. P., and Vetter, H. (1993) Induction of immediate-early genes by angiotensin II and endothelin-1 in adult rat cardiomyocytes. *J. Hypertens.* 11, 927-934
16. Lijnen, P., and Petrov, V. (1999) Renin-angiotensin system, hypertrophy and gene expression in cardiac myocytes. *J. Mol. Cell. Cardiol.* 31, 949-970
17. Cowie, M. R., and Mendez, G. F. (2002) BNP and congestive heart failure. *Prog Cardiovasc Dis* 44, 293-321
18. Murphy, L. O., Smith, S., Chen, R. H., Fingar, D. C., and Blenis, J. (2002) Molecular interpretation of ERK signal duration by immediate early gene products. *Nat Cell Biol* 4, 556-564
19. Huber, M., Watson, K. A., Selinka, H. C., Carthy, C. M., Klingel, K., McManus, B. M., and Kandolf, R. (1999) Cleavage of RasGAP and phosphorylation of mitogen-activated protein kinase in the course of coxsackievirus B3 replication. *J. Virol.* 73, 3587-3594
20. Satoh, M., Tamura, G., Segawa, I., Tashiro, A., Hiramori, K., and Satodate, R. (1996) Expression of cytokine genes and presence of enteroviral genomic RNA in endomyocardial biopsy tissues of myocarditis and dilated cardiomyopathy. *Virchows Arch.* 427, 503-509
21. MacKenna, D., Summerour, S. R., and Villarreal, F. J. (2000) Role of mechanical factors in modulating cardiac fibroblast function and extracellular matrix synthesis. *Cardiovasc. Res.* 46, 257-263
22. Henke, A., Mohr, C., Sprenger, H., Graebner, C., Stelzner, A., Nain, M., and Gemsa, D. (1992) Coxsackievirus B3-induced production of tumor necrosis factor-alpha, IL-1 beta, and IL-6 in human monocytes. *The Journal of Immunology* 148, 2270-2277
23. Heim, A., Canu, A., Kirschner, P., Simon, T., Mall, G., Hofschneider, P. H., and Kandolf, R. (1992) Synergistic interaction of interferon-beta and interferon-gamma in coxsackievirus B3-infected carrier cultures of human myocardial fibroblasts. *J. Infect. Dis.* 166, 958-965
24. Moffitt, J. R., Hao, J., Wang, G., Chen, K. H., Babcock, H. P., and Zhuang, X. (2016) High-throughput single-cell gene-expression profiling with multiplexed error-robust fluorescence in situ hybridization. *Proc. Natl. Acad. Sci. U.S.A.* 113, 11046-11051
25. Sharma, N., Ogram, S. A., Morasco, B. J., Spear, A., Chapman, N. M., and Flanegan, J. B. (2009) Functional role of the 5' terminal cloverleaf in Coxsackievirus RNA replication. *Virology* 393, 238-249
26. Lévêque, N., Garcia, M., Bouin, A., Nguyen, J. H. C., Tran, G. P., Andreoletti, L., and Semler, B. L. (2017) Functional Consequences of RNA 5'-Terminal Deletions on Coxsackievirus B3 RNA Replication and Ribonucleoprotein Complex Formation. *J. Virol.* 91
27. Bouin, A., Nguyen, Y., Wehbe, M., Renois, F., Fornes, P., Bani-Sadr, F., Metz, D., and Andreoletti, L. (2016) Major Persistent 5' Terminally Deleted Coxsackievirus B3 Populations in Human Endomyocardial Tissues. *Emerging Infect. Dis.* 22, 1488-1490

28. Huang da, W., Sherman, B. T., and Lempicki, R. A. (2009) Bioinformatics enrichment tools: paths toward the comprehensive functional analysis of large gene lists. *Nucleic Acids Res* 37, 1-13
29. Huang da, W., Sherman, B. T., and Lempicki, R. A. (2009) Systematic and integrative analysis of large gene lists using DAVID bioinformatics resources. *Nat Protoc* 4, 44-57

Chapter 6:

Discussion and Future Directions

6.1. Summary of Dissertation

Decoding complex host-pathogen interactions requires the use of systems-biology methods. In this dissertation we developed tools to study phosphatase coordination of cardiomyocyte signaling in the context of CVB3 infection.

In chapter 2 we developed a set of subcellular phosphatase activity assays which can measure activity specific to each major class of protein phosphatases. Thus, for the first time, we achieve simultaneous measurement of MAPK and STAT negative regulation in two subcellular compartments. We find that subcellular phosphatase activities are independently regulated and divergent subcellular responses can unveil processes important in acute viral infection and antiviral signaling.

In chapter 3 we developed a cell-based model of chronic CVB3 infection to investigate consequences of intracellular host-pathogen interactions. We find that cellular adaption to prolonged CVB3 expression is not restricted to a single response, but rather, can take many forms. In vivo, this has been linked to immunological haplotype diversity and gender (1, 2), but cellular molecular heterogeneity has not been systematically quantified. Our cell line model sets the stage for identifying cellular adaptation-specific outcomes of chronic CVB3 expression, something not easily achievable in vivo.

In chapters 3 and 4 we explore statistical methods of extracting phenomenological predictions from system-level data. These are important tools in interpretation of large data sets like those generated in this dissertation. Using these methods, we find that clonal adaptations to chronic CVB3 expression do not merely alter the activity of protein phosphatases but may actually rewire phosphatase regulatory mechanisms entirely.

Finally, in chapter 5 we explore other cell-based models of CVB3 infection. Based on transcriptomic data, we find that iPSC-derived cardiomyocytes faithfully emulate ERK-mediated growth responses to acute CVB3 infection (3-5). These cells present an exciting avenue for investigation of chronic infection though there is no evidence that they can initiate or sustain chronic CVB3 expression.

The concepts addressed and tools developed here can extend beyond the scope of this dissertation to further elucidate the role of protein phosphatases in human biology and intracellular pathways important in pathological cardiac inflammation.

6.2. Future Directions

Applications of substrate and context specific PPase assays

Protein phosphatases have been recognized as key drivers of several human diseases (6-10, 26-31). For example, PP2A and DUSP4 inhibition drives cell growth in cancer (26-29). Conversely, overexpression of PTP1B is correlated with poor prognosis in cancer (8-9, 30-31). Thus, there is great interest in developing targeted therapies to inhibit as well as activate phosphatase activity clinically. Our substrate-specific and context-specific phosphatase activity assays are poised to aid in early target identification and prioritization of small molecule lead compounds aimed at restoring healthy signal transduction.

Examples of current phosphatase activity screening include high-throughput assays utilizing artificial substrates (11) and cell-based fluorescence assays (12). In the former, the use of generic substrates would not capture phosphatase inhibition from blocking of substrate binding motifs that lay distal to catalytic domains on some phosphatases. By contrast, our assay platform may capture molecules with that mechanism of action because each assay utilizes full length recombinant proteins. Cell-based fluorescence assays require complex machinery and high-content image processing that can be cumbersome for large inhibitor screens. However, high-throughput screening with our assay can be done in an “ex vivo” manner where inhibitors or agonists can be spiked-in to banked cellular extracts to assess modulation of multiple pathways at once. While our assay does not assess specificity for individual phosphatases, our subcellular fractionation can help identify compounds that work in the compartment of interest. Furthermore, current assays cannot identify off-target effects on other signaling cascades. For example, many ERK targeting phosphatases also have specificity for p38 and

JNK proteins (13). Thus, multiplexed investigation of all three pathways in our assay platform would help prioritize ERK pathway specific drugs earlier in the development pipeline. Additionally, phosphatase extracts can also be prepared from preclinical cell-based models of disease to test bioactivity of lead compounds in vitro. These considerations as well as the capability to fully automate our assay platform, from endogenous phosphatase extraction to activity quantification, make it an exciting opportunity for small molecule lead prioritization.

Computational models of signal transduction pathways are being increasingly used to identify therapeutic targets and predict clinical outcomes (14). While the importance of phosphatase negative regulation has been acknowledged (15, 16), most phosphatase reactions are governed by free parameters (17-19). Experimental footing for stimulus-driven dynamics in such models may constrain these sensitive nodes and reveal feedback mechanisms important to drug efficacy or resistance. This can be achieved within the framework of current ordinary differential equation (ODE) based model development where network architecture is determined from literature and free parameters are fitted to experimental data. Unbiased measurement of phosphatase activity in our assays allows for the derivation of a single rate parameter which phenomenologically recapitulates not only multiple phosphatases per substrate but also many regulatory processes including transcription/translation, subcellular shuttling, and post-translational modifications. Thus, addition of dynamic phosphatase activity to ODE models would nominally increase the complexity of the network architecture but stands to significantly improve modeling of negative feedback loops, facilitating the discovery of emergent phenomena.

Extending in vitro chronic CVB3 model to assess consequences of host-pathogen interactions

Viral RNA presence and subsequent viral protein expression during infection have multifarious effects on the host-cell at the protein and transcript levels. The magnitude of these effects maybe an important determinant of overall cellular behavior. In fact, in Chapter 3 we found that expression levels

of viral RNA correlated with certain gene programs in cellular models of chronic CVB3 infection (Chapter 3, Figure 1); suggesting that viral RNA (and consequently viral protein) dosage may be a key determinant of cellular adaptation to chronic infection. We can assess how responsive these programs are to the dosage of CVB3 RNA through the use of shRNAs targeting the viral transcript. For example, we have shown that knockdown of CVB3 with two high-efficiency hairpins results in loss of differential IL6 expression between “high” CVB3 expressing clones B3 and B4 (Chapter3 Figure S2A) and “low” CVB3 expressing clone C3 (Figure 1 A&B). By contrast, IL7R expression was mildly decreased in all clones with shCVB3 knockdown but differential expression was maintained (Figure 1C). This may highlight stable clonal adaptations that are relatively insensitive to the current CVB3 status of the cell. Using this method, we can also titrate the shCVB3 hairpin to find dose-dependent adaptations in a clone with a high CVB3 copy number. Such studies would prioritize altered gene families and elucidate mechanisms underlying dose-dependent prognoses documented in the clinic where patients with higher chronic CVB3 expression experience increased disease severity (32).

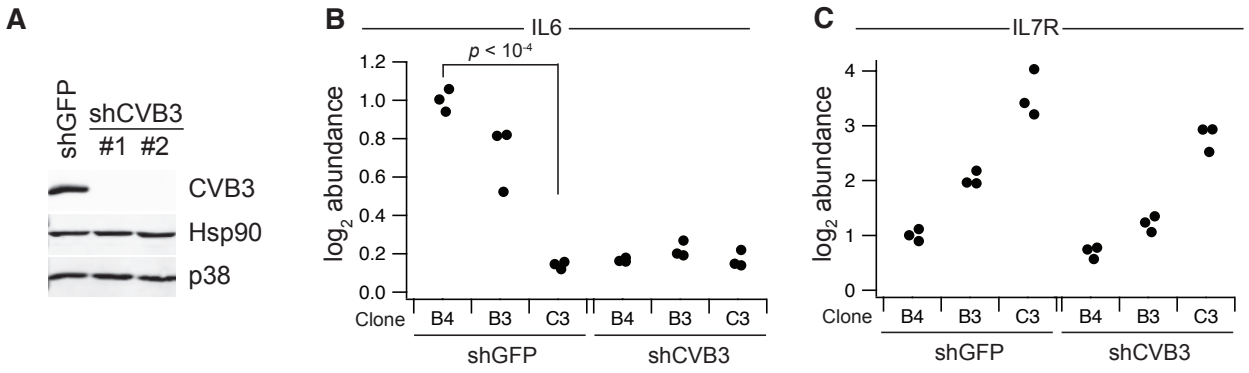

Figure 1. CVB3 knockdown can elucidate CVB3-expression driven transcriptional adaptations
A. Hairpin validation of two shCVB3 constructs in acutely infected HeLa cells. Both hairpins achieved >90% knockdown assessed by VP1 immunoblot. B. Group B clones express more IL6 transcript than Group C clone. With shCVB3 knockdown, IL6 relative abundance in Group B clones drop to Group C clone levels. Assessed by qPCR of n = 3 biological replicates. C. IL7R differential expression is maintained with shCVB3 knockdown. Assessed by qPCR of n = 3 biological replicates. All sample are relative to B4 shGFP.

While AC16 cells provide an ideal model system to study the diversity of chronic CVB3 adaptations, we are not able to assess resultant structural and contractile changes as AC16s do not assemble functional sarcomeres (33). Cardiomyocytes derived from iPSC cells may provide a complementary model system from which we can measure population-level changes in morphology (e.g. hypertrophy) as well as beat frequency and sarcomere structure in parallel with intracellular measurements (e.g. phosphatase activity). Chronic CVB3 expression in iPSC cardiomyocytes cannot be achieved through genetic engineering as with AC16s because iPSC cardiomyocytes do not proliferate. Instead, chronic CVB3 expression can be achieved by delivering virions carrying 5'-truncated CVB3 genomes as discussed in Chapter 5.3. Importantly, both cell-based models reflect cardiac biology observed in patients. Using unsupervised principle components analysis on the transcriptome of AC16s, iPSC-cardiomyocytes, and patient tissue from the GTEx database (34), we find that the first principle component delineates heart-derived samples from skin-derived samples (Figure 2). This segregation suggests that AC16s, while fused with skin fibroblasts, retain much of their cardiac-like biology. Further, along PC1, iPSCs align with the tail of patient left ventricle samples suggesting that they may not represent mature adult cardiomyocytes though they exhibit contractile function (35-36). Similarly, AC16 cells align with both ventricular and atrial GTEx samples suggesting a mixed cardiac phenotype as documented previously (33). We can further mine the GTEx data for patients harboring latent viral heart infections and compare the transcriptome of these samples to infected AC16 and iPSC cardiomyocytes. The second principle component captures a minority of the remaining variance in the data (~15%) and segregates GTEx samples from data generated in this study. This may suggest that remaining variance stems from differences in in vitro and ex vivo samples, RNA-seq techniques, alignment and normalization algorithms, and/or cell culture and tissue collection approaches. While an ideal chronic CVB3 infection model would allow assessment of contractile, morphological, intracellular, and diverse genetic adaptions, this is not easily achievable in vitro. Thus, we can use complementary AC16 and iPSC derived models to address these aspects in relevant cardiac cellular models.

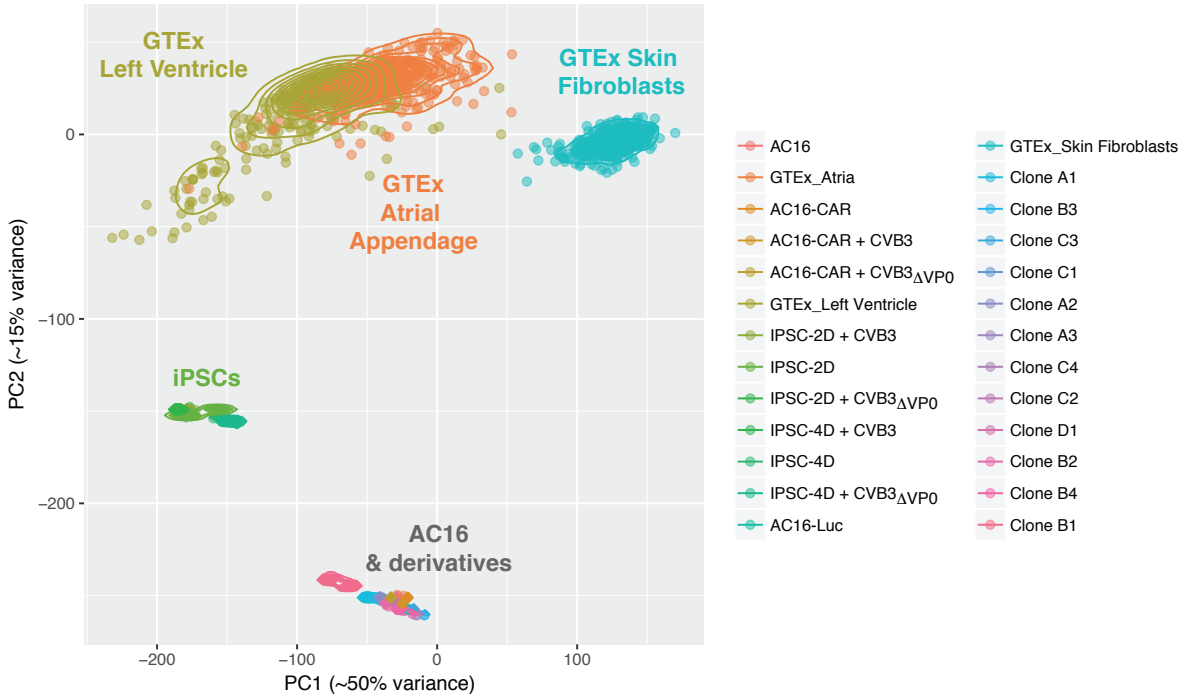

Figure 2. Cellular cardiomyocyte models reflect patient biology at the transcriptomic level
Transcripts per million (TPM) data was downloaded from GTEx database and patient data from left ventricle tissue, atrial appendage, and skin fibroblasts were extracted. GTEx TPM data was combined with iPSC and AC16 cardiomyocyte TPM data by shared ensemble gene identifiers. Approximately, 32,000 genes were used for principle components analysis. Inclusion was determined by at least one sample having a TPM $\geq$ 1 for a gene.

Coxsackievirus B3 as a model for identifying pathways important to cardiac inflammation

The experimental model of chronic CVB3 infection described in this dissertation facilitates investigation of the host response to viral infection at the systems-level. As a proof of principle, we demonstrated that adaptation-specific rewiring of intracellular signaling pathways can result in altered cytokine production in Chapter 3. By extending these types of analyses to include a wider range of stimuli as well as combinatorial conditions, we can build a predictive PLSR model linking pathway regulation to cytokine secretion. Additionally, we can leverage viral expression and adaptation-specific signaling to assess how perturbations in intracellular signaling can modulate the cardiac inflammatory milieu. Then, through in vitro coculture we can examine how disrupting these pathways in a targeted manner would impact immune cell activation and cytokine mediated crosstalk. Ultimately, understanding the connectivity of inflammation-induced paracrine signaling can expose redundant or

synergistic factors. Ablation of these cytokines could break the feedback circuit between cardiomyocytes and immune cells to resolve pathological inflammation. This may be generalizable to chronic heart failure (CHF) where myocardial production of inflammatory cytokines IL1β, TNFα, and IL6 lead to end-stage disease (20-22). While the pathogenic role of these molecules is certain, clinical trials of anti-TNFα therapies have had little success and some have even been detrimental (23-25). These failures may suggest redundancy in proinflammatory factors in CHF. Thus, systems-level study of cardiac immunomodulation may identify new more effective combinatorial anti-cytokine therapies for end-stage disease.

6.3. Concluding remarks

This dissertation highlights the impact systems-biological methods can have on our understanding of coordinated cellular processes ranging from biochemical and transcriptomic to paracrine signaling. Indeed, we have shown that decoding complex, bidirectional host-pathogen interactions require systems-level interrogation. Furthermore, the tools developed here can be applied to several areas of biomedical research and could aid not only in fundamental discoveries about biological networks but also in translational applications.

6.4. References

1. Lodge, P. A., Herzum, M., Olszewski, J., and Huber, S. A. (1987) Coxsackievirus B-3 myocarditis. Acute and chronic forms of the disease caused by different immunopathogenic mechanisms. *Am J Pathol* 128, 455-463
2. Lyden, D., Olszewski, J., and Huber, S. (1987) Variation in susceptibility of Balb/c mice to coxsackievirus group B type 3-induced myocarditis with age. *Cell. Immunol.* 105, 332-339
3. Sanna, B., Bueno, O. F., Dai, Y.-S., Wilkins, B. J., and Molkentin, J. D. (2005) Direct and indirect interactions between calcineurin-NFAT and MEK1-extracellular signal-regulated kinase 1/2 signaling pathways regulate cardiac gene expression and cellular growth. *Mol. Cell. Biol.* 25, 865-878
4. Huber, M., Watson, K. A., Selinka, H. C., Carthy, C. M., Klingel, K., McManus, B. M., and Kandolf, R. (1999) Cleavage of RasGAP and phosphorylation of mitogen-activated protein kinase in the course of coxsackievirus B3 replication. *J. Virol.* 73, 3587-3594
5. Murphy, L. O., Smith, S., Chen, R.-H., Fingar, D. C., and Blenis, J. (2002) Molecular interpretation of ERK signal duration by immediate early gene products. *Nat. Cell Biol.* 4, 556-564
6. De Rocca Serra-Nédélec, A., Edouard, T., Tréguer, K., Tajan, M., Araki, T., Dance, M., Mus, M., Montagner, A., Tauber, M., Salles, J.-P., Valet, P., Neel, B. G., Raynal, P., and Yart, A. (2012) Noonan syndrome-causing SHP2 mutants inhibit insulin-like growth factor 1 release via growth hormone-induced ERK hyperactivation, which contributes to short stature. *Proc Natl Acad Sci U S A* 109, 4257-4262
7. Xu, R., Yu, Y., Zheng, S., Zhao, X., Dong, Q., He, Z., Liang, Y., Lu, Q., Fang, Y., Gan, X., Xu, X., Zhang, S., Dong, Q., Zhang, X., and Feng, G.-S. (2005) Overexpression of Shp2 tyrosine phosphatase is implicated in leukemogenesis in adult human leukemia. *Blood* 106, 3142-3149
8. Wiener, J. R., Hurteau, J. A., Kerns, B. J., Whitaker, R. S., Conaway, M. R., Berchuck, A., and Bast, R. C. (1994) Overexpression of the tyrosine phosphatase PTP1B is associated with human ovarian carcinomas. *Am. J. Obstet. Gynecol.* 170, 1177-1183
9. Wang, N., She, J., Liu, W., Shi, J., Yang, Q., Shi, B., and Hou, P. (2015) Frequent amplification of PTP1B is associated with poor survival of gastric cancer patients. *Cell Cycle* 14, 732-743
10. Bollu, L. R., Mazumdar, A., Savage, M. I., and Brown, P. H. (2017) Molecular Pathways: Targeting Protein Tyrosine Phosphatases in Cancer. *Clin. Cancer Res.* 23, 2136-2142
11. Montalibet, J., Skorey, K. I., and Kennedy, B. P. (2005) Protein tyrosine phosphatase: enzymatic assays. *Methods* 35, 2-8
12. Vogt, A., Cooley, K. A., Brisson, M., Tarpley, M. G., Wipf, P., and Lazo, J. S. (2005) Cell-active dual specificity phosphatase inhibitors identified by high-content screening. *Drug Discov. Today* Suppl, 3-12
13. Kondoh, K., and Nishida, E. (2007) Regulation of MAP kinases by MAP kinase phosphatases. *Biochim. Biophys. Acta* 1773, 1227-1237
14. Kirouac, D. C., Schaefer, G., Chan, J., Merchant, M., Orr, C., Huang, S. A., Moffat, J., Liu, L., Gadkar, K., and Ramanujan, S. (2017) Clinical responses to ERK inhibition in BRAF(V600E)-mutant colorectal cancer predicted using a computational model. *NPJ Syst Biol Appl* 3, 14

15. Bhalla, U. S., Ram, P. T., and Iyengar, R. (2002) MAP kinase phosphatase as a locus of flexibility in a mitogen-activated protein kinase signaling network. *Science* 297, 1018-1023
16. Heinrich, R., Neel, B. G., and Rapoport, T. A. (2002) Mathematical models of protein kinase signal transduction. *Mol. Cell* 9, 957-970
17. Chen, W. W., Schoeberl, B., Jasper, P. J., Niepel, M., Nielsen, U. B., Lauffenburger, D. A., and Sorger, P. K. (2009) Input-output behavior of ErbB signaling pathways as revealed by a mass action model trained against dynamic data. *Mol. Syst. Biol.* 5, 239
18. Sasagawa, S., Ozaki, Y.-i., Fujita, K., and Kuroda, S. (2005) Prediction and validation of the distinct dynamics of transient and sustained ERK activation. *Nat. Cell Biol.* 7, 365-373
19. Schoeberl, B., Eichler-Jonsson, C., Gilles, E. D., and Müller, G. (2002) Computational modeling of the dynamics of the MAP kinase cascade activated by surface and internalized EGF receptors. *Nat. Biotechnol.* 20, 370-375
20. Briasoulis, A., Androulakis, E., Christophides, T., and Tousoulis, D. (2016) The role of inflammation and cell death in the pathogenesis, progression and treatment of heart failure. *Heart Fail Rev* 21, 169-176
21. Sánchez-Trujillo, L., Vázquez-Garza, E., Castillo, E. C., García-Rivas, G., and Torre-Amione, G. (2017) Role of Adaptive Immunity in the Development and Progression of Heart Failure: New Evidence. *Arch. Med. Res.* 48, 1-11
22. Kubota, T., Miyagishima, M., Alvarez, R. J., Kormos, R., Rosenblum, W. D., Demetris, A. J., Semigran, M. J., Dec, G. W., Holubkov, R., McTiernan, C. F., Mann, D. L., Feldman, A. M., and McNamara, D. M. (2000) Expression of proinflammatory cytokines in the failing human heart: comparison of recent-onset and end-stage congestive heart failure. *J. Heart Lung Transplant.* 19, 819-824
23. Mann, D. L., McMurray, J. J. V., Packer, M., Swedberg, K., Borer, J. S., Colucci, W. S., Djian, J., Drexler, H., Feldman, A., Kober, L., Krum, H., Liu, P., Nieminen, M., Tavazzi, L., van Veldhuisen, D. J., Waldenstrom, A., Warren, M., Westheim, A., Zannad, F., and Fleming, T. (2004) Targeted anticytokine therapy in patients with chronic heart failure: results of the Randomized Etanercept Worldwide Evaluation (RENEWAL). *Circulation* 109, 1594-1602
24. Mann, D. L. (2015) Innate immunity and the failing heart: the cytokine hypothesis revisited. *Circ. Res.* 116, 1254-1268
25. Javed, Q., and Murtaza, I. (2013) Therapeutic potential of tumour necrosis factor-alpha antagonists in patients with chronic heart failure. *Heart Lung Circ* 22, 323-327
26. Mazumdar, A., Poage, G. M., Shepherd, J., Tsimelzon, A., Hartman, Z. C., Den Hollander, P., Hill, J., Zhang, Y., Chang, J., Hilsenbeck, S. G., Fuqua, S., Kent Osborne, C., Mills, G. B., and Brown, P. H. (2016) Analysis of phosphatases in ER-negative breast cancers identifies DUSP4 as a critical regulator of growth and invasion. *Breast Cancer Res Treat* 158, 441-454
27. Neviani, P., Santhanam, R., Trotta, R., Notari, M., Blaser, B. W., Liu, S., Mao, H., Chang, J. S., Galietta, A., Uttam, A., Roy, D. C., Valtieri, M., Bruner-Klisovic, R., Caligiuri, M. A., Bloomfield, C. D., Marcucci, G., and Perrotti, D. (2005) The tumor suppressor PP2A is functionally inactivated in blast crisis CML through the inhibitory activity of the BCR/ABL-regulated SET protein. *Cancer Cell* 8, 355-368
28. Janghorban, M., Farrell, A. S., Allen-Petersen, B. L., Pelz, C., Daniel, C. J., Oddo, J., Langer, E. M., Christensen, D. J., and Sears, R. C. (2014) Targeting c-MYC by antagonizing PP2A inhibitors in breast cancer. *Proc Natl Acad Sci U S A* 111, 9157-9162

29. Sontag, E., Fedorov, S., Kamibayashi, C., Robbins, D., Cobb, M., and Mumby, M. (1993) The interaction of SV40 small tumor antigen with protein phosphatase 2A stimulates the map kinase pathway and induces cell proliferation. *Cell* 75, 887-897
30. Hoekstra, E., Das, A. M., Swets, M., Cao, W., van der Woude, C. J., Bruno, M. J., Peppelenbosch, M. P., Kuppen, P. J., Ten Hagen, T. L., and Fuhler, G. M. (2016) Increased PTP1B expression and phosphatase activity in colorectal cancer results in a more invasive phenotype and worse patient outcome. *Oncotarget* 7, 21922-21938
31. Liu, H., Wu, Y., Zhu, S., Liang, W., Wang, Z., Wang, Y., Lv, T., Yao, Y., Yuan, D., and Song, Y. (2015) PTP1B promotes cell proliferation and metastasis through activating src and ERK1/2 in non-small cell lung cancer. *Cancer Lett* 359, 218-225
32. Satoh, M., Akatsu, T., Ishikawa, Y., Minami, Y., Takahashi, Y., and Nakamura, M. (2007) Association between toll-like receptor 8 expression and adverse clinical outcomes in patients with enterovirus-associated dilated cardiomyopathy. *Am Heart J* 154, 581-588
33. Davidson, M. M., Nesti, C., Palenzuela, L., Walker, W. F., Hernandez, E., Protas, L., Hirano, M., and Isaac, N. D. (2005) Novel cell lines derived from adult human ventricular cardiomyocytes. *J Mol Cell Cardiol* 39, 133-147
34. Consortium, G. T. (2013) The Genotype-Tissue Expression (GTEx) project. *Nat Genet* 45, 580-585
35. Zhang, J., Wilson, G. F., Soerens, A. G., Koonce, C. H., Yu, J., Palecek, S. P., Thomson, J. A., and Kamp, T. J. (2009) Functional cardiomyocytes derived from human induced pluripotent stem cells. *Circ Res* 104, e30-41
36. Ma, J., Guo, L., Fiene, S. J., Anson, B. D., Thomson, J. A., Kamp, T. J., Kolaja, K. L., Swanson, B. J., and January, C. T. (2011) High purity human-induced pluripotent stem cell-derived cardiomyocytes: electrophysiological properties of action potentials and ionic currents. *Am J Physiol Heart Circ Physiol* 301, H2006-2017